BRNO UNIVERSITY OF TECHNOLOGY

VYSOKÉ UČENÍ TECHNICKÉ V BRNĚ

FACULTY OF MECHANICAL ENGINEERING

FAKULTA STROJNÍHO INŽENÝRSTVÍ

INSTITUTE OF AEROSPACE ENGINEERING

LETECKÝ ÚSTAV

FATIGUE CRACK GROWTH RETARDATION TECHNIQUES FOR THE INTEGRAL AIRFRAME STRUCTURE

FATIGUE CRACK GROWTH RETARDATION TECHNIQUES FOR THE INTEGRAL AIRFRAME STRUCTURE

DOCTORAL THESIS

DIZERTAČNÍ PRÁCE

AUTHOR — **Ing. Václav Jetela**

AUTOR PRÁCE

SUPERVISOR — **doc. Ing. Josef Klement, CSc.**

ŠKOLITEL

BRNO 2022

Abstract

A problem with fast crack propagation arose from utilizing integral airframe structure. One of the techniques to slow down crack propagation and prolong the fatigue life is the application of crack retarder. The aim of this thesis is to compare the performance of additively manufactured crack retarders with bonded ones in terms of the fatigue life, crack growth rate and delamination. In case of the bonded crack retarders; no attention has been paid to the crack retarders made of stainless steel. The stainless steel appears to be a suitable candidate for its coefficient of thermal expansion close to the aluminum, high strength and elastic modulus. Regarding the additively manufactured crack retarders, little or no attention has been paid to the crack retarders made of metals different than the base structure.

To address this research gap, two distinctive technologies were selected: cold spray and ultrasonic consolidation. Using the cold spray, the titanium and stainless steel crack retarders were deposited. Using the ultrasonic consolidation, the stainless steel crack retarders were welded. In the experimental work, the crack advance was visually observed. The crack retarder delamination was monitored using the pulsed thermography with subsequent Thermographic Signal Reconstruction. Bonded stainless steel crack retarders proved to be an suitable alternative to the already proven carbon fibre crack retarders. Stainless steel retarders significantly lowered the fatigue crack growth rate which resulted in longer fatigue life. However, all cold sprayed crack retarders accelerated crack growth rate and led to the specimen's premature failure. Ultrasonically consolidated crack retarder with two steel layers was the most effective in the life prolongation. The study also proved, that the delamination in the ultrasonically consolidated metal laminates can be detected using pulsed thermography.

Keywords: Selective reinforcement, Bonded Crack Retarder, Cold Spray, Ultrasonic Consolidation, Crack growth, Damage Tolerance, Thermography, Delamination.

Abstrakt

Únavová trhlina roste v integrální konstrukci rychleji než v konstrukci nýtované. Tento problém se projevuje výrazně nižší životností integrální konstrukce. Jednou z metod jak omezit růst dlouhých únavových trhlin je aplikace lokálního vyztužení, tzv. zastavovače trhliny. Zastavovač omezuje rozevření čela trhliny, čímž výrazně zpomaluje její růst.

V první části práce jsou kriticky hodnoceny dosavadní studie zabývající se metodami zpomalování růstu dlouhých únavových trhlin. Rešerše je rozšířena i na technologie, které materiál nepřidávají, ale například pouze mění stav materiálu podkladové konstrukce. Studie jsou hodnoceny s ohledem na použité technologie, materiály a zvýšení únavové životnosti. Rovněž jsou zmíněny obecné závěry týkající se požadavků na vlastnosti optimálního zastavovače trhlin. Na konci rešerše jsou diskutovány směry, kterými by se mohl ubírat výzkum v oblasti zpomalování růstu dlouhých únavových trhlin.

Na základě zjištěných mezer v současném stavu poznání byl stanoven cíl práce; porovnat dopad lepených a aditivně vyrobených zastavovačů na růst trhliny v konstrukci z hliníkové slitiny. Přičemž byly vybrány tyto aditivní technologie: cold spray a ultrazvuková konsolidace. Obě tyto technologie umožňují vytvořit vysokopevnostní spoj mezi nestejnými kovovými materiály, čímž by bylo možné minimalizovat rozvoj delaminace mezi zastavovačem a podkladovou konstrukcí. Z hlediska materiálů se práce zaměřuje zejména na vysokopevnostní nerezovou ocel z těchto důvodů: vysoká pevnost, vysoký modul pružnosti v tahu a koeficient tepelné roztažnosti blízký hliníkové slitině. Pro potřeby porovnání byly do studie zahrnuty i lepené zastavovače z uhlíkového kompozitu a stříkané zastavovače z titanové slitiny.

Teoretická část práce poskytuje vhled do lineární lomové mechaniky a šíření dlouhých únavových trhlin. Rovněž jsou diskutovány efekty mající dopad na růst únavových trhlin v kovových konstrukcích. V kapitole jsou také představeny jednotlivé technologie použité pro výrobu zastavovačů trhlin v této práci. V závěru kapitoly jsou podrobně rozebrány mechanismy a vlastnosti zastavovačů trhliny, které mají pozitivní i negativní dopad na rychlost šíření trhliny v podkladové konstrukci.

V experimentální části práce je nejprve popsána výroba vzorků se zastavovači trhlin. V případě lepených zastavovačů byly použité v minulosti osvědčené postupy úpravy adherendů. V případě zastavovačů stříkaných metodou cold spray byly použity v minulosti optimalizované procesní parametry nástřiku. Pro výrobu ultrazvukově konsolidovaných zastavovačů bylo nezbytné provést optimalizaci procesních parametrů, protože jejich hodnoty nebyly pro danou aplikaci ověřené. Připravené vzorky byly podrobeny cyklickému zatížení při němž se opticky pozoroval vznik a následný růst únavové trhliny. Za účelem zachycení delaminace byla vyztužená strana vzorku snímána termokamerou. Termokamera snímala teplotní odezvu vzorku po optické excitaci. Termogramy byly dále zpracovávány metodou rekonstrukce termografického signálu za účelem zvýšení kontrastu delaminace.

Měřením bylo prokázalo, že zastavovače z nerezové oceli významně prodloužují životnost hliníkové konstrukce a snižují rychlost šíření trhliny. To platí pro zastavovače lepené a ultrazvukově konsolidované. Zastavovače z titanové slitiny a nerezové oceli vyráběné metodou cold spray nebyly efektivní. Jejich aplikace na podkladovou konstrukci vedla ke snížení únavové živostnosti a zvýšení rychlosti šíření únavové trhliny v podkladové konstrukci. Stříkané zastavovače nedelaminovaly; únavová trhlina prorostla přímo do zastavovačů trhlin. K přímému růstu trhliny do zastavovače došlo i v případě vzorku s ultrazvukově konsolidovanými zastavovači. Zastavovače ze dvou vrstev oceli umožnily zpomalit růst únavové trhliny nejvíce. Zastavovač v tomto případě delaminoval. Přičemž závislost velikosti delaminace na počtu cyklů má stejný trend jako v případě zastavovačů lepených.

Tato disertační práce porovnává dopad doposud nevyzkoušených materiálů zastavovače a výrobních technologií na rychlost šíření trhliny v hliníkové konstrukci, delaminaci zastavovače a životnost vzorku. Výsledky studie je možné využít k tvorbě modelů predikujících růst trhliny v ultrazvukově konsolidovaných a lepených konstrukcích. Výsledky experimentálních měření navíc prokazují, že je možné detekovat delaminaci v ultrazvukově konsolidovaném laminátu metodou pulzní termografie.

Klíčová slova: Lokální vyztužení, Lepený zastavovač trhliny, Cold spray, Ultrazvuková konsolidace, Růst trhliny, Přípustné poškození, Termografie, Delaminace.

Citation

JETELA, Václav. *Fatigue Crack Growth Retardation Techniques for the Integral Airframe Structure*. Brno, 2022. Doctoral thesis. Brno University of Technology, Faculty of Mechanical Engineering, Institute of Aerospace Engineering. Supervisor Josef Klement.

Declaration

I declare that this thesis is the result of my own work under the guidance of my supervisor and all literature and electronic sources used for the research are cited in the list of literature.

In Brno, 29th Jun, 2022 .....

Václav Jetela

Acknowledgment

I am extremely grateful to my supervisor, Assoc. Prof. Josef Klement, for his expert guidance, encouragement and patience. This work would not have been possible without the generous support from the Internal Grant Agency of Brno University of Technology [project no. FSI-S-20-6288]; who financed my research. I would also like to acknowledge the assistance of Dr. Petr Augustin for assisting in the fatigue crack growth testing. Many thanks to Jan Kondas and Dr. Jan Čížek for helping me to obtain specimens with cold sprayed coatings. Thanks should also go to Dr. Petr Kracík for giving me the introductory thermal imaging training and enabling me to use the departmental thermal camera. Special thanks to Dr. Michal Mališ, for valuable discussions about data processing, researchers' struggle and life. Thanks also to Hana Říhová for expending so much effort when processing the international orders. I am also grateful to the the most skillful IAE's technician, Pavel Krpálek, for machining support prior testing. Special thanks to my friend, Jakub Holzer, for SEM and OM images. Thanks should also go to Penta Trading's technician, Tomáš Sperlich, for his proactive approach when machining EDM notches.

I am seriously indebted to my father, he has taught me a lot about persistence and getting things done. I would also like to extend my deepest gratitude to my mother and her family, for being my greatest mental support. This thesis would not have been written without constant encouragement of my girlfriend, Lenka. She has always been by my side through the hardest times. Particularly helpful to me during this time were also Dr. Marek Vácha, Mark Manson and Pavel Moric. They have taught me how to process failures, push boundaries and be grateful.

Contents

1 Introduction **11**

1.1 Problem formulation 11

1.2 Justification of the problem 13

2 Literature review **15**

2.1 Bonded crack retarders 15

2.2 Geometry modification 23

2.3 Cold spray 24

2.4 Residual stresses 25

2.5 Consolidation 26

2.6 Summary 27

2.7 Prospects 27

3 Aim and Objectives **31**

4 Theory **33**

4.1 Linear Elastic Fracture Mechanics 33

4.2 Fatigue crack growth 38

4.3 Effects on macrocrack growth and life 43

4.4 Manufacturing technologies 46

4.5 Mechanisms related to crack retarders 58

5 Experimental Work **67**

5.1 Substrate 67

5.2 Bonded crack retarders 69

5.3 Cold sprayed crack retarders 72
5.4 Consolidated crack retarders 73
5.5 Fatigue crack growth test 76
5.6 Delamination monitoring 77
5.7 Digital image processing 78
5.8 Results and discussion 80

6 Conclusion **91**
6.1 Research implication and contribution 92
6.2 Future research ideas 94

References **95**

Abbreviations **107**

A Delamination data **i**
A.1 1-CFUD-BCR i
A.2 2-CFUD-BCR ii
A.3 1-AISI301A-BCR iii
A.4 2-AISI301B-BCR v
A.5 2-AISI301-UCCR vii

Chapter 1

Introduction

1.1 Problem formulation

The primary airframe structure may consists of stringers, skin and trusses. Riveting, a traditional technique to join these structural elements together, is being replaced by the integral airframe structures manufacturing (Fig. 1.1). Besides the welded integral structures, where stringers are made separately and then welded to the separately manufactured skin, the integral panels can be extruded or high-speed machined. There, stringers and skin are made from one piece.

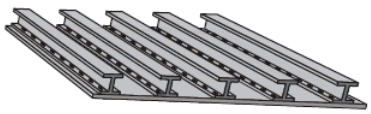

Riveted

Boeing	Douglas	Airbus Industrie	Lockheed	Antonov	Il'ushin	Tupolev	Yakovlev
B-707	DC-8	A300	C-130	AN-10	IL-18	TU-104	YaK-40
B-727	DC-9	A310	L-1011	AN-12	IL-96	TU-134	YaK-42
B-737	DC-10	A320				TU-154	
B-747		A330				TU-204	
B-757		A340					
B-767							
B-777							

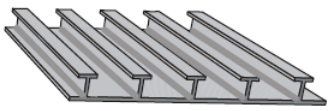

Integrally stiffened

Aerospatiale -British Aerospace "Concorde"	Lockheed	Dornier	Vickers	Antonov		Il'ushin	Tupolev
	C-188	Do 228	VC 10	AN-22	AN-70	IL-62	TU-144
	C-141			AN-24	AN-72	IL-76	
	C-5			AN-26	AN-74	IL-86	
				AN-30	AN-124		
				AN-32	AN-225		

Figure 1.1: Stiffened wing structures [1].

In comparison with the riveted structures, the integral airframe structures saves weight and contain less stress concentrators but do not contain the physical barriers against fatigue crack growth. The physical barrier is classified as a place in a structure where one part of a structure is covered by another part (Fig. 1.2). If the physical barriers are non-existent, the fatigue crack can grow from one part to another without a delay [1]. This results in the earlier fatigue failure of integral structure. Such problem can be expressed by the fatigue crack growth curve of both structures (Fig. 1.3).

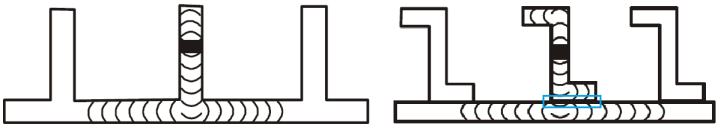

Figure 1.2: A comparison of integral and riveted structures: Physical barrier marked with blue colour [1].

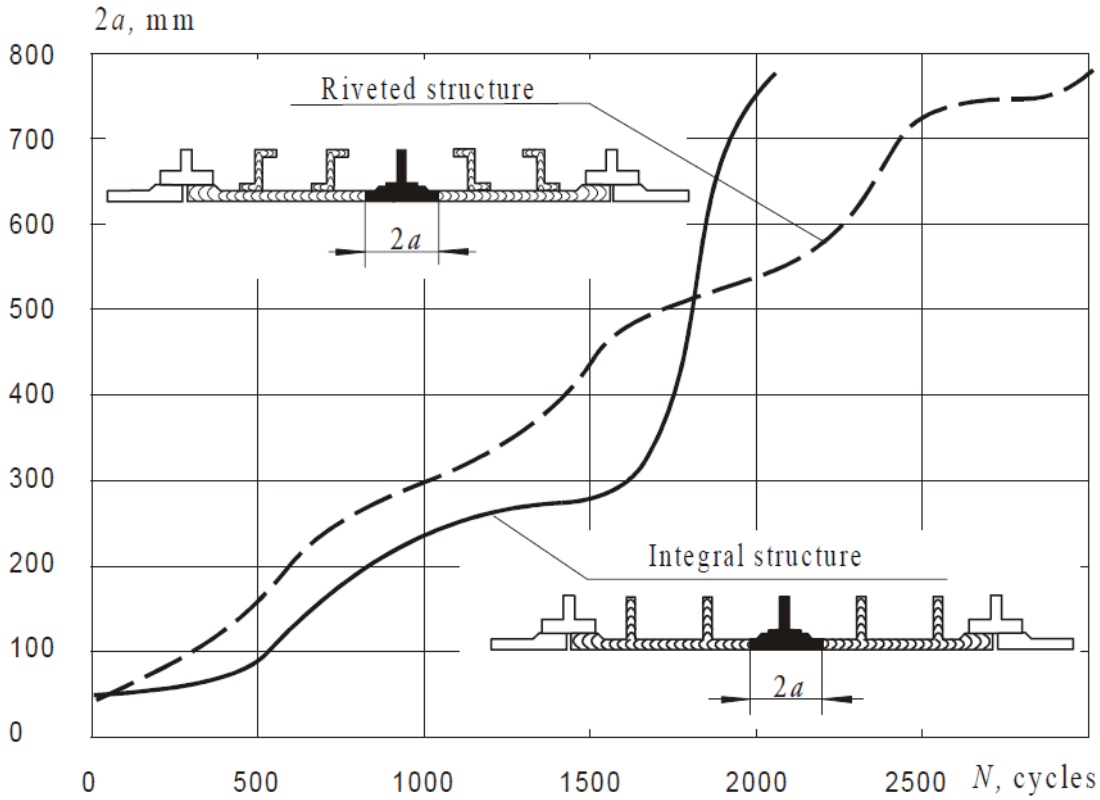

Figure 1.3: Duration of crack growth in riveted and integral panel skin from initial skin crack beneath broken central stringer [1].

1.2 Justification of the problem

According the previous section, the integral airframe structure can be seen as a fatigue critical component. With respect to the study from 2002 [2], fatigue had contributed 55% towards aircraft service failures (Tab. 1.1). Regulators are aware of it and thus penalize unitized structures by imposing an additional design safety factor [3]. By increasing the number of design safety factors, the aircraft structure becomes heavier. Considering these facts, it is even more important to cope with fatigue life extension of such structures to create greener aircraft.

Moreover, as the fatigue life extends, a decrease in the number of airframe inspections can be attained. It is desirable to reduce the number of inspections because: (1) the airframe maintenance occupies 30% of total aircraft maintenance cost and (2) the airframe maintenance cost per flight hour steadily increases as the aircraft ages [4].

Table 1.1: Frequency of failure machanisms in percentages [2].

Failure type	Engineering components	Aircraft components
Corrosion	29	16
Fatigue	25	55
Brittle fracture	16	-
Overload	11	14
Hight temperature corrosion	7	2
SCC/Corrosion fatigue/HE	6	7
Creep	3	-
Wear/abrasion/erosion	3	6

Chapter 2

Literature review

A research in fatigue crack growth retardation is evaluated in terms of used technologies, materials and obtained increases in fatigue life. The individual studies are arranged chronologically with a section for each technology. Moreover, general conclusions regarding crack retarder's performance, design and limitations are highlighted. At the end of this chapter, recommendations for further research directions are made with respect to obvious knowledge gaps.

2.1 Bonded crack retarders

In 1989, Schijve published a paper about the fatigue life evaluation of panels made of 2024-T3 alloy with the bonded, riveted and the integrally machined crack retarders. The crack retarders were made of Al alloy, Ti alloy and ARALL [5]. It was documented that the fatigue life of panel with BCRs was longer than the fatigue life of panel with riveted and integrally machined retarders. The stiffness of retarder and interference (retarder/panel) have the biggest impact on the effectiveness of retarder. It is well known that the bonded joint is much stiffer than the riveted joint. Probably this led to the longer fatigue life in case of the BCRs. Fatigue sensitivity is another important aspect. Fatigue crack nucleation was observed in all riveted retarders. As the crack initiated in the retarder, the enhancement in fatigue life was negligible. In case of the BCR, an adhesive acted as a barrier against the crack growth. According to the material selection, Ti alloy can offer excellent resistance

against fatigue. However, existing mismatch between the CTE of Ti and Al alloy leads to high thermal residual stresses, both in the retarder and the panel. At the end, the fatigue life of panel with Ti BCRs increased by a factor of 1.7 and with ARALL retarders increased by a factor of 1.4–2.0. In other words, the ARALL retarders performed as good as the Ti retarders.

Farley et al. presented results of a study aimed for the increase in fatigue life of CT specimens made of 7075 alloy with MMC retarders in 2004 [6]. Retarders were composed of the Al_2O_3 fibres and the Al-matrix. The individually manufactured retarders were adhesively bonded into the machined grooves on a both sides of the specimen. The increase in fatigue life by a factor of 5.0 was observed, however, the fatigue crack growth test did not continue till the final failure. Authors also did the parametric study to investigate the influence of retarder's width, thickness and adhesive stiffness on the crack growth and the fracture toughness.

In 2005, Zhang and Li focused on experiments with the riveted, welded and the integrally stiffened panels made of 2024-T351 alloy [7]. To investigate the increase in fatigue life, the integrally machined panels with the Ti and CF BCRs were numerically analysed. Fatigue crack growth tests were supported by FEA for the welded and the integrally stiffened panel. In the analyses, the effect of continuous debonding during the crack propagation was also included. It appeared that the machined and the welded stiffeners lowered the SIF much more than the riveted ones. Moreover, the temperature mismatch after welding process introduced the compressive residual stresses between stiffeners and the positive residual stresses in the proximity of stiffeners. Negative residual stresses are favourable, they lower SIF and thus contributes to the fatigue life extension. The fatigue life of welded panels was much longer (factor 1.6) in contrast with integral ones. However, an unstable crack propagation occurred after the failure of stiffeners. The longest theoretical extension in the fatigue life by factor of 3.5 was observed in case of panel with CF UD BCRs. See Fig. 2.1 for a prediction.

The Colavita et al. wrote a paper oriented to the fatigue crack growth retardation in the 2024-T3 alloy M(T) specimens with CF retarders in 2006 [8]. The effect of adhesive curing temperatures on the fatigue crack growth was investigated. The

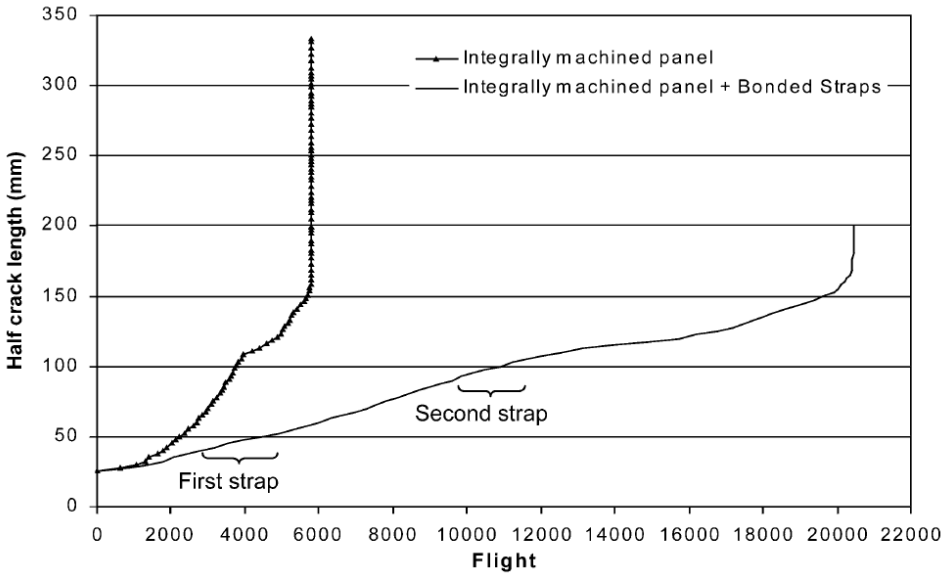

Figure 2.1: Predicted crack growth lives for integrally machined panels with and without crack retarder straps; aircraft service load spectrum (σ_{max} = 138 MPa) [7].

specimen cured at RT experienced lower residual stress levels, and thus longer fatigue life, than the specimen cured at 70 °C. The fatigue life of first specimen increased by factor of 3.0 while the latter one increased only by a factor of 1.09 . During the fatigue crack growth test, the continuous debonding started to grow, as the crack passed the first edge of retarder. Although the tests were supported by FEA, the analyses were conservative only up to the last edge of retarder.

In 2008, Zhang et al. continued at work of Colavita et al. They engaged in the testing of 2024-T351 M(T) specimens and 7085-T7651 SENT specimens with GF and Ti crack retarders [9]. Tests conducted during this and the previous study were supported by FEA incorporating a new model of continuous debonding. In case of the SENT specimens with CF crack retarders cured at 120 °C, the fatigue life extension was not significant (factor 1.07), as opposed to specimens with Ti crack retarders (factor 1.6) and GF crack retarders (factor 1.35). They concluded that both the CTE and the stiffness of CF crack retarder were dissimilar to substrate's values, resulting in high shear stresses in the adhesive joint. This led to the delamination within the BCR and/or in the adhesive joint. Delamination localization rely on the toughness of adhesive and matrix. The higher the toughness, the more likely the delamination occurs.

A Boscolo et al.'s study on a fatigue life increase through crack retarders made of GLARE, CF, GF and Ti alloy was focused on the completion of FE model [3] to support Colavita's experiments. The influence of retarder's material, size and location on the fatigue crack growth was examined. In addition, they developed a design tool to achieve the optimal crack retarder design in terms of prescribed fatigue life target and minimum structural weight added by the crack retarder. Their two-dimensional modelling technique, called LICRA, comprises progressive delamination based on Tahmasebi's adhesive model [10], the computation of thermal residual stresses and their redistribution during the crack propagation. This extensive work is discussed in detail in Boscolo's PhD thesis [11]. Based on experimental observation and FE modelling, Boscolo concluded:

- higher BCR elastic modulus and cross section increase the fatigue crack growth retardation,
- as the adhesive stiffness increases, the bridgining effect increases,
- as the adhesive toughness increases, the delamination propagation decreases,
- at lower SIF ranges, the TRS can negatively affect or cancel stiffening and bridging effect,
- at higher SIF ranges, the BCR elastic modulus and cross section are the major design parameters.

The Liljedahl et al. numericaly analysed the thermal residual stresses in the 7085-T651 SENT specimen with Ti crack retarders. The modelling results matched well with experimental observations [12].

In 2009, Liljedahl et al. wrote a paper about the change in residual stress distribution during fatigue crack propagation in 7085-T7651 SENT specimens with Ti and CF crack retarders[13]. The measured residual stresses were validated through FE analyses. Authors observed the continuous delamination as the crack passed the last edge of crack retarder. The greatest crack retardation between the stiffened and unstiffened side was observed in the specimens with CF crack retarders. This was caused mainly due to the high elastic modulus of CF crack retarder. Authors

concluded that the stiffness ratio, residual stresses and the presence of delamination have the greatest impact on the fatigue crack growth.

Moreira and Castro analyzed the fatigue life of 6056-T651, 6056-T4 and 6056-T6 integrally stiffened panels produced using the high speed cutting, friction stir and laser beam welding in 2010 [14]. Authors came to the same conclusion as Li and Zhang; welded panels possess longest fatigue life.

Irving et al. presented at the ICAF 2011 a paper on a crack retardation in 7085-T7651 M(T) and SENT specimens with GLARE, Ti, Al and CF crack retarders [15]. A series of tests were conducted at three stress levels with the CA and VA loading. The greatest increase in fatigue life was observed in the specimen with Al crack retarders (factor 3.8, SENT specimen, CA) and the GLARE crack retarders (factor 2.7, M(T) specimen, CA). However, an unwanted crack nucleation and growth were detected in the Al crack retarders. Fatigue crack growth tests were conducted once again on the integrally stiffened panels with GLARE and Al crack retarders, and supported by FE analyses comprising a delamination. The greatest advantage of GLARE lies in its CTE close to the substrate's value resulting in lower residual stresses in the substrate (Fig. 2.2), and thus longer fatigue life. Liljedahl in his study on an evolution of residual stresses in specimens with GLARE, Ti, CF crack retarders came to the same conclusion [16]. The measured residual stresses matched the residual stress levels from FE analyses.

In 2011, Liljedahl in his study on an evolution of residual stresses in specimens with Ti crack retarders tested at RT and -50 °C came to the conclusion that thermal residual stresses at such temperature are twice as large compared to the room temperature [17].

Brot and Kressel finished the experimental and numerical studies on the 2024-T351 panels stiffened with CF and BF crack retarders [18]. The tests were performed at RT and -50 °C. The fatigue life of panels tested at RT with CF crack retarder increased by a factor of 2.0 and with BF BCR by a factor of 1.6. The decrease in the ambient temperature to -50 °C led to much longer fatigue lives in case of the specimen with CF retarder (factor 6.5). Authors emphasized that no delamination between the substrate and the retarder had been observed.

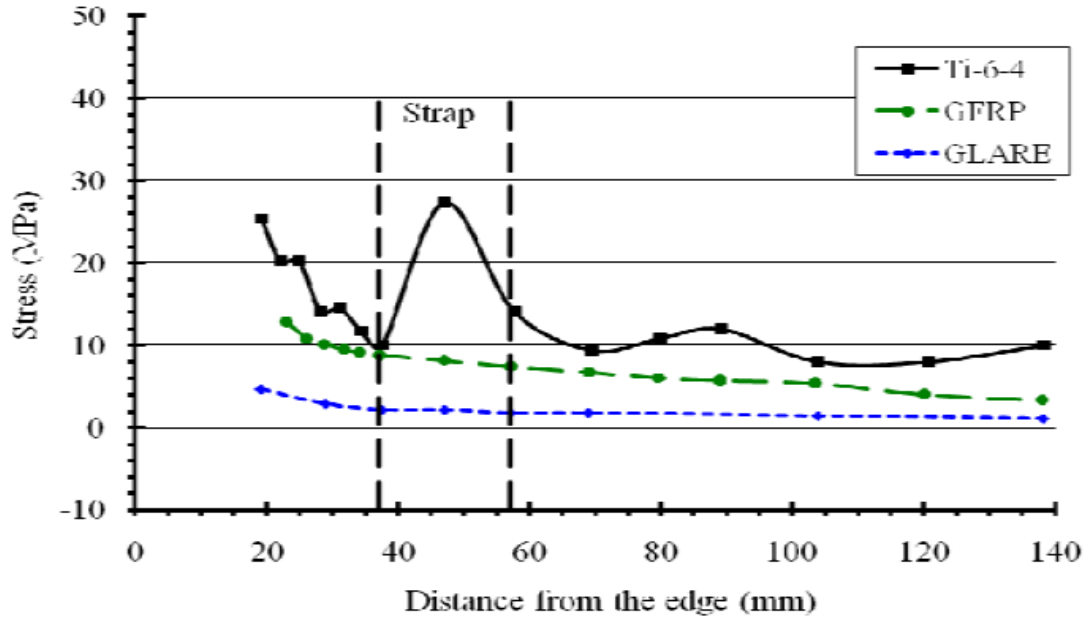

Figure 2.2: Measured longitudinal residual stresses (average values) in a 10 mm thick SENT sample bonded with 20 mm wide, 200 mm long straps. Measured residual stresses are 2.5 mm from the bond interface [15].

Ma et al.'s paper is aimed to the fatigue life extension through GLARE crack retarders bonded on the friction stir welded 7085-T7651 ESET specimen [19]. Prior to testing, specimens were cured at RT and 120 °C. The specimen cured at RT experienced longer fatigue life (factor 3.0) than the latter one (factor 2.4). The experimental study was supported by FE analyses incorporating thermal residual stresses. However, authors did not mention if the delamination behaviour had been included in the analyses.

Meneghin et al. both experimentally and numerically investigated the stiffened Al panels with Al and Ti BCRs [20]. The fatigue crack growth tests were supported by FE analyses comprising residual stresses. As can be seen in Fig. 2.3, the introduced residual stresses act together. The tensile stresses in the skin are balanced by the compressive stresses in the substrate. Authors observed a reduction in fatigue life as the ambient temperature decreases. At -50 °C, the retardation effect of Ti BCRs was non-existent. In other words, the crack needed 20% less cycles to reach the first stringer than crack in the panel without BCRs.

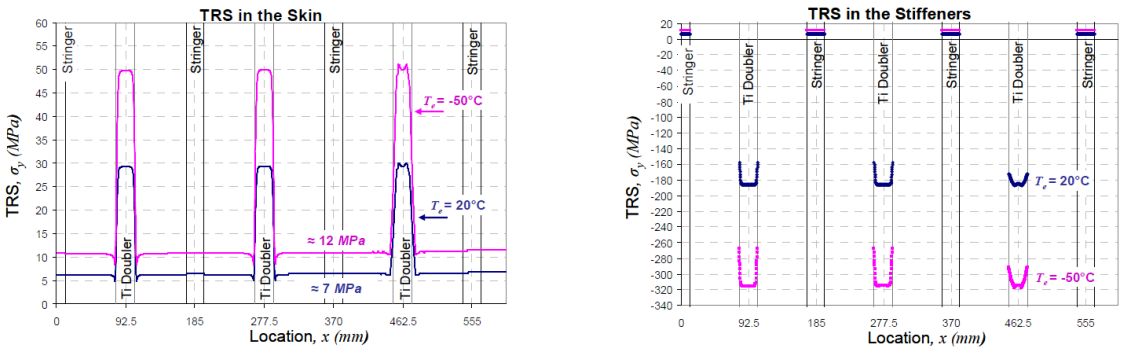

Figure 2.3: TRS induced in the skin and in the stiffeners of the intact stiffened panel with titanium doublers [20].

In 2012, Molinari et al. published an extensive parametric study on the panels reinforced by bonded, integral and riveted stringers with BCRs [21]. Authors developed an analytical tool named LEAF to predict the damage tolerance properties of stiffened structure. Although their technique comprises continuous delamination, residual stresses are omitted. It was concluded that the BCRs with higher width to thickness ratio are more effective in the retardation. With respect to the manufacturing technology, the bonded and riveted panels possessed the longest fatigue life.

Doucet et al. completed a FE model to predict a crack growth in the 2024-T351 M(T) specimen with GLARE BCRs in 2013 [22]. The main goal was to investigate the influence of delamination size and shape to the specimen's fatigue life. Although a detailed model for continuous delamination was included, residual stresses were not. Doucet in his PhD thesis refined the delamination model and incorporated thermal residual stresses calculation [23]. This three-dimensional modelling technique, called ReSLIC , calculates the delamination extent according to the loading mode and corresponding delamination law. The modelling technique was validated against specimen test results; GLARE BCRs bonded on 2624-T351 M(T) specimen increased the fatigue life by a factor of 1.17. No evidence of delamination (C-scan) during and after the test was observed. In addition to this test program, a series of riveted panels with and without BCRs and integrally stiffened FSW panel with BCRs was tested under VA loading. An increase in fatigue life was obtained in all riveted panels with BCRs. However, no general conclusions were derived for the in-

tegrally stiffened panel, because the bare panel was not tested and the test for panel with BCRs was preliminarily stopped due to the presence of cracks away from main crack. Based on experimental observation and FE modelling, Doucet concluded:

- BCR delamination has no effect on the substrate SIF in the case of M(T) specimens,
- BCR delamination has major effect on the substrate SIF in case of SEN(T) specimens,
- wider BCR at equivalent stiffness ratio promotes longer bridging effect and thus longer fatigue life,
- thicker substrate at equivalent stiffness ratio showed no change in fatigue life extension,
- secondary bending is one of the major influential mechanism defining the BCR effectivity.

Ma and Xu focused on the theoretical analyses of residual stresses in the friction stir welded ESET specimen with crack retarder in 2014 [24]. Authors did not mention the material used for the substrate and BCR, used delamination model and if residual stresses were included in analyses.

In 2015, Syed et al. analysed the 2624-T351 SENT specimen with GLARE crack retarders damaged by local impact [25]. The fatigue life of undamaged specimen with GLARE crack retarders increased by a factor of 2.3, whereas the specimens impacted with 35 J showed a 55% reduction in fatigue life when compared to the undamaged specimen. Furthermore, Syed's PhD thesis [26] studied the fatigue crack growth at specified temperature, after thermal cycling and after impact damage in various specimens made of 2624-T351 alloy. Residual stresses and their redistribution during fatigue crack propagation were also evaluated. Based on experimental work, Syed concluded:

- thermal cycling does not have significant effect on the fatigue lives of M(T) specimens with GLARE BCRs,

- the fatigue life of M(T) specimen with GLARE BCRs is almost identical to specimen without BCRs tested at -60 °C and +70 °C,
- load carrying BCRs bonded on M(T) specimen can significantly improve the fatigue life, compared to BCRs with shear load transfer.

2.2 Geometry modification

In 2006, Llopart et al. both experimentally and numerically investigated the influence of stringer geometry on the SIF and crack deviation in the 6013-T6 integrally stiffened panels [27]. Using the "double stringer flange", the biggest drop in the SIF was obtained. Authors concluded that as the SIF factor drops, the probability of change in the crack trajectory decreases. Apparently, a crack path can be deviated at the certain distance from a stringer, where stringer's influence on the SIF is negligible.

In 2008, Uz et al. published a paper about work on the 2139-T351 laser beam welded panels with systematic thickness variations, i.e. crenellations [28]. The panels were tested at the CA and VA loading. Authors experimentally verified that the fatigue life gain in the slow growth region (thin section) is always higher than the life shortening in the fast growth region (thick section). The crenellated panel showed approximately a 65% longer fatigue life compared to the reference panel of the same weight. Although an attempt to predict crack propagation was made, prediction was highly unconservative.

In 2004, Sepe et al. compared the fatigue life of chemically milled 2024-T3 panel with bonded panel during multi-axial loading [29]. Both panels were not stiffened by stringers. Bonding led to an increase in fatigue life by a factor of 1.5–2.0.

In 2015, Lu et al. completed a numerical study on fatigue life extension through crenellations [30]. An optimization procedure based on the genetic algorithm and FEA was used to find the most effective panel geometry in terms of crack retardation.

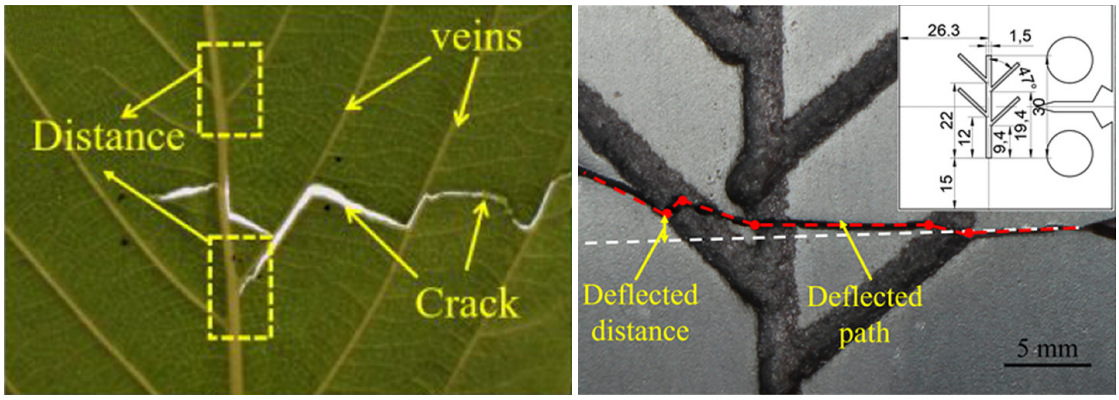

(a) Leaf (b) Specimen with leaf vein pattern.

Figure 2.4: Crack growth [31].

In 2020, Liu et al. laser cladded 2024 CT specimen with leaf vein pattern made of 7075 alloy [31]. Leaf vain patterns deflected the primary crack and initiated the propagation of secondary cracks (Fig. 2.4). Sacrificing a slight weight increase, the fatigue life increased by a factor of 1.4–2.3.

2.3 Cold spray

Jones et al. did an experimental study on the 2024-T3 M(T) and SENT specimens with deposited as-sprayed 7075 crack retarders in 2011 [32]. The main goal was to investigate the damage tolerance properties of cold sprayed structure. An ability of the 7075 CSCR to carry load during crack propagation was proved. Authors broadened the topic with experimental work on the riveted specimens with the cold sprayed 7075 layer in 2014 [33]. They investigated the possibility to seal the riveted join, repair adjacent cracked and corroded skin. The crack retarder did not delaminate and remained uncracked up to the crack length of 6 mm in the substrate. Moreover, the crack retarder withstood stresses up to 200 MPa under representative flight load spectra. At the end of the experimental study, crack retarders were deposited on the F/A-18 Hornet wing attachment centre barrel to demonstrate its ability to bond on a complex geometry and withstand bending moment spectrum. Authors concluded that further research is required to determine the upper stress limit before the crack retarders potentially delaminate or crack.

2.4 Residual stresses

Among other possibilities to slow-down the crack propagation, there are technologies introducing thermal or mechanical residual stresses. Well known shot peening and derived laser shock processing; these technologies have been proved to be successful at introducing mechanical residual stresses in various aircraft structures. It has been observed that the compressive residual stresses are generally of the order of 0.5–0.6% yield strength [34]. The thermal residual stresses can be introduced by the Electron Beam Suface Processing Technology and the Laser Surface Processing Technology.

Zhang et al. described the individual regions after electron beam irradiation in Al, Ti and Mg specimens [35]. A detailed analysis of the Al and Mg specimens revealed that the plastic deformation associated with the imparted stresses can extend over several hundreds of micrometres. Ivanov et al.'s evaluated the fatigue life of Al-Si specimen after electron beam irradiation [36]. An increase in fatigue life by a factor of 3.5. was obtained. Studies focused on lowering the fatigue crack growth rate in a wrought Al alloys by EBSP has not been published. On contrary, this technology appeared to be useful for reducing the crack growth rate in wrought steels [37], [38].

Schubel et al. modified the surface of 2198-T8 CT specimen by a laser to determine an effect on the specimen's fatigue life [39]. To lower the reflectivity of specimen, the SiC powder was deposited on a surface. After the irradiation, the thermal residual stresses and hardness profiles were measured. The irradiated specimen showed an increase in fatigue life by a factor of 3, but a decrease in the hardness in the heat zone and the heat-affected zone. The residual stresses were found to be similar to that found after welding. Authors attributed the increase in fatigue life to those stresses and not to microstructural changes. This study was further expanded to support the experimental results by FE analyses [40]. Input parameters for the VCCT were evaluated individually for the mechanical and thermal loading. Then the superposed loads were used as input variables for the Walker equation-based prediction. At the end, sensitivity analyses revealed a major impact of input parameters on crack growth prediction represented by a fatigue crack growth curves.

Groth et al. both experimentally and numerically investigated the laser-irradiated 2024-T3 CT specimens to evaluate the thermal residual stresses, microstructural and fatigue life changes [41]. Process parameters were optimized to ensure the highest levels of thermal residual stresses while maintaining a minimal surface deformation. An optimal position of the irradiated areas was determined using FE analyses calibrated by thermocouples. Only a slight increase in the fatigue life was obtained (factor 1.1). Authors expanded their research by a study on the number and shape of irradiated areas. The application of the dashed line pattern led to a greater decrease in the fatigue crack growth rate resulting in longer fatigue life (factor 1.2). Authors finally suggested the application of two lines to ensure a crack retardation independent of the location where a possible crack emerges.

In 2017, Cunha et al. expanded the topic to evaluate the effect of rolling direction [42]. It was not concluded that the rolling direction significantly affects the thermal residual stresses induced by the laser irradiation. Besides this, an increase in fatigue life by a factor of 1.6 was obtained in 2024-T3 CT specimens with the dark-coloured layer and two heated zones. Because the hardness decreased in the heat zone, authors suggested further research on mechanical properties of laser-irradiated area.

2.5 Consolidation

In 2013, Bird et al. reinforced the 2219-T851 and 2195-T8 specimens with the Al_2O_3 MetPreg™ [43] tape utilizing the Vacuum Hot-Pressing [44]. The combination of two matrices (Al and Al – 2 Cu) and two crack retarder locations were tested by the three-point bending test with the increasing loading amplitude. Although the fibres did not maintain the load-carrying capability at the end of the test, no delamination occurred.

In 2018, Hehr et al. did an experimental and numerical study on the 6061-H18 NASA LaRC Digital Twin specimens reinforced with the Al_2O_3 MetPreg™ tapes and 6061-H18 foils using the Ultrasonic Consolidation and CNC machining, i.e. the Ultrasonic Additive Manufacturing (UAM) [45]. Static FE analyses were used to determine location and the number of MetPreg™ layers. An increase in fatigue

life by a factor of 120 was identified. However, the authors did not mention the loading conditions and whether the load was proportionally increased for reinforced specimen.

2.6 Summary

The previously discussed studies are summarized in Tab. 2.1. With regards to the most efficient crack retarder design, one can find used material combinations (substrate/retarder) and fatigue life increases. To compare the individual technologies, other retardation techniques are also mentioned.

2.7 Prospects

It is apparent from the reviewed studies that the effectiveness of crack retarder is mostly determined by its:

· elastic modulus,

· coefficient of thermal expansion,

· delamination resistance.

The thermal residual stresses can be lowered by using the crack retarder made of material with higher CTE. Some steels possess the CTE close to the substrate's value. Additionally, due to the high elastic modulus of steel, more load can be transferred from the substrate. However, the relatively high density of steel probably impeded its application to crack retarders.

The application of CF crack retarders always leads to a high level of thermal residual stresses both in a substrate and crack retarders. Using the fibre metal laminate crack retarder, the thermal residual stresses can be lowered. This has been successfully achieved by the GLARE crack retarders. Studies focused on the application of CARE crack retarders are lacking.

Table 2.1: Summary of crack retarder studies.

Technology	Year	Main Author	Substrate	Al	Ti	Steel	CF	GF	BF	AlF	ARALL	GLARE	CARE	Longest life	LEF	σ_{max} [MPa]	R	T_{test} [°C]	T_c [°C]
BCR	1989	Schijve	2024-T3	*	*						*			ARALL	2.0	88.3	0.33	RT	120
	2004	Farley	7075							*				AlF	5.0	6.9	0.1	RT	?
	2005	Zhang[a]	2024-T351		*		*							CF	3.5	138	VA		
	2006	Colavita	2024-T3				*							CF	3.0	70	0.1	RT	RT
	2008	Zhang	7085-T7651		*		*	*						Ti	1.6	18.57	0.1	RT	120
	2009	Liljedahl	7085-T7651		*		*							Residual stress study				RT	120
	2011	Liljedahl	7085-T651		*									Residual stress study				RT/-50	120
	2011	Irving	7085-T7651	*	*		*					*		Al	3.8	17	0.1	RT	120
														GLARE	2.7	60	0.1	RT	120
	2011	Brot	2024-T351				*		*					CF	2.0	85.6	0.1	RT	120
														CF	6.5	85.6	0.1	-50	120
	2011	Ma	7085-T7651									*		GLARE	3.0	64.29	0.1	RT	RT
														GLARE	2.4	64.29	0.1	RT	120
	2015	Syed	2624-T351									*		GLARE	2.3	60	0.1	RT	120
	2015	Doucet	2624-T351									*		GLARE	1.2	60	0.1	RT	121
	2017	Jetela	**2024-T351**			*	*									60	0.1	RT	80
CSCR	2011	Jones	2024-T3	*										Al	1.4	93.36	0.1	RT	
	2018	Jetela	**2024-T351**		*	*										60	0.1	RT	
VHPCR	2013	Bird	2219, 2195							*				Bending fatigue				RT	299-499
UCCR	2018	Hehr	6061-H18							*				AlF	120.0	?	0.1	RT	
	2022	Jetela	**2024-T351**		*											60	0.1	RT	
GM	2008	Uz	2139-T351			Machined crennelations									1.65	50	0.1	RT	
	2014	Sepe	2024-T3			Bonded crennelations									2.0	50.96	0.04	RT	?
	2020	Liu	2024			Leaf vain pattern									2.3	?	0.1	RT	
RS	2015	Ivanov	Al-Si			Electron Beam Surface Treatment								Bending fatigue				RT	
	2012	Schubel	2198-T8			Laser Shock Processing									3.0	7	0.1	RT	
	2014	Groth	2024-T3			Laser Shock Processing									1.1	103.8	0.1	RT	
	2017	Cunha	2024-T3			Laser Shock Processing									1.6	7	0.1	RT	

[a]FEA

An increase in the delamination resistance increases the effectiveness of load transfer from a substrate causing longer fatigue life. This can be achieved by increasing the lap shear and peel bond strength of interface. Cold spray is a new technology and thus not a large number of studies focused on the crack retardation have been carried out [46]. The previously mentioned studies dealt only with Al crack retarders applied on Al substrate. Although cold sprayed Ti [47] [48], Al and steel [49] [50] coatings were evaluated in terms of the microstructural properties and process parameters, the impact of such coatings on crack propagation have not been published. A potential increase in fatigue life can be expected due to higher adhesion of such coatings.

Besides mentioned technologies, a high-strength bond can be attained by the TLP diffusion bonding. The TLP diffusion bonding process differs from the diffusion bonding in utilizing lower clamping forces and temperatures below the melting point using various thin interlayers, which changes local chemical composition at the interface and lowers the temperature for bond creation. In 2010, Alhazaa et al. measured the shear strength of 42.3 MPa of diffusively bonded 7075/Ti-6Al-4V joint [51]. The following process parameters were used: 500 °C/1 MPa/1 hour. In 2014, Samavatian et al. achieved the shear strength of 36 MPa of a 2024/Ti-6Al-4V joint utilizing Cu/Sn/Cu interlayer [52]. The joint was created at 510 °C for 1 hour. Authors replaced the interlayer with the Cu/Zn/Cu but only a slight increase in the shear strength (37 MPa) was achieved [53]. A much greater increase was accomplished by Anbarzadeh et al [54]. Using the Sn/Ag/Bi interlayer and two-stage TLP diffusion bonding at 620 °C and 453 °C, they measured the shear strength of 62 MPa.

Other additive technologies like the SLM and DLD might be useful in a crack retarder fabrication. Rapid solidification could lead to a high-strength bond between a crack retarder and substrate, and thus greater delamination resistance. A major disadvantage of additive technologies is a large number of process parameters that have to be selected carefully to lower the porosity and obtain good mechanical properties. Moreover, multi-material structures cannot be heat treated sufficiently due to the dissimilar melting temperature of individual materials, e.g. the Ti/Al

combination. In 2015, Shamsei et al. suggested further research in process parameters to obtain good mechanical and fatigue properties of laser-deposited parts [55]. However, technologies of liquid-state joining of dissimilar reactive metals are often accompanied by the growth of brittle intermatellics at the interface, resulting in the poor mechanical properties of joint [56].

The input thermal energy from ultrasonic welding is 70–80% lower [57], in comparison to e.g. SLM. Only one study on the crack retardation through ultrasonically consolidated Al_2O_3 crack retarders was found, although an intermetallic-free joint between other reactive metals, e.g. Ti and Al, has been successfully achieved. Zhang et al. measured the shear strength of 100 MPa of 2139-T8/Ti-6Al-4V joint [58]. However, the temperature during the ultrasonic welding rose to 550 °C and thus the joined metals had to be aged. Wolcott et al. determined the shear strength of 46 MPa of a Ti/1100 Al joint [59]. Although the subsequent thermal treatment triggered the formation of intermetallic compounds, the shear strength of such joint increased to 102 MPa. Authors hypothesized that this intermetallic layer acts similarly to the thin braze layer, and the biaxial stress state leads to an increase in the shear strength.

A few evident research gaps were marked with bold asterisk (Tab. 2.1) in the last row of sections: BCR, CSCR and UCCR. The combination of such technologies and materials was chosen as a subject of research in this thesis. The exact material combinations and specimen geometry are specified in the Chapter 3.

Chapter 3

Aim and Objectives

The main aim of this thesis is to compare the impacts of bonded and additively manufactured crack retarders on the fatigue crack growth in the metallic structure. To address this aim, individual objectives are enumerated in subsequent points:

1. To measure the performance of steel bonded crack retarders. The 2024-T351 M(T) specimens with the AISI 301 bonded crack retarders will be prepared to perform the fatigue crack growth test incorporating delamination monitoring.

2. To measure the performance of additively manufactured crack retarders. The 2024-T351 M(T) specimens with the AISI 316L, Ti-6Al-4V cold sprayed crack retarders will be prepared to perform the fatigue crack growth test incorporating delamination monitoring. The 2024-T351 M(T) specimens with the AISI 301/Al crack retarders will be prepared to perform the fatigue crack growth test incorporating delamination monitoring.

3. To compare the bonded crack retarders with additively manufactured ones and find the most effective crack retarder in terms of life extension, weight and delamination resistance.

Chapter 4

Theory

4.1 Linear Elastic Fracture Mechanics

4.1.1 Loading modes

There are three distinctive crack loading modes. Mode I that opens the crack faces, Mode II that slides the crack faces and causes in-plane shear and Mode III that introduces out-of-plane shear [60]. The modes are useful to determine the individual contribution to crack loading. In many real structures, the mixed-mode loading occurs.

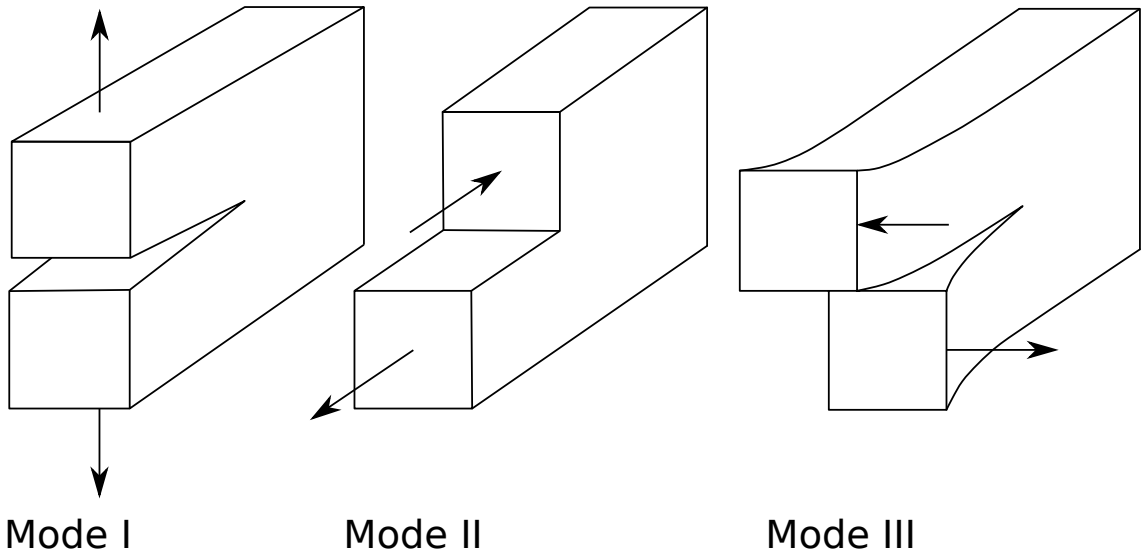

Figure 4.1: Crack loading modes [60].

Fatigue microcrack grows along the initial slip band orientation. However, the fatigue macrocrack have the strong tendency to grow perpendicular to the main principle stress (Mode I). Thus, Mode I falls exclusively within the scope of this thesis.

4.1.2 Stress Intensity Factor

To describe the stress severity around the crack tip, Irwin [61] proposed the concept of stress intensity factor, which originates from the linear elastic solution for the stress field around a crack. The solution in polar coordinates (Fig. 4.2) is given by

$$\sigma_{ij}(r,\theta) = \frac{K}{\sqrt{2\pi r}} f_{ij}(\theta) + \text{'other terms'} \tag{4.1}$$

with

$$K = \sigma\sqrt{\pi a} \tag{4.2}$$

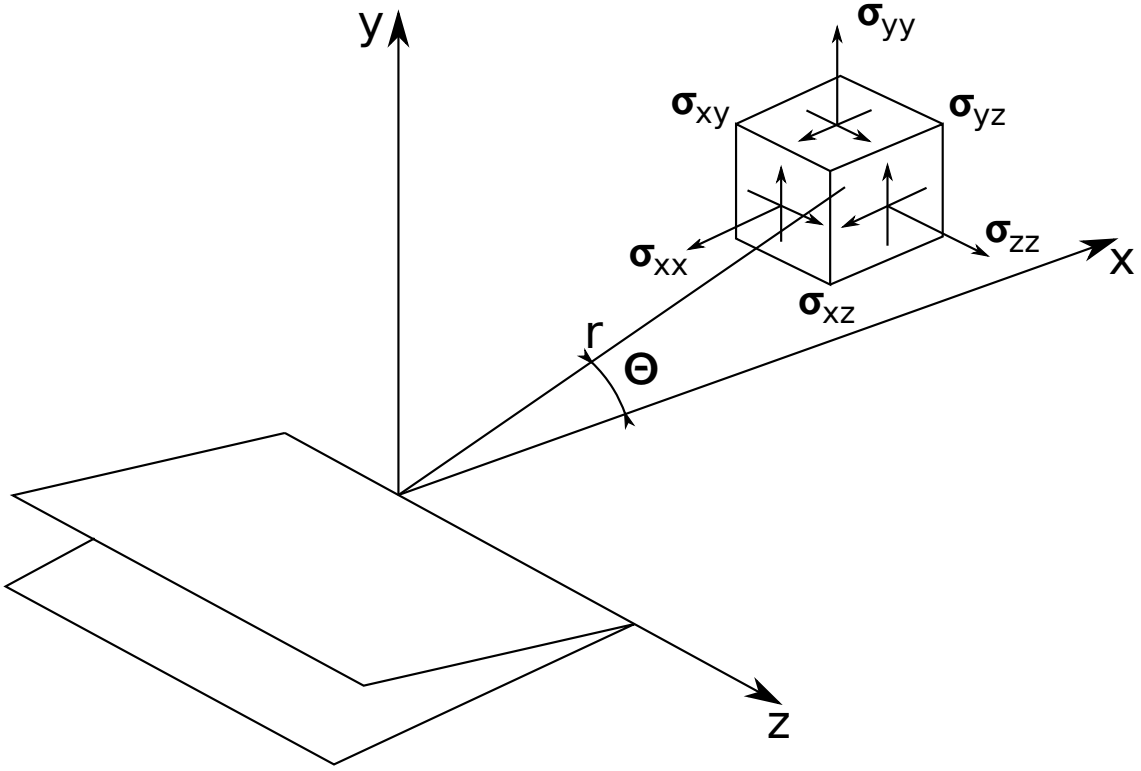

Figure 4.2: Crack tip coordinate system and stress components.

In those equations, σ_{ij} is the stress tensor, K is the stress intensity factor, σ is the uniform external stress field, a is the crack length and the f_{ij} is the angular distribution function. Angular distrib. function determines the distribution of the stresses near the crack tip along the circumference direction. The 'other terms' are negligible if the point is sufficiently close to the crack tip.

The Equation (4.2) defines the stress intensity factor of crack in the infinite plate. However, this does not reflect conditions in the real structures with finite dimensions. For this reason, the geometry correction factor β was added to the equation:

$$K = \sigma\beta\sqrt{\pi a} \tag{4.3}$$

The stress intensity factor data or geometry correction factor data can be obtained from:

- Literature (e.g. [62], [63], [64])
- Numerical Methods (e.g. Direct method)

  Finite Element Method [65]

  Boundary Element Method [66]

  Finite Difference Method [67]
- Analytical Methods

  Green's functions [68], [69]

  Westgaard's solution to Airy's stress functions [70] [71]

  Weight functions [72]
- Experimental Methods

  Strain gauges [73]

  Photoelasticimetry [74]

  Crack Opening Displacement measurement [75]
- Empirical methods ($da/dN - \Delta K$ relation, Superposition)

This is not the comprehensive review of all methods to estimate the K factor. Many other methods have been developed, mostly combinations. It should be pointed out that analytical methods were generally derived for idealistic geometries and thus numerical methods must be performed for more complex geometries.

Crack displacement field

Displacement field close to the crack tip for the through-thickness cracked plate can be written as

$$u_i = \frac{K}{2G}\sqrt{\frac{r}{2\pi}} f_i(\theta) \tag{4.4}$$

with

$$G = \frac{E}{2(1+\nu)} \tag{4.5}$$

Reducing the crack opening displacement (u_x), the K and crack growth rate $\frac{da}{dN}$ decrease. This is an essential crack growth retarding mechanism attributed to crack retarders and will be discussed further in the Section 4.5.

4.1.3 Plane stress and plain strain

The material far from the specimen's surfaces possesses three dimensional stress state [76]. The third stress component evolves because the material can not contract in thickness direction due to the surrounding material and therefore $\epsilon_z = 0$, where ϵ_z is the strain in the thickness direction. On specimen's surface, where surrounding material does not longer exist on one side, the material can contract in the thickness direction and thus $\epsilon_z \neq 0$ (Fig. 4.3). Please note that b stands for specimen thickness.

From von Mises yield criterion can be derived that stresses in the plastic zone are 2.5 times higher[1] under plain strain conditions than under plane stress conditions [60] and thus the K may differ from specimen's surface to interior. In terms of crack growth rate in solid specimen, the crack grows slower on specimen's surface. This often leads to through-thickness crack with curved crack front.

[1] materials with Poisson's ratio $\nu = 0.3$

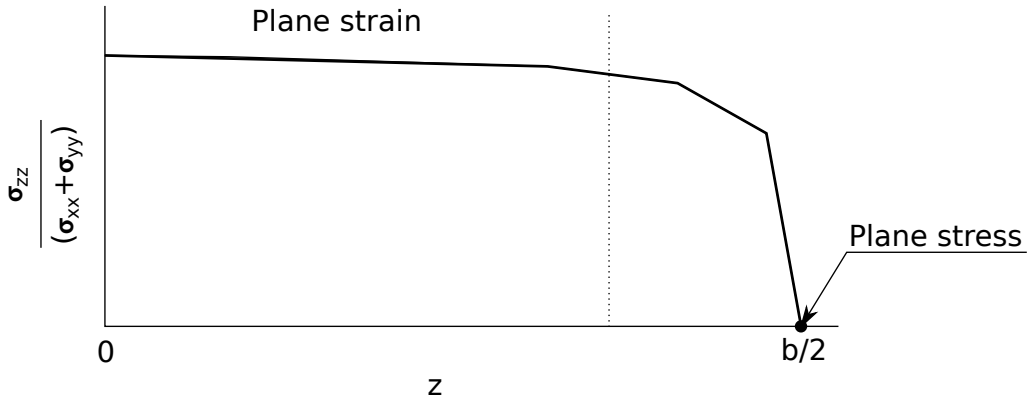

Figure 4.3: Variation of the plane-strain constraint $\sigma_{zz}/(\sigma_{xx} + \sigma_{yy})$ along the crack front [76].

During the comparative crack growth tests with laminated and solid specimens [77], the plane stress conditions were observed in the internal metallic layers of laminated specimen. The crack grew independently in the individual layers which resulted in the longer fatigue life of laminated specimen. Similarly, this mechanism restricts the crack growth in the layers of laminated crack retarder.

Strain energy release rate

The Griffith's energy available for an increment of crack extension $-\frac{d\Pi}{dA}$ [78] was reformulated by Irwin [79] using the energy release rate (crack driving force) G.

$$G = -\frac{d\Pi}{dA} = \frac{\sigma^2 \pi a}{E} \tag{4.6}$$

Inserting the Equation (4.2), the $G - K$ relation is given by:

$$G = \frac{K^2}{E} \qquad \text{Plane stress} \tag{4.7}$$

$$G = \frac{K^2}{\frac{E}{1-\nu^2}} \qquad \text{Plane strain} \tag{4.8}$$

The FEA and VCCT method [80] are often used to determine G in the Equations (4.7) and (4.8). Obviously, this approach has been widely used to predict K in cracked structure with bonded crack retarders [3], [11], [20], [81] or with laser-irradiated zones [40].

4.2 Fatigue crack growth

4.2.1 Stress Cycle

During fatigue loading, the stress level changes with time (Fig. 4.4), between σ_{max} and σ_{min} stress levels. The mean stress σ_m lies exactly between those stress levels in the distance of σ_a. Stress ratio, important stress cycle characteristic, is then given by R.

$$R = \frac{\sigma_{min}}{\sigma_{max}} \tag{4.9}$$

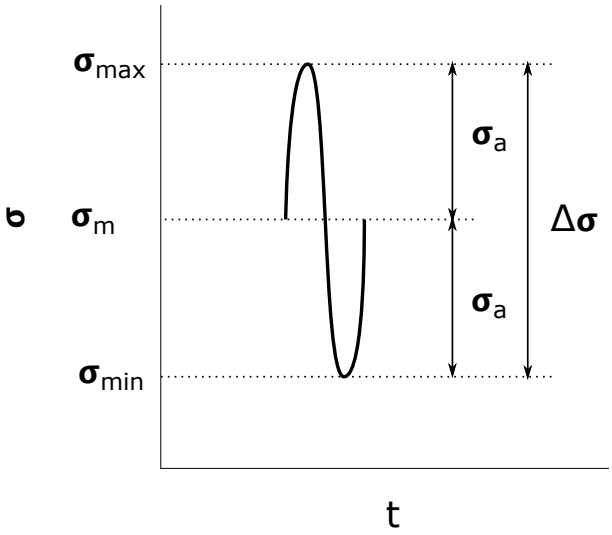

Figure 4.4: Stress cycle [82]

Tests performed in the experimental section were done at $R = 0.1$. Such ratio closely approaches service conditions of the lower wing panel that is subjected to steady and alternating tension loadings.

4.2.2 Stress Intensity Factor Cycle

Because the external load σ varies with time, the stress intensity factor (4.2) varies between K_{max} and K_{min} levels and so the stress intensity factor cycle (or range) is thus defined by

$$\Delta K = \Delta\sigma\beta\sqrt{\pi a} \tag{4.10}$$

and the stress ratio

$$R = \frac{\sigma_{min}}{\sigma_{max}} = \frac{K_{min}}{K_{max}} \tag{4.11}$$

The knowledge of the stress intensity factor range can be used for crack growth prediction using the similarity principle. If two specimens with unequal crack lengths are loaded by unequal load cycles but their ΔK and R are the same, the crack extension in both specimens should be same. Subsequently, the crack growth in structural component can be predicted using the crack growth data of the basic specimens (e.g. M(T), CT) if the β or the $\Delta K(a)$ relation for the structural component is known.

4.2.3 Fatigue life

Fatigue life consists of two periods (Fig. 4.5):

1. crack initiation: cyclic slip, microcrack nucleation and their growth

2. crack growth period: macrocrack growth and failure

Large portion of fatigue life is spent during the first period, where fatigue crack is affected by microstructural properties. First period usually happens near a material's free surface where the maximum stress levels occurs due to the presence of stress concentrators[2]

In the second period, crack is affected by material bulk properties and atmospheric composition [82]. Crack retarders are meant to be a structure's macrofeature so their positive effect on a fatigue life manifests in the second period.

[2]e.g. corners, scratches, particles and voids

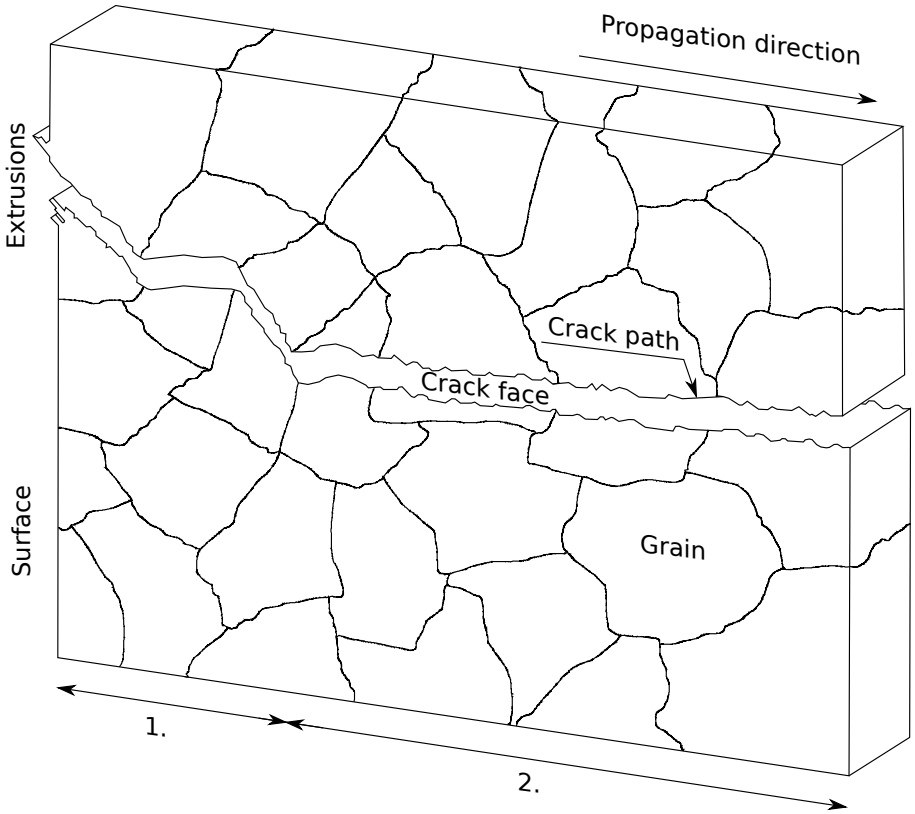

Figure 4.5: Fatigue life periods [83].

Macrocrack growth and failure

The previously discussed period of macrocrack growth and failure is subdivided into three regions:

I. Threshold region,

II. Paris-Erdogan region,

III. Stable tearing region.

Threshold region The $\frac{da}{dN} - \Delta K$ curve (Fig. 4.6) declines asymptotically towards threshold value of stress intensity factor cycle ΔK_{th}. If $\Delta K < \Delta K_{th}$, the fatigue macrocrack stops growing. However, microcrack can still grow at this region. K_{th} strongly depends on R [84] and therefore it is not the stand-alone material constant. The near-threshold region is defined by the *operational* ΔK_{th} which corresponds to fatigue crack growth rate of 10^{-10} m/cycle [85].

Paris-Erdogan region Paris and Erdogan [86] proposed the first empirical crack growth law, $\frac{da}{dN} - \Delta K$ relation, to describe fatigue crack growth in the second period. This relation set up a basis for more complex laws incorporating geometry of crack growth and plasticity based constitutive behaviours.

$$\frac{da}{dN} = C(\Delta K)^n \tag{4.12}$$

where C and m are material constants. The $\frac{da}{dN} - \Delta K$ relation defines the fatigue crack growth resistance of a material [82]. To cover fatigue crack growth in all three regions, Forman and Mettu [87] introduced the so-called NASGRO equation:

$$\frac{da}{dN} = C_{FM} \left[\left(\frac{1-\gamma}{1-R} \right) \Delta K \right]^n \frac{\left(1 - \frac{\Delta K_{th}}{\Delta K}\right)^p}{\left(1 - \frac{K_{max}}{K_C}\right)^q} \tag{4.13}$$

where γ is the Newman's crack opening function [88], K_C is the fracture toughness and C_{FM}, n, p, q are material constants (Fig. 4.6). The equation 4.13 is implemented in various fatigue crack growth predicting softwares frequently used in aerospace industry.

Mechanism and fracture surface characteristics Fracture surface is covered with parallel grooves that are perpendicular to crack growth direction, i.e., striations (Fig. 4.7: (1), (2)). From the striation spacing, the microscopic crack growth rate can be calculated. In this region, microscopic crack growth rate is approximately equal to macroscopic crack growth rate (e.g. observed on the material's surface).

Regarding the origin of striations, the three major theories were proposed: The plastic blunting [89], [90]; the concept of slip step [91], [90] and the alternating slip model [92], [93]. Although, the plastic blunting model is considered to describe the striation forming in ductile materials, a novel study of Pippan et al. sees their formation as a more complex problem [94].

Stable tearing region The $\frac{da}{dN} - \Delta K$ rises asymptoticaly towards the K_C. The growth is accelerated and thus crack growth life spent in this region is very short. When $K_{max} = K_C$, failure occurs.

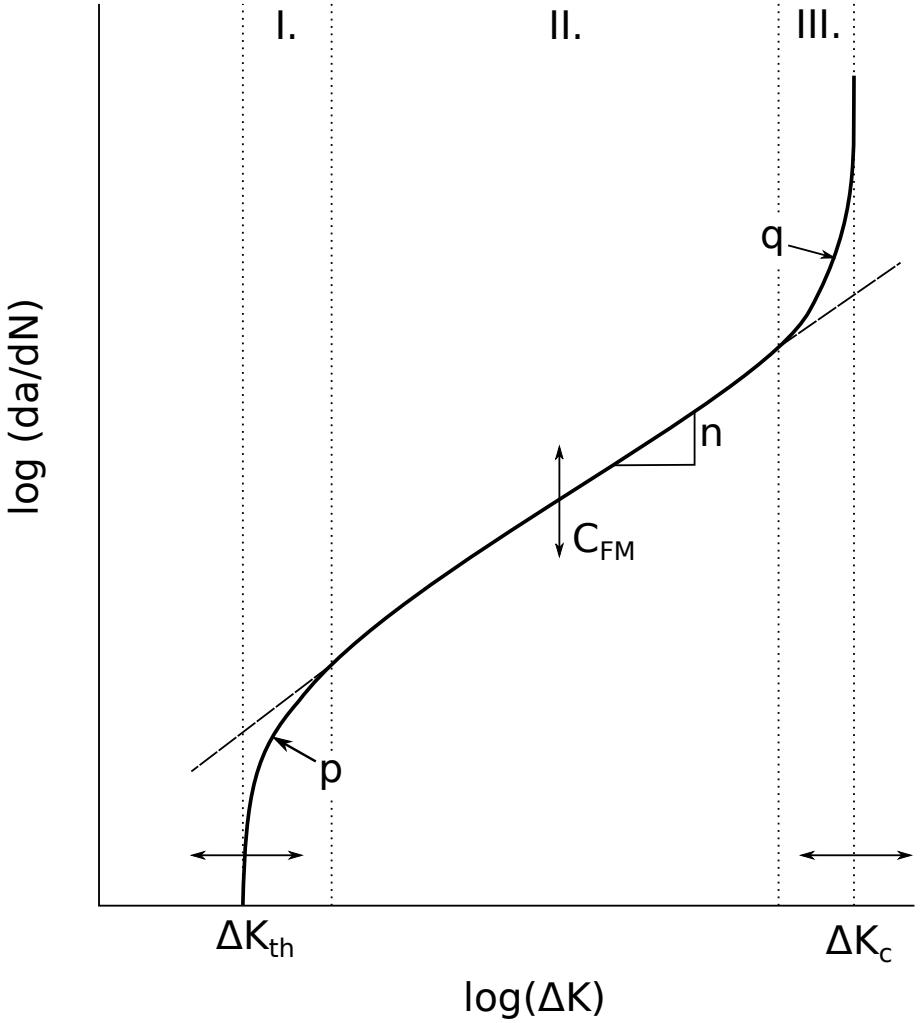

Figure 4.6: Fatigue crack propagation curve with marked macrocrack growth regions and influences of NASGRO equation parameters on her shape [95].

Mechanism and fracture surface characteristics The local areas of ductile tearing[3] and/or cleavage[4] (static processes) are spaced between striations (fatigue process) [82], [60] (Fig. 4.7). Both static mechanisms are becoming predominant over fatigue mechanism with increasing K_{max} [60]. Because the ductile tearing is highly localised, the crack growth is stable process [82].

[3]Ductile tearing areas emerges as the the consequence of microvoid nucleation, growth and coalescence.

[4]Only in specific materials at specific temperatures.

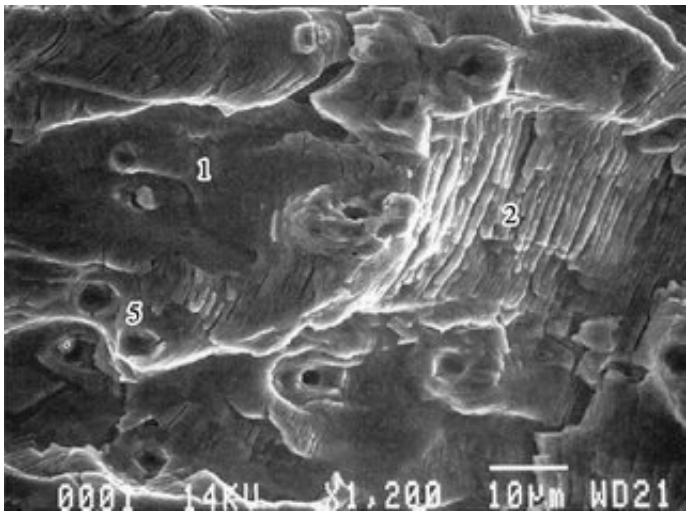

Figure 4.7: Features of 2024-T351 alloy fracture surface: (1) Ductile striations, (2) Fragile striations, (5) Dimples of ductile tearing. Adapted from [96].

4.3 Effects on macrocrack growth and life

This chapter deals with the effects on crack growth in aluminium alloys at the constant amplitude cyclic loading. An emphasis is placed on the 2024-T351 alloy that is used as substrate in the experimental section.

Microstructure A few opposite conclusions were drawn on the role of microstructure in the macrocrack growth region. Wanhill elucidated [84] that the grain size effect cause the multiple linear sections in the near-threshold region in the 2024 alloy in T351 and T3 tempers. A corellation between the plastic zone sizes and the characteristic microstructural dimensions[5] was found. On the contrary, Xu et al. concluded that the grain size effect rather impacts the crack closure [97]. Moreover, a substantial contraction of Paris-Erdogan region was observed as the crack grew from conventional dendritic structure to directional dendritic structure [98] in 2024 alloys. The rolled sheets and plates possess directional microstructure that manifests in anisotropic mechanical properties. In the 2024-T351 plate, the crack growth rate was found to be somewhat lower in the L-T direction than in the T-L direction [99].

[5]mean planar distance between dispersoids, subgrain and dislocation cell sizes, grain dimensions

Batch-to-batch differences A significant variability in the da/dN was observed between batches of 2024-T3 alloy. Interestingly, variability between batches from one manufacturer was nearly identical to the variability between batches from various manufacturers. The da/dN variability was found to increase with increasing ΔK [100]. Eventually, the crack growth life was approximately doubled [82].

Heat treatment The comparative study of 2024 alloy showed that changing the temper from T351 to T3, the fatigue crack growth life can increased by a factor 1.5 at $R = 0.1$. A more substantial increase by a factor 4.4 was observed at $R = 0.5$ [101]. The changes in crack growth rate between different tempers are attributed to changes in yield strength. A high strength materials generally possess poor fatigue crack growth resistance [82].

Atmosphere The effect of atmospheric composition is attributed corrosion mechanism. Corrosion is time, material and environmental dependent problem. The synergic effect of corosion and cyclic loading is a broad topic and thus only a few remarkeable studies attributed to the aluminium alloys are mentioned there. The immersion in distilled water speeds up the macrocrack growth in the 2024-T351 alloy [102]. Generally, the saline solution might increase the crack growth rate even more. The alternating immersion have greater impact on crack growth rate than the persistent immersion [103]. Especially in the 2024-T351 alloy loaded in the corrosive enviroment, the decrease in loading frequency decreases the crack growth rate (opposite behavior). The alloy's sensitivity to the load rise time rather than the loading frequency in 2024-T351 alloy was observed [104]. Obviously, a substantial decrease in the crack growth rate in the 2024-T351 alloy was observed in high-vacuum [103]. Such behaviour is common for all metallic materials that are fatigued in the inert environment. The fracture surface observations revealed that the vacuum suppresses the striation formation. This finding suggests that the environment have major impact on macrocrack growth [105]. The oxygen and helium are the inert atmospheres and does not contribute to the crack growth rate increase in the 2xxx alloys [106], [107]. However, the presence of water vapours in the inert atmosphere might affect the crack growth rates significantly. With increasing

water vapor pressure, the crack growth rate increases [108]. Commonly proposed corrosion fatigue mechanisms related to the crack growth rate increase in the moist environment are anodic dissolution and hydrogen embrittlement [103], [105].

Stress ratio effect Sometimes called called the "mean stress effect". As the stress ration increases, a cracked part spends more time in tension and thus crack has more opportunities to advance. This increase shifts the entire fatigue crack propagation curve (Fig. 4.6) up and to the left [109].

Temperature Testing the crack growth response of 2024-T351 alloy at elevated temperature revealed that the temperature increase from 22 °C to 204 °C had only a slight effect on the crack growth rate [110], although interestingly, the tensile and yield strength both changed. Results at -54 °C showed the decrease in fatigue crack growth rate at near-threshold region (lower ΔK_{th}). However, at higher ΔK the crack growth rates were about the same [111]. The crack growth rate decreased probably due to the lower water vapour pressure at -54 °C. Intuitively, the presence of corrosive environment at high temperatures speeds up the corrosion processes and subsequently the crack growth rate.

Thickness effect The crack growth rate decreases with decreasing thickness of the 2024-T3 specimen [112], [113]. It was found that the changes in stress state are responsible for discrepancy in the crack growth rate (elaborated in Subsection 4.1.3).

Loading frequency In 2024-T3 alloy, a substantial increase in the crack growth rate due to the decreasing loading frequency was observed in both dry and wet air [114].

Residual stresses The constant ΔK fatigue crack growth test of 2024-T351 M(T) specimen revealed an increase in the crack growth rate as the crack passed the area with the tensile residual stresses. A drop in the crack growth rate was observed in

the CT specimen as the crack approached the area with the compressive residual stresses. The residual stress fields were introduced by welding process [115], [116].

4.4 Manufacturing technologies

Three distinctive technologies are used to fabricate crack retarders in this thesis: the adhesive bonding, cold spray and ultrasonic consolidation. This chapter describes them in detail with a particular focus on underlying bond formation mechanisms.

4.4.1 Cold Spray

Cold spray is an additive technology that was developed by Anatolii Papyrin and his colleagues in Novosibirsk, Russia [117]. The technology allows to deposit coatings on various substrates. Deposited coating often exhibits the outstanding adhesion strength in combination with low thermal affection of both the coating and substrate.

Process description

The solid particles and heated gas are separately fed into the convergent-divergent nozzle (Fig. 4.8). As the heated gas expands in the nozzle, his temperature decreases while the velocity increases. The particle then enters the expanding flow and her velocity also increases. The accelerated particle travels the stand off distance before impacting the substrate. Upon the impact, the particle and/or substrate are plastically deformed and the bond between substrate and particle is realized. Cold spray gun is mounted on robotic arm that allows her: (1) to travel along the predefined path at certain speed and (2) to maintain constant stand off distance from the substrate.

There are a few process parameters that must be adequately set to obtain dense coating: gas pressure, gas temperature, gas composition, gas flow rate, powder feed rate, particle size and morphology, gun travel speed, gun stand off distance, gun step distance. Some of these parameters are not self-explanatory and thus will be discussed bellow.

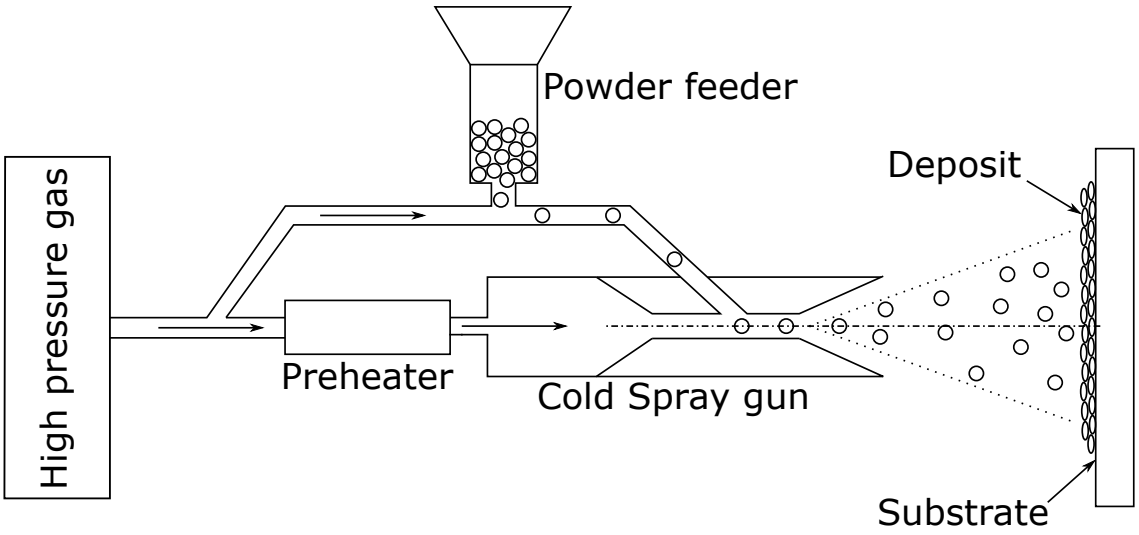

Figure 4.8: Cold Spray apparatus. Adapted from [118].

Nitrogen, helium or air are mostly used in the cold spray process [119]. Particle morphology describes the shape of the particles in used powder. Powder having the spherical, irregular or sponge particle morphologies is often used [120]. Gun travel speed is the relative speed between Cold Spray gun and substrate. Gun stand off distance is the distance between substrate and Cold Spray gun nozzle. Gun step distance is the is the distance of two neighbor spraying passes.

To create bond between particle and substrate, the particle velocity upon impact v_{pi} must achieve the certain level, critical velocity v_{cr}. If $v_{pi} < v_{cr}$, the bond is not created and the particle rebounds from the substrate. In other words, the critical velocity marks the transition from the substrate erosion to the the coating formation. For metals, the critical velocity is within $500 - 700$ m/s range and decreases with increasing gas temperatures [117].

The v_{pi} increases with increasing gas pressure and temprature [121]. However, increasing gas temperature may negatively affect the substrate and particle properties [117]. The v_{cr} decreases if particle size and density decreases. In contrast, the increase in particle hardness, specific heat and melting temperature increases the v_{cr} [121].

Bond formation

A solid-state bonding at high strains arguably leads to the bond formation between particle and substrate. This bonding requires the atomic-flat and oxide-free surfaces brought into the intimate contact. One way to achieve such surface conditions is the interfacial plastic deformation [122].

Such deformation takes place during the high-velocity impact of two solid objects. The high-velocity impact promotes a high contact pressures in both solid objects; the shear strengths of contacting objects are vastly exceeded. Consequently, material starts to act as a fluid and a jet is formed (Fig. 4.9a). This material behaviour is called Adiabatic Shear Instability[6] (ASI) and takes place at $v \geq v_{cr}$. The ASI and subsequent bond formation occurs locally; the bond is not realized on the entire interface. It is worth noting that there is an ongoing research on bonding in cold spray and the ASI may not be the sole bonding mechanism. Historically, the ASI and jet formation were first observed during the explosive welding (Fig. 4.9b), magnetic pulse welding and dynamic powder compaction [122], [123].

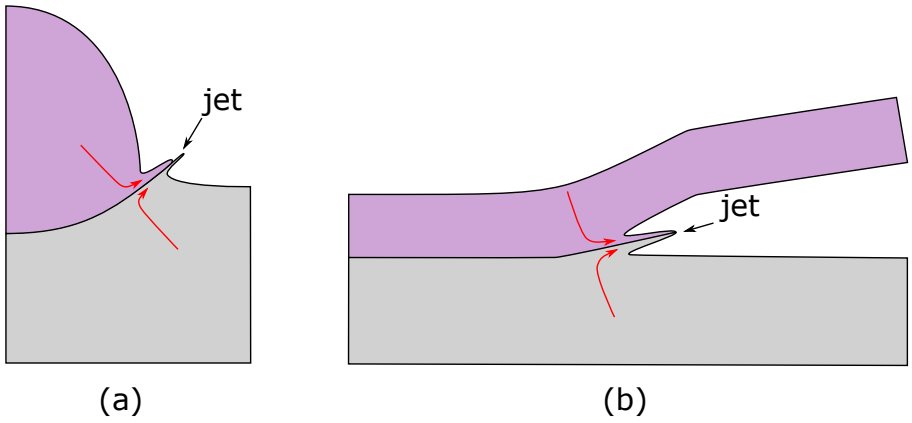

Figure 4.9: Deformation localisation due to the Adiabatic Shear Instability during: (a) cold spraying, (b) explosive welding. Adapted from [122].

In this thesis, the stainless steel and Ti-alloy are deposited onto the Al-alloy substrate to create the crack retarders. When dissimilar material combinations are being bonded, the ASI is limited in the harder and denser material. Combining the "softer" substrate and "harder" particles, the bonding is also governed by mechanical interlocking [122] (Fig. 4.10).

[6] no heat is transferred from the interface

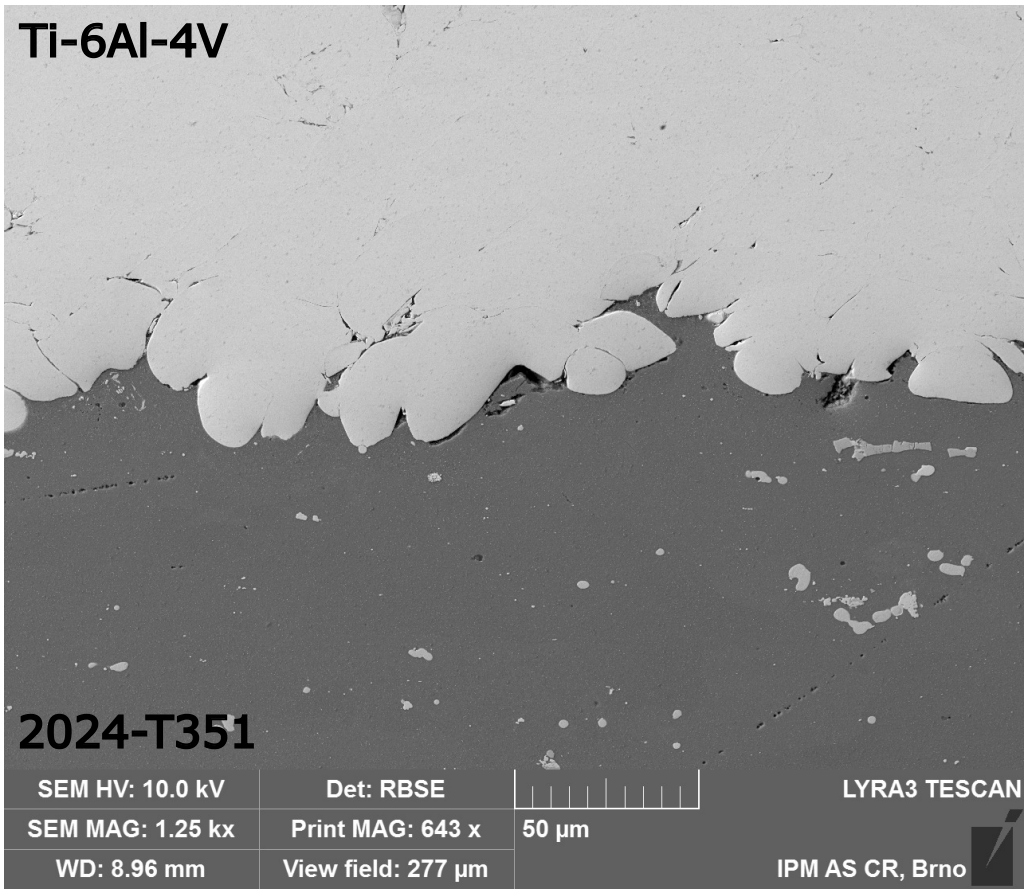

Figure 4.10: Interface between the Ti-6Al-4V crack retarder and the 2024-T351 substrate.

Coating characteristics

Mechanical properties Coatings in as-sprayed conditions often exhibit low strength, ductility and high porosity [124]. The mechanical properties of deposited Ti-6Al-4V and 316L alloys used for the fabrication of crack retarders in this thesis are no exception (Tab. 5.7). Generally, poor mechanical properties can be improved by Hot Isostatic Pressing. However, this approach is not applicable in case of material combination where optimum processing temperature of certain material is the melting temperature of other material. For this reason, the cold-sprayed crack retarders were tested in as-sprayed conditions.

An adhesive strength up to the 140 MPa of Cu coatings on Al substrate was achieved using the N_2 carrier gas [125]. The adhesion strength about 80 MPa of 316L coatings on Al substrate was attained using the same gas [126].

Residual stresses Mechanical[7] and thermal residual stresses may emerge in both coating and substrate upon cold spraying. While the first one evolve as a result of highly localised plastic deformation; the latter one is attributed to the temperature rise due to the impinging jet [127] and CTE mismatch (coating/substrate). The plastic deformation is believed to have little to no effect on the substrate temprature [128].

Suhonen et al. deposited the Ti coating on the Al substrate and in situ measured the compressive residual stresses of the order of 150 MPa in the Ti coating. Moreover, the compressive residual stresses of the order of 90 in the Cu coating deposited on the Al substrate were observed. They concluded that the compressive residual stresses in the coatings are directly proportional to the CTE difference between coating and substrate [129].

4.4.2 Adhesive bonding

While the first documented usage of adhesive dates at least 200,000 years back [130] [131], the first epoxy resin was synthesized in 1936 by Dr. Pierre Castan, Swiss chemist [132]. In aerospace, epoxy resin-based adhesives are now well established in various structural applications [133].

Process description

Prior bonding, adherend surfaces must be cleaned and modified. Then, an adhesive is applied on the treated adherend surfaces (paste adhesive) or between surfaces (film adhesive). Adherend surfaces are brought into intimate contact. The relative movement between adherends is constrained by fixtures while the pressure is applied on the outward facing adherend surfaces. The bond is then exposed to the specific temperature, pressure and humidity for the length of time to cure properly.

[7]Thermal spray terminology: tensile stresses = quenching stresses, compressive stresses = peening stresses

Bond formation

Adhesion theories can be distinguished according to the scale of action: macroscopic, microscopic, atomic and molecular [134]. The electrostatic theory takes place at the macroscopic scale, on the contrary, the mechanical interlocking acts at the microscopic scale. Three molecular theories were proposed: the diffusion, wetting and weak boundary layer. For the atomic scale, the chemical bonding was postulated.

Prerequisites Wetting is the liquid´s ability to form interface with solids. The contact angle between solid and liquid characterizes the degree of wetting. Adhesive must cover the substrate to ensure maximum adhesion so the wetting angle must be as small as possible. According the other definition, the surface tension of the adhesive should be same or lower than the surface tension of the adherend. This requirement for maximum adhesion applies to all possible combinations of adherends and adhesives.

In this thesis, three materials are bonded with epoxy adhesive: the stainless steel, aluminium alloy and CF/epoxy composite. Generally, metals possess higher surface energy than epoxy resins [135] [136]. The surface energy of CF/epoxy laminate and epoxy adhesive is equal. Consequently, the criteria for good wettability is satisfied for all retarder/substrate material combinations.

The diffusion theory requires (a) a high molecular mobility and (b) molecular compatibility of adherends. Obviously, the compatibility cannot be satisfied when bonding metal to metal and metal to composite with the epoxy adhesive. Diffusion plays role in the process of bonding thermoplastics using only heat or solvent (i. e. without adhesive) [137].

Main theories Chemical bonding theory supposes the formation of ionic, covalent or hydrogen bonds or van der Waals forces or acid-base complex between an oganic adhesive (epoxy) and adherend [138], [139]. Steel adherends may be bonded to epoxy groups by condesation reaction creating the oxides at the interface [140]. A correlation between the theoretical ion-pair force and the measured shear strength indicates that the ionic interaction significantly contributes to the strength of alu-

minium/epoxy joints exposed to water [139]. The van der Waals forces are believed to cause the adhesion according the adsorption theory [139]. According the acid-base theory, electron rich-elements (bases) reacts with electron poor elements (acids) and such attraction results in adhesion [134]. Aluminium oxide contain "acid sites" that reacts with "base sites" in the epoxy adhesives [141]. Comparing the typical strengths, the chemical bonds and interactions can be arranged from strongest to weakest: ionic bond, covalent bond, hydrogen bond, acid-base interaction, van der Waals forces [139].

Electrostatic theory assumes that an electron transfer occur between an adhesive and adherend. Such transfer cause the formation of two electronic bands (with electrical charge) at the adhesive/adherend interface. Electrostatic forces that evolve between those bands probably contribute to adhesion strength [142].

Mechanical interlocking theory argues that the level of filling the adherend's microscopic crevasses, pores and dimples vastly contributes to adhesion strength. The "level" can be characterized by the surface area per unit weigth of adherend [134]. Microrough surface can be obtained by surface treatments that modifies the adherend's surface morphology.

In this thesis, the FPL etching is utilized as a surface treatment of aluminium substrate prior bonding. Such process promotes the formation of Al_2O_3 towers and ridges on the aluminium surface [143] (Fig. 4.11a). Besides other chemical reactions that might occur between oxide layer and adhesive, the oxide morphology is believed to contribute to the adhesion strength through mechanical interlocking in aluminium and titanium bonded joints [144]. Deeper oxide layer might be formed through anodizing process[8]. In terms of joint strength and durability, anodized adherends perform better than FPL etched adherends [145].

For an optimal adhesion of CF/epoxy crack retarders, the peel ply is used. A microscopic morphology of peel ply fibers is transfered to the composite surface (Fig. 4.11c) during curing process and adhesion strength is thus increased [146]. Additionally, plasma treatment or surface abrasion might further increase the shear strength of bonded CF/epoxy joints [147].

[8]e.g. Chromic Acid Anodizing, Phosphoric Acid Anodzing

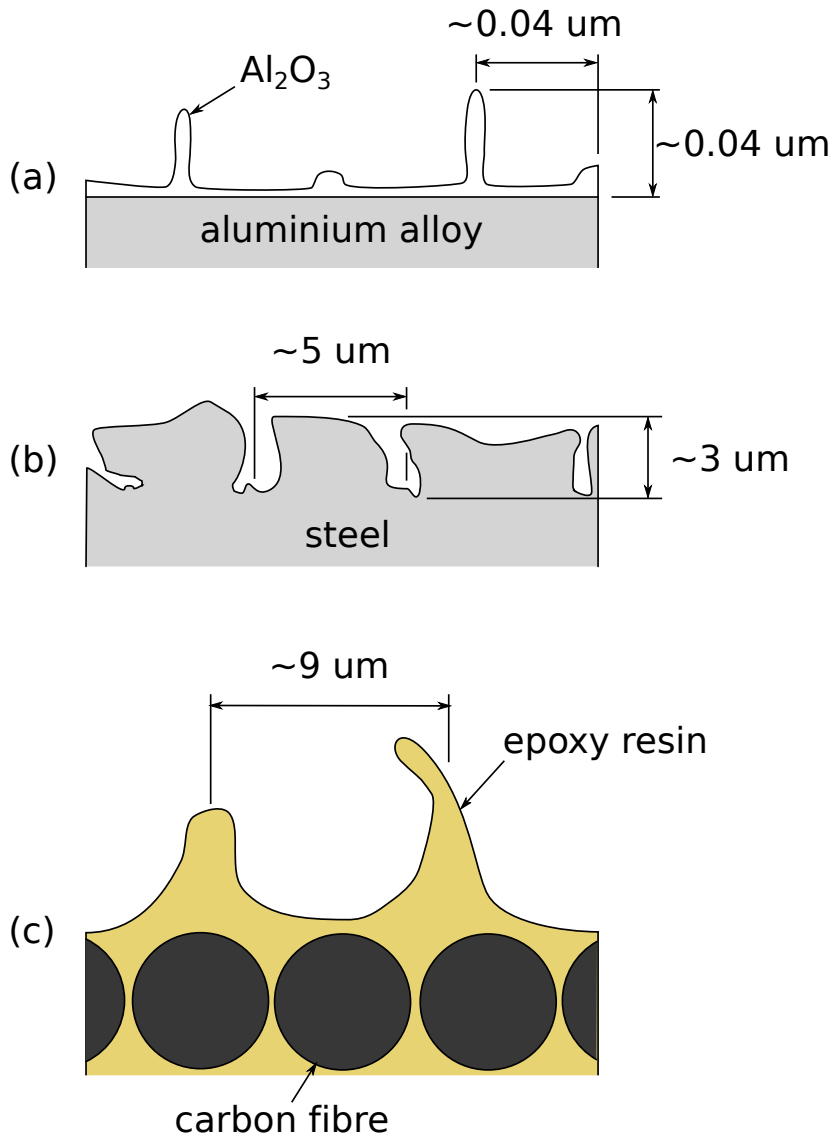

Figure 4.11: Surface morphology after the various surface treatments: (a) FPL etching. Adapted from [143], (b) Pickling. Adapted from [148]. (c) Peel ply. Adapted from [146].

Prior bonding, the stainless steel crack retarders were immersed in the pickling solution[9]. This solution attacks the chromium depleted layer under the oxide layer formed after cold-rolling. The oxide layer is subsequently removed by spalling [149]. The solution then attacks the grain boundaries [150] and create microrough surface [151] suitable for bonding (Fig. 4.11b). An alternative pickling solution[10] or the plasma treatment might further increase adhesion strength [152], [153]. Utilizing

[9] $HF + HNO_3$
[10] $CH_2O + H_2O_2 + HCl$

the anodization process in the nitric acid or sulfuric-chromic acid solution after pickling, the shear strength of stainless steel bonded joint increases [154].

Weak boundary layer theory states that the adhesive joint fails cohesively in the weak layer along the interface. In other words, the adhesion type of failure does not occur. The theory identifies the origins of weak layers and classifies them into seven groups: air, the adhesive, the adherend, air and the adhesive, air and the adherend, the adhesive and the adherend, the adhesive and the adherend and air [155].

Adhesive bonding process parameters can be divided into four groups:

- Mechanical surface treatment

  Duration

  Type of the abrasive[11] [12]

  Grit size[10]

  Particle diameter[11]

  Laser power[13]

  Scanning speed[12] [14]

  Stand off distance[12] [13]

  Radio frequency generator power[13]

  Gas composition[13]

  Gas flow rate[13]

- Chemical surface treatment

  Duration

  Bath or electrolyte composition

  Bath or electrolyte temperature

[11] Abrading
[12] Grid blasting
[13] Laser Surface Treatment
[14] Corona Discharge Treatment

The anodizing voltage-current density

Drying atmosphere temperature

- Curing

  Duration

  Pressure

  Temperature

  Heating rate

  Radiant flux[15]

- Post curing

  Duration

  Temperature

Bond characteristics

Mechanical properties Because the adhesive used in this thesis to bond the AISI 301 stainless steel and CF UD laminate to the 2024 substrate is cured well bellow annealing and glass transition temperatures (Section 5.2), the mechanical properties of adherends (crack retarder, substrate) remain unaffected. The bond between two Al alloy adherends typically exhibit the shear strength of $20 - 30$ MPa while the maximum lies between $40 - 50$ MPa [156].

Residual stresses Structural adhesives cure at elevated temperatures to obtain superior mechanical properties [157]. Curing temperature vary from 60 °C to 170 °C and thus the residual stresses evolve when adherends with dissimilar CTE are bonded. However, residual stresses might be lowered using an low-modulus adhesive [157].

In this thesis, all crack retarders are cured at 80 °C. Because of the CTE mismatch (substrate/retarder), some residual stresses were certainly induced. In the Chapter 2, the effect of residual stresses on the crack growth in substrate is discussed.

[15]Light curing

4.4.3 Ultrasonic Consolidation

Ultrasonic consolidation[16] is an additive technology developed by Dawn White and his colleagues in Ann Arbor, Michigan [158]. This technology combines ultrasonic welding and CNC machining together to manufacture a three-dimensional object out of thin metallic sheets. Deposit shows the excellent interfacial shear strength in combination with low thermal affection.

Process description

To build the first layer, thin metallic sheet is placed on the anvil (Fig. 4.12). The anvil might be heated to control the process temprature [159] and achieve better consolidation [160]. Then the textured sonotrode is positioned on the outward facing surface of metallic sheet. An increase in sonotrode's surface roughness lead to bonds with greater peel strengh [161]. Sonotrode oscillates in the direction of her rotational axis, rotates around that axis and pushes the foil against the anvil. While sonotrode rotates, the bond is continuously formed along the sonotrode's trajectory. When consolidation is finished, the deposit might be subjected to CNC machining. The whole process takes place at ambient air. Regarding the ultrasonic source, the electrical energy from power supply is converted to ultrasonic energy by transducer. Sonotrode, which is mechanically fixed to the transducer, amplifies the ultrasonic vibrations outputting from the transducer. Two transducer in push-pull configuration (Fig. 4.12) are used to increase energy input and consolidate relatively hard materials.

From process description, four main process parameters of ultrasonic consolidation can be distinguished: the amplitude of the ultrasonic vibrations, normal force of the sonotrode, longitudial speed of the sonotrode's and temperature of the anvil. The critical design parameters in the UC is the height to width ratio of the finished deposit and foil thickness. If the height to width ratio reaches 0.7-1.2, the bond is not created [162]. The maximum thickness of foils to be ultrasonically consolidated is $\sim$0.25 mm, otherwise the foil sticks to the sonotrode [163].

[16] Also known as Ultrasonic Additive Manufacturing (UAM).

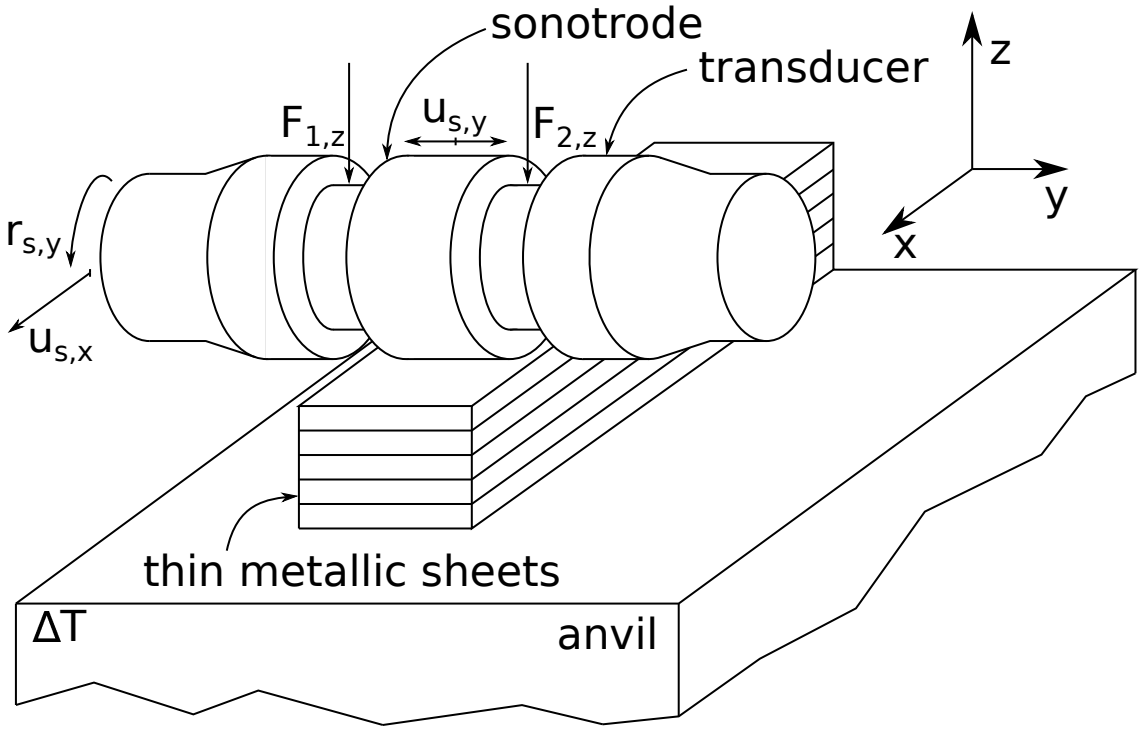

Figure 4.12: Ultrasonic consolidation apparatus.

Bond formation

First, the peaks of surface micro-asperities come into contact with adjacent surface of the other foil. The combination of normal force and oscillating motion brake up the oxide film at those peaks. Consequently, clean metal surfaces are brought into intimate contact and the micro-bonds are obtained. Bonded micro-asperities starts moving with ultrasonic vibration. Asperities soften[17], undergo the high-strain-rate deformation and collapse. The oxide film on the remaining unbonded surfaces is broke up by plastic flow and friction [165]. As a result, metallurgical bond between two metallic foils is obtained [166]. Although, the plastic deformation and friction generates heat, a temperature in the bond zone is well bellow melting temperature. A temperature rise of 100 °C was measured in the bond zone of 6061 alloy foils [167]. In the bond zone of Al/Ti interface, the temperature can vary from 170 °C (40 µm amplitude, 2 kN normal force) to 275 °C (60 µm amplitude, 2 kN normal force) [168].

[17]Ultrasonic softening [164]

Relatively soft materials (e.g. aluminium alloys) are covered with soft oxide film and thus bonding them together does not pose any difficulties [169]. Conversely, it is difficult to consolidate materials with hard oxide film (e.g. stainless steels, titanium alloys). Increasing the process parameters (normal force, amplitude) might help, however, it leads to various problems: foil bonds to the sonotrode, sonotrode‘s excessive wear [159], [163]. To solve this issue, interlayer made of aluminum might be used to create bond between two materials with hard oxide film [169], [170]. In this thesis, the aluminium foils are used as an interlayers between stainless steel foils. If the intermatallic compounds are formed in the bond zone of Al/Stainless steel joint, the Zn interlayer might be used to prevent it [171].

Deposit characteristics

Mechanical properties The 1100-O Al/cp-Ti joint exhibited the shear strength 46.3 MPa in as-build condition. Utilizing the Spark Plasma Sintering as a post-consolidation treatment, the shear strength more than doubled [59]. Obielodan et al. measured the shear strength 37.8 MPa on the 3003 Al/cp-Ti joint [172].

Residual stresses Despite the high-strain-rate deformation of asperities, friction between mating surfaces and heated anvil produce heat during the ultrasonic consolidation process; no attention has been payed to the evolution of thermal residual stresses after the consolidation. Particularly the consolidated structures made of the materials with dissimilar CTE migh experience the rise of residual stresses and subsequent warpage.

4.5 Mechanisms related to crack retarders

These mechanisms were previously identified as the most influential, although their significance strongly depends on e.g. loading conditions. Both stiffening and bridging can lower stress intensity factor at the crack tip and thus slow-down the fatigue crack propagation. Remaining mechanisms have negative impact on fatigue crack propagation.

Stiffening Before the fatigue crack reaches the crack retarder, the crack retarder acts as a stringer and transfers load from the substrate. The stiffer the crack retarder is, the more load is transferred. The load transfer from substrate to crack retarder may be desribed by the isostrain condition for composite material.

There is an assumption that an interfacial bond between layers is ideal and thus applied stress causes equal strain in all layers.

$$\epsilon_c = \epsilon_r = \epsilon_s \tag{4.14}$$

where ϵ_c is the total strain of assembly (substrate + retarder), ϵ_r is the strain of retarder and ϵ_s is the strain of substrate. According to the Hooke's law: $\sigma_c = E_c\epsilon_c$, $\sigma_r = E_r\epsilon_r$, $\sigma_s = E_s\epsilon_s$ and thus

$$\frac{\sigma_c}{E_c} = \frac{\sigma_r}{E_r} = \frac{\sigma_s}{E_s} \tag{4.15}$$

The relation between retarder stress and substrate stress is given by

$$\sigma_r = \frac{E_r}{E_s}\sigma_s \tag{4.16}$$

where E_r is the Young's modulus of retarder and E_r is the Young's modulus of substrate. If $E_r > E_s$, then

$$\frac{E_r}{E_s} > 1 \tag{4.17}$$

and thus

$$\sigma_r > \frac{E_r}{E_s}\sigma_s \tag{4.18}$$

Schijve [5] defined the stiffening ratio

$$\mu = \frac{\sum_{i=1}^{n} E_r^i A_r^i}{E_s A_s + \sum_{i=1}^{n} E_r^i A_r^i} \tag{4.19}$$

where A_r is the cross section of retarder, A_s is the cross section of substrate and n is the number of stiffening elements. He concluded that increasing the stiffness ratio increases the performance of crack retarder.

Bridging When the fatigue crack passes the bonded crack retarder, the crack retarder starts delaminating from the substrate. The delaminating crack retarder promotes restraining forces that limits the crack opening (Fig. 4.14) and reduces the ΔK (Fig. 4.13). Bridging mechanism is well observed in the FMLs [173], [174]. Modelling studies have shown that the stiffer the strap, the greater the bridging effect [3]. Precisely, the crack retarder's stiffness between delamination edges have the major impact on bridging. However, bridging effect is vastly limited by the yield limit of the crack retarder material [11].

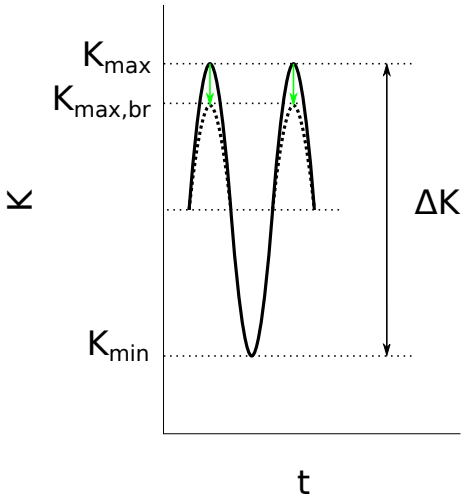

Figure 4.13: The reduction of K_{max} through bridging. Adapted from [173].

Delamination Crack retarder starts delaminating in front of the progressing crack tip [5], where the maximum tensile stresses are, and/or at the free ends, where the maximum shear stresses are (Fig. 4.14). The higher the crack retarder's stiffness is, the higher the adhesive shear stresses at the free ends are and the adhesive will fail earlier [3]. The straps can still carry the load but are less effective (Fig. 4.15) because of the lack of shear transfer capability [7]. The beneficial bridging effect is thus mitigated. It is well known that surface pretreatment and bondline thickness have the major impact on the adhesive shear strength [156], [175].

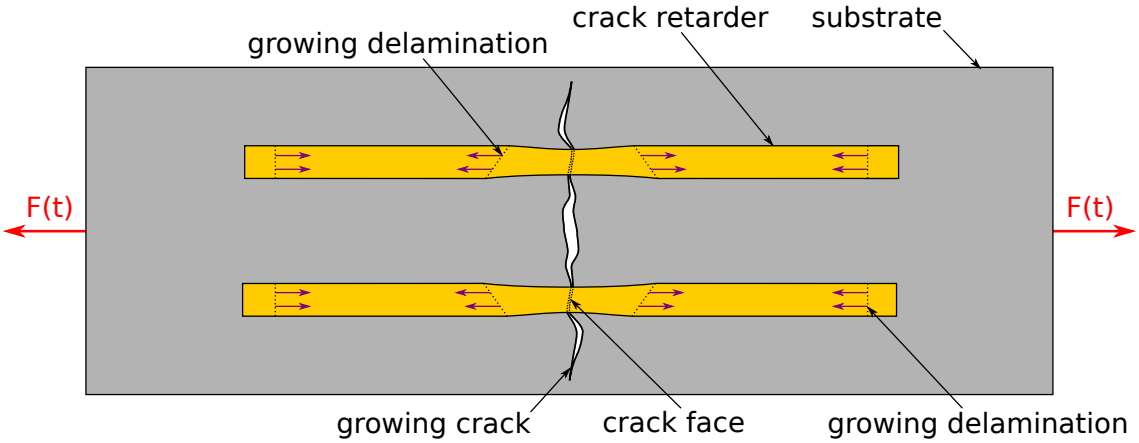

Figure 4.14: Bridging: notice the reduction in crack opening bellow the crack retarder and the transverse deformation of crack retarder. Delamination: typical shape and location. The violet arrows indicate the delamination's growth direction.

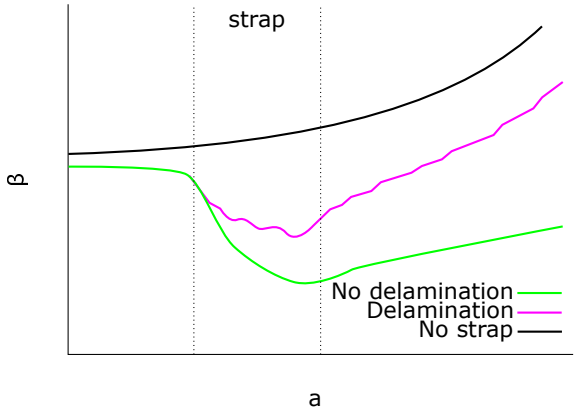

Figure 4.15: The reduction of the β through delamination. Adapted from [3].

According the modelling studies [11], [23], the Mode I and Mode II fracture toughness of the substrate/crack retarder interface are one of the most influential parameters of delamination resistance. The increase in G_{IIc} decreased the da/dN at low applied load ($\sigma_{max} \sim 30MPa$) and this decrease was more prominent if stiffer crack retarders were used [11]. Adhesive toughness tends to increase with bondline thickness [176].

In the specimens with laminated BCRs, the delamination can occur between crack retarder and substrate and/or within crack retarder. In the latter case, inter-ply delamination occurs [177]. This inter-ply delamination usually takes place in an unsymmetrical structures[18].

[18]Crack retarder attached only to one side of the substrate.

Secondary bending Due to the unsymmetrical configuration, the specimen's neutral line is shifted. As the unsymmetrical specimen is tension loaded, the bending moments emerge and cause out-of-plane deformation of the specimen (Fig. 4.16). The tensile stress at the crack tip is thus lowered or increased (unreinforced side) due to the presence of such moments [178]. Unequal stresses through thickness cause curved crack front and the different crack growth rates on the reinforced a unreinforced side of the specimen.

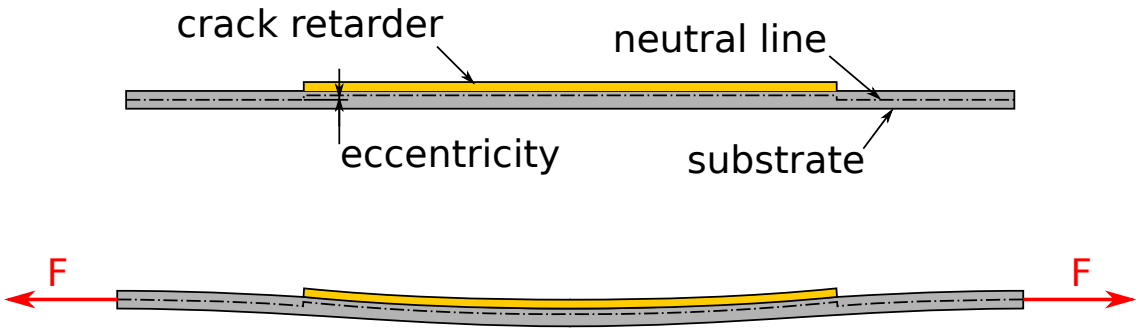

Figure 4.16: The effect of shifted neutral line and tensile loading on the specimen's deformation. Adapted from [178].

Thermal residual stresses Crack retarders are often exposed both to the temperature rise during adhesive curing process and to the temperature decrease during flight conditions. If coefficients of thermal expansion of substrate and crack retarder deviate, the change in ambient temperature promotes thermal residual stresses and out-of-plane deformation (Fig. 4.17). The level of residual stresses then depends on both crack retarder's and substrate's stiffness.

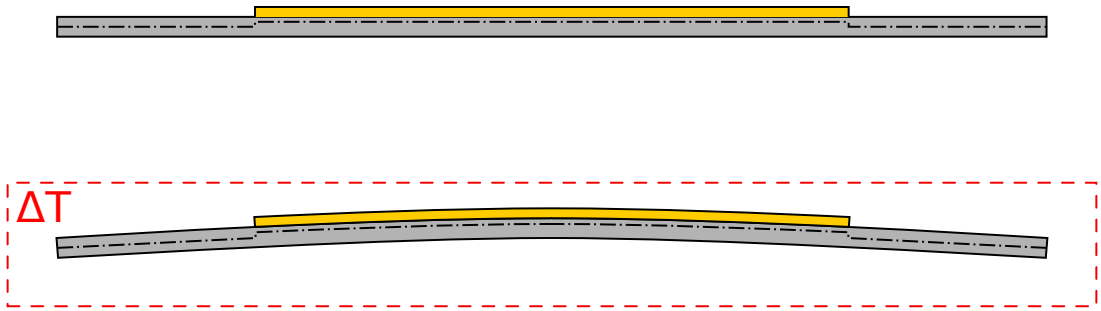

Figure 4.17: The effect of thermal expansion coefficient mismatch and thermal loading on the specimen's deformation. This deformation occurs when the CTE of crack retarder is higher than the CTE of substrate.

From 1D closed-form solution of thermal residual stresses [11], the effect of crack retarder's parameters on thermal residual stresses might be deduced. First, the equilibrium equation can be formulated:

$$\sigma_r t_r w_r + \sigma_s t_s w_s = 0 \tag{4.20}$$

where σ_r, σ_s are the stresses in the retarder (r) and substrate (s); t_r, t_s are the thicknesses of retarder and substrate; w_r, w_s are the widths of retarder and substrate. The width of retarder is equal to width of substrate (Fig. 4.18) and therefore:

$$\sigma_r t_r + \sigma_s t_s = 0 \tag{4.21}$$

Rewriting the equation 4.21, the stress in the retarder can be expressed:

$$\sigma_r = -\sigma_s \frac{t_r}{t_r} \tag{4.22}$$

Adding the thermal strain contribution into the equation 4.15, the compatibility equation can be reformulated:

$$\alpha_r \Delta T + \frac{\sigma_r}{E_r} = \alpha_s \Delta T + \frac{\sigma_s}{E_s} \tag{4.23}$$

where α_r, α_s are the coefficients of thermal expansion of retarder (r) and substrate (s); ΔT is the change in the ambient temperature (curing, service).
Rewriting the equation 4.23, the stress in the substrate can be expressed:

$$\Delta T E_s(\alpha_r - \alpha_s) + \frac{\sigma_r E_s}{E_r} = \sigma_s \tag{4.24}$$

Substituing equation 4.22 into equation 4.24 the residual stress in the substrate can be obtained:

$$\Delta T E_s(\alpha_r - \alpha_s) = \sigma_s + \frac{\sigma_s E_s t_s}{E_r t_r} \tag{4.25}$$

$$\Delta T E_s(\alpha_r - \alpha_s) = \sigma_s \frac{E_r t_r + E_s t_s}{E_r t_r} \tag{4.26}$$

$$\sigma_s = \frac{E_r t_r E_s \Delta T(\alpha_r - \alpha_s)}{E_r t_r + E_s t_s} \tag{4.27}$$

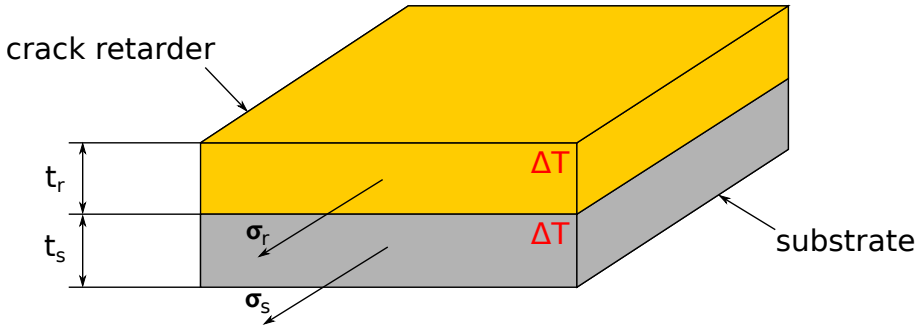

Figure 4.18: Cross section of two bonded plates subjected to a temperature load. Adapted from [11].

The effect of thermal residual stresses on the fatigue crack growth in a structures with crack retarders has been already discussed in the Chapter 2. Generally, the zones of compressive residual stresses lowers crack opening and reduces the ΔK (Fig. 4.19) [173].

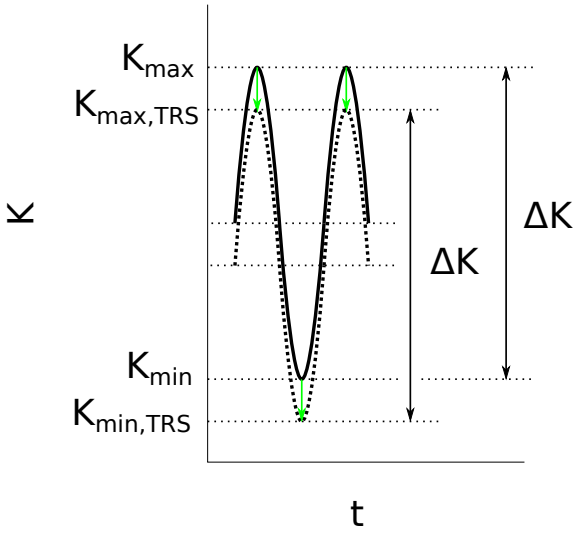

Figure 4.19: The reduction of the K_{max}, K_{min} through negative tensile residual stresses. Adapted from [173].

Other mechanisms Fatigue sensitive crack retarder can fail earlier and cause premature failure of structure [77] so the crack retarder material with higher fatigue properties should be preferred.

The connected dissimilar materials corrode in the presence of an electrolyte. The mating surfaces of bonded crack retarders and substrate are separated by an adhesive. However, the corrosion might still occur if electrolyte connects other surfaces of dissimilar metals.

The tendency to galvanic corrosion can be estimated comparing the electronegativity of combined metals. In this thesis, crack retarders made of various materials are attached to 2024 alloy substrate. Used crack retarder materials are arranged in descending order according the susceptibility to galvanic corrosion with 2024 alloy: CF/epoxy, Ti, 316L, 301 [179]. Substrate and crack retarder must be adequately sealed to be prevented against galvanic corrosion.

Chapter 5

Experimental Work

This chapter describes the experimental studies (Tab. 5.1) that have been done to meet the thesis objectives[1]. Each following section is named after the technology used in crack retarder fabrication. In the end, crack retarders are evaluated in terms of crack growth rate, fatigue life extension, weight and delamination resistance.

5.1 Substrate

The M(T) specimens were high-speed milled from the sheet made of 2024-T351 aluminium alloy, which is widely used in various aerospace applications. The fatigue crack growth tests were carried out on the M(T) specimen with several geometries (Fig. 5.1). The bare specimens were used as a substrate for bonded crack retarders made of AISI 301, CF UD and cold sprayed crack retarders made of AISI 316L and Ti-6Al-4V. The M(T) specimen width and length were chosen according to ASTM E647 [85] while the thickness of 2 mm represented common integral wing skin panel. The mechanical properties and chemical composition of substrate are shown in Tab. 5.2, 5.3. In case of the specimens with ultrasonically consolidated crack retarders, the substrate was manufactured in the reverse order (as elaborated in Chapter 5.4).

[1]Specimens with thinner crack retarder are marked with "1" (e.g. 1-AISI301), thicker crack retarder are marked with "2" (e.g. 2-AISI301)

Table 5.1: Test matrix.

	Crack retarder constituents						Crack retarder				Substrate		Loading parameters
Specimen name	No. of layers	Layer	Thickness (t_{lay} [mm])	No. of interlayers	Interlayer	Length [mm]	Width [mm]	Thickness (t_r [mm])	Manufacturing temperature [°C]	Material and geometry	Dimensions [mm]	Maximum stress (σ_{max} [MPa])	Cyclic loading
Bare	0	-	0	0	-	0	0	0	RT	2024-T351 M(T)	375 x 100 x 2	60	$R = 0.1$ $f = 15$ Hz RT
1-AISI301-BCR	1	AISI 301	0.26	1	Araldite® 2011	200	10	0.44	80			60	
2-AISI301A-BCR	2	AISI 301	0.26	2	Araldite® 2011	200	10	0.60	80			60	
2-AISI301B-BCR	2	AISI 301	0.26	2	Araldite® 2011	200	10	0.55	80			60	
1-CFUD-BCR	2	M10R/38%/UD150/CHS	0.16	1	Araldite® 2011	200	10.2	0.53	80			60	
2-CFUD-BCR	5	M10R/38%/UD150/CHS	0.16	1	Araldite® 2011	200	10.2	1.08	80			60	
1-AISI316L-CSCR	3	AISI 316L	0.20	0	-	200	11.1	0.48	?			60	
2-AISI316L-CSCR	6	AISI 316L	0.20	0	-	200	11.2	0.96	?			60	
1-Ti64-CSCR	3	Ti-6Al-4V	0.20	0	-	200	11.2	0.51	?			60	
2-Ti64-CSCR	6	Ti-6Al-4V	0.20	0	-	200	11.3	1.02	?			60	
Bare	0	-	0	0	-	0	0	0	RT			60	
1-AISI301-UCCR	1	AISI 301	0.26	1	1100-O	200	10.2	0.29	52			60	
Bare	0	-	0	0	-	0	0	0	RT			100	
2-AISI301-UCCR	2	AISI 301	0.26	2	1100-O	200	10.2	0.71	52			100	

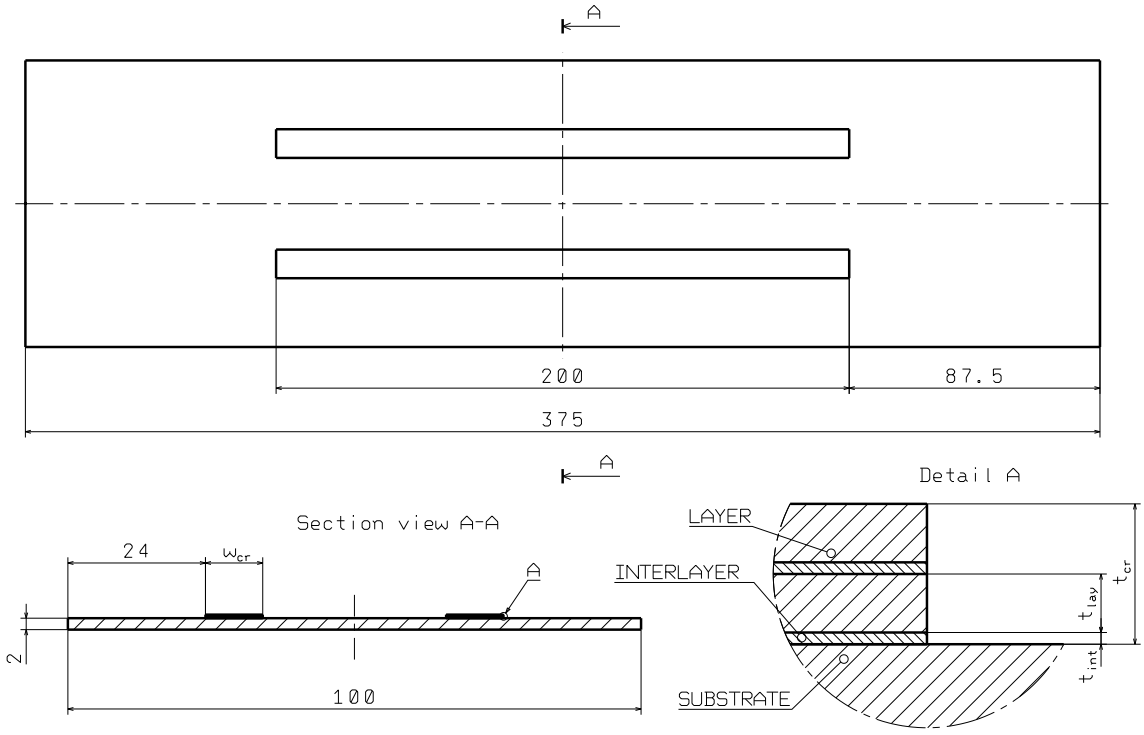

Figure 5.1: Specimen shape. Dimensions in mm, not in scale.

Table 5.2: 2024 chemical composition [180].

Alloy	Al	Cr	Cu	Fe	Mg	Mn	Si	Ti	Zn
2024	Bal.	<0.1	3.8 4.9	<0.5	1.2 1.8	0.3 0.9	<0.5	<0.15	<0.25

5.2 Bonded crack retarders

Substrate surface pretreatment: The FPL etching, commonly used surface preparation prior adhesive bonding in the aircraft industry, was performed on all M(T) specimens with bonded crack retarders. First, the surface was degreased with acetone and then FPL etched in the bath composed of 6.4% $Na_2Cr_2O_7 \cdot 2\,H_2O$, 23.4% H_2SO_4 and 70.2% H_2O (weight fraction). The etching duration was four hours at the ambient temperature. Finally, the surface was rinsed with water and blow-dried with the 45 °C air.

Table 5.3: Mechanical and thermal properties of substrate, bonded crack retarder and adhesive.

Material	2024-T351[a]	AISI 301	M10R/38% /UD150/CHS	Araldite® 2011
E [GPa]	72.4	185[b]	136[d]/143[e]	1.9[h]
ρ [g/cm^3]	2.77	7.88[c]	1.57[f]	1.05[h]
α [10^{-6}/K]	23	17[c]	1[g]	-
Rm [MPa]	470	1635[b]	2168[d]/2676[e]	-
$Rp_{0.2}$ [MPa]	325	1508[b]	-	-
A [%]	20	2.1[b]	-	-

[a] [180]
[b] [181]
[c] [182]
[d] Two layers. Tested according to ASTM D3039.
[e] Five layers. Tested according to ASTM D3039.
[f] [183]
[g] Typical generic values.
[h] [184]

5.2.1 Austenitic stainless steel

The capability of retarding the crack growth was examined for the specimen bonded with one steel layer and two steel layers. The AISI 301 austenitic stainless steel in the work-hardened state was chosen for its high strength, elastic modulus and CTE (see Tab. 5.3, 5.4 for mechanical properties and chemical composition).

Strap surface pretreatment: The straps used for adhesive bonding of crack retarders were cut out of the sheet made of 0.255 mm thick AISI 301 steel and degreased with acetone. After that, the straps were immersed in the solution containing 12.5% HF, 40.8% H_2O, and 46.7% HNO_3 for 20 minutes at the ambient temperature. In the end, rinsing with water and blow-drying with the 45 °C air took place.

Adhesive bonding: The crack retarders were bonded onto the specimen surface by the two-component Araldite® 2011 structural adhesive. The specimen with one steel layer (1-AISI301-BCR) was cured for 24 hours at the ambient temperature and for 30 minutes at the 80 °C. In case of the specimen with two steel layers (2-AISI301-BCR), first, two pretreated straps were bonded together and cured. An

excessive adhesive layer on the outer surfaces was removed. Then, the resulting BCRs were degreased with acetone and immersed in the solution containing H_2O, HF and HNO_3 for 20 minutes at the ambient temperature. Finally, bonding onto the substrate and curing were done. The same curing process was used as in the case of the 1-AISI301-BCR. Note that two specimens with two steel layers were manufactured; specimen 2-AISI301A-BCR and 2-AISI301B-BCR (Tab. 5.1).

Table 5.4: AISI 301 chemical composition [182].

Alloy	Fe	C	Mn	Si	P	S	Cr	Ni
301	Bal.	<0.15	<2	<1	<0.045	<0.03	16 18	6 8

5.2.2 Unidirectional carbon fibre

To compare the performance of steel crack retarders with previously validated crack retarder material, the BCRs made of two and five layers of M10R/38%/UD150/CHS prepreg were prepared. The prepreg consists of the high-strength unidirectional 12K carbon fibre fabric and M10R epoxy resin matrix (see mechanical properties in Tab. 5.3).

Strap manufacturing process: First, the prepreg roll was de-frozen at the ambient temperature to avoid the condensation of air humidity. Then, the individual prepreg plies were cut out of the prepreg roll. After removing the release film from the prepreg plies, the hand lay-up set off. As the desired number of prepreg plies was positioned in a single direction, the entire assembly was covered with the peel ply, bleeder cloth and vacuum bagging film. Such assembly was autoclaved at 0.5 MPa and 120 °C for 1 hour. Finally, the cured sheets were cut with a hand saw to obtain 10 mm wide crack retarders.

Crack retarder surface pretreatment: Using the peel ply, the crack retarder surfaces were modified to optimize the bond quality. Prior to bonding, they were degreased with acetone.

Adhesive bonding: The crack retarders were bonded onto the specimen surface by the Araldite® 2011 adhesive. Both specimens were then cured for 24 hours at the ambient temperature and post-cured for 30 minutes at the 80 °C.

5.3 Cold sprayed crack retarders

To compare the bonded crack retarders with the additively manufactured ones, four specimens with cold sprayed crack retarders made of Ti-6Al-4V titanium alpha-beta alloy and AISI 316L austenitic stainless steel were manufactured (see Tab. 5.5 and 5.6 for powder properties). Crack retarders were deposited using the Impact Spray System 5/11 and following process parameters: stand-off distance 30 mm, step distance 1 mm, gun travel speed 0.5 $m \cdot s^{-1}$, gas (N_2) pressure 50 bar and temperature 1100 °C. These process parameters were chosen according the previous research done by Impact Innovations. To prevent overspray and obtain consistent width and length of crack retarders, the metallic protective mask was utilized prior spraying.

Cold sprayed deposits in as-sprayed condition often possess lower mechanical properties (Fig. 5.7) than wrought counterparts. To increase the load transfer capability, it was decided to increase the height of cold sprayed crack retarders to 0.5 mm and 1.0 mm for both material combinations. After the deposition, the crack retarders were slightly higher and thus their upper surface was milled.

Table 5.5: SANDVIK 316L (15-38 µm) powder chemical composition [185].

Alloy	Fe	C	Cr	Ni	Mo	Si	Mn	S	P
316L	Bal.	0.03	16.0 18.0	10.0 14.0	2.0 3.0	1.0	2.0	0.03	0.045

Table 5.6: AP&C Ti-6Al-4V (15-45 µm) powder chemical composition [186].

Alloy	Ti	Al	V	Fe	O	C	N	H	Y
Ti-6Al-4V	Bal.	5.50 6.75	3.50 4.50	0.05 0.25	0.14 0.16	0.02	0.02	0.010	<0.005

Table 5.7: Mechanical and thermal properties of cold sprayed crack retarder.

Material	Ti-6Al-4V	AISI 316L
E [GPa]	69.7[a]	182[a]
ρ [g/cm^3]	4.43[b]	8.00[c]
α [10^{-6}/K]	8.6[b]	15.9[c]
Rm [MPa]	295 [a]	795[a]
$Rp_{0.2}$ [MPa]	-	765[a]
A [%]	-	0.05[a]

[a] Tested according to ASTM E8.
[b] [180]
[c] [182]

5.4 Consolidated crack retarders

Two 2024-T351 M(T) specimens with ultrasonically consolidated crack retarders were manufactured. Crack retarders were made of AISI 301 steel; the same composition, thickness and batch as in case of BCRs (Tab. 5.4). Additionally, the 0.05 mm thick interlayer made of 1100 alloy was used between steel layers (Tab. 5.8, Fig. 5.9). The substrate surface had to be machined prior consolidation to be perfectly leveled and clean, for this reason, it was not possible to use the same 2024-T351 bare M(T) specimens as in previous experiments. The crack retarders were first consolidated to the 6 mm thick 2024-T351 sheet and then the M(T) specimen was extracted from the sheet. One 2024-T351 bare M(T) specimen was extracted for the comparison purposes and to avoid batch-to-batch inconsistency (Section 4.3).

Table 5.8: 1100 alloy chemical composition [187].

Alloy	Al	Si+Fe	Cu	Mn	Zn
1100	Bal.	0.95	0.05 0.20	0.05	0.10

5.4.1 Austenitic stainless steel

At time of performing experimental studies, consolidating the AISI 301 steel foils of thicknesses 0.255 mm was on the edge of what was possible. Thus the optimal

Table 5.9: Mechanical and thermal properties of 1100-O interlayer used in consolidated crack retarder.

Material	1100-O
E [GPa]	69.0[a]
ρ [g/cm^3]	2.71[a]
α [10^{-6}/K]	23.6[a]
Rm [MPa]	90[a]
$Rp_{0.2}$ [MPa]	35[a]
A [%]	40[a]

[a] [188]

process parameters had to be determined. For this reason, several trials with varying: sonotrode's frequency, longitudinal speed, amplitude, driver[2], interlayer thickness were performed by Fabrisonic. The relative strength of the bond between materials was determined using comparative manual peeling test.

The 30 kHz trials were conducted on the Fabrisonic SL 1200, Ultrasonic Additive Manufacturing machine with 2 kW ultrasonic welding system. Across seven trials, the sonotrode's amplitude and interlayer thickness was increasing while the longitudial speed was decreasing. The pressure in the machine's piston assembly was kept contant at 0.827 MPa; this roughly corresponds to the 3000 N of down force. No bonding to steel was achieved in the Trial 1 (Fig. 5.2a). Based on the results, a good bonding to steel was achieved in the Trial 6, it was moderately hard to peel up steel from anvil (Fig. 5.2b). Some bonding to steel was achieved in the Trial 7, it was difficult to peel up steel from anvil (Fig. 5.2c). Because the results of Trial 6 and 7 were found contradictory, other trials were done.

[2]Driver is placed between sonotrode and foil to be consolidated. Driver holds foil in place, transfers horn's oscillations and prevents foil from bonding to the horn.

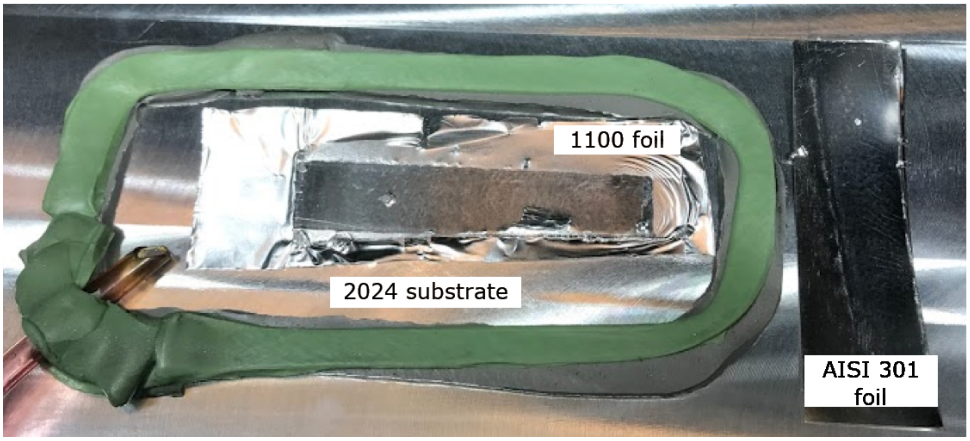

(a) Trial 1: 32 µm amplitude, 25.4 mm/s longitudinal speed, titanium driver, 25 µm thick 1100-O interlayer, unheated anvil, 3000 N down force.

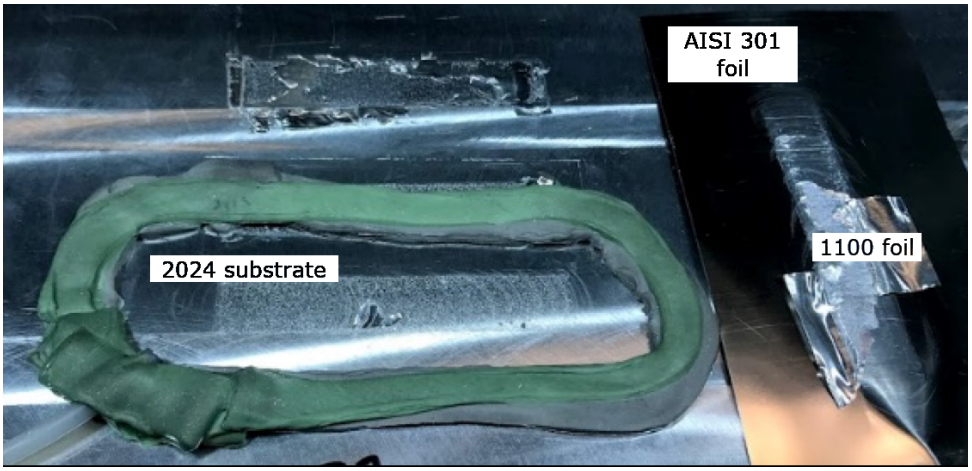

(b) Trial 6: 35.7 µm amplitude, 21.2 mm/s longitudinal speed, no driver, 51 µm thick 1100-O interlayer, unheated anvil, 3000 N down force.

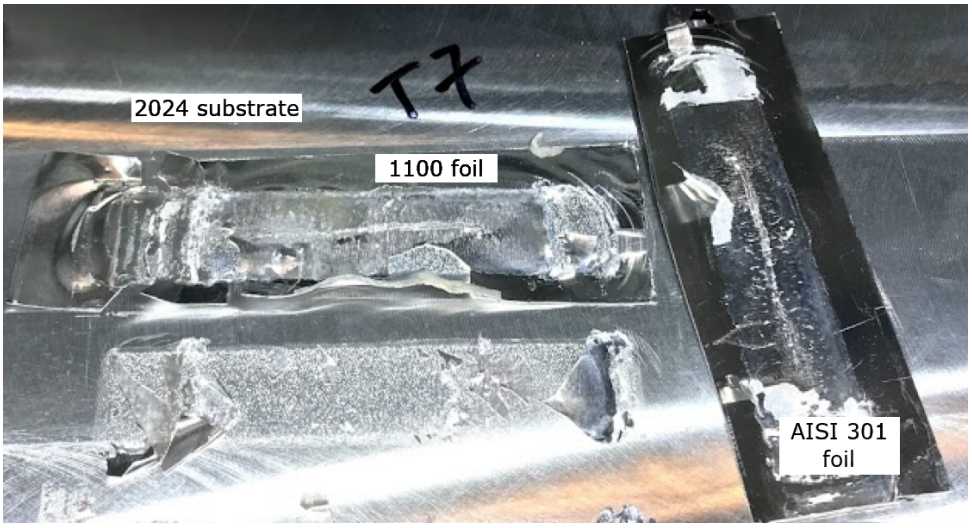

(c) Trial 7: 35.7 µm amplitude, 6.4 mm/s longitudinal speed, titanium driver, 51 µm thick 1100-O interlayer, unheated anvil, 3000 N down force.

Figure 5.2: 20 kHz trials.

Two 20 kHz trials were conducted on the Fabrisonic SL 7200, Ultrasonic Additive Manufacturing machine with 9 kW ultrasonic welding system. During these trials, the down force and longitudinal speed were kept constant while the sonotrode's amplitude was increasing. According the results, it was very difficult to peel up steel from anvil in both trials. In the Trial 8, a good bonding to steel was achieved (Fig. 5.3a). However, a few delaminations appeared in the Trial 9 (Fig. 5.3b).

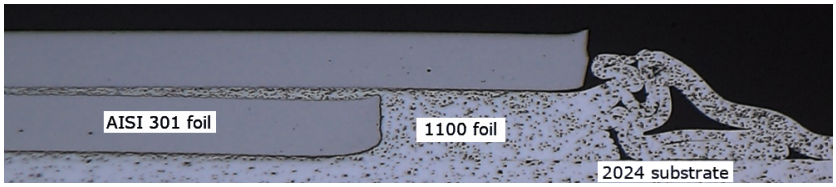

(a) Trial 8: 40 µm amplitude, 21.2 mm/s longitudinal speed, titanium driver, 51 µm thick 1100-O interlayer, anvil heated at 52 °C, 7500 N down force.

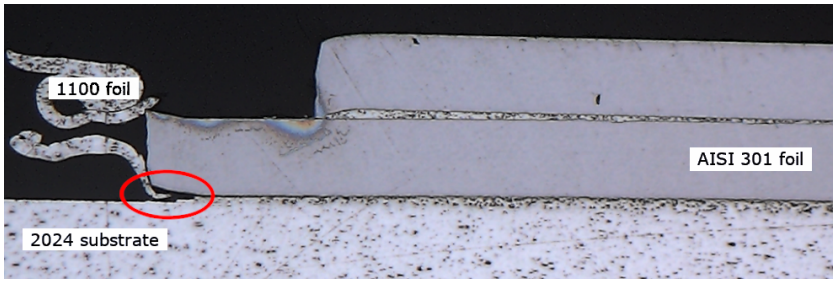

(b) Trial 9: 41.43 µm amplitude, 21.2 mm/s longitudinal speed, titanium driver, 51 µm thick 1100-O interlayer, anvil heated at 52 °C, 7500 N down force. Red circle marks delamination.

Figure 5.3: 30 kHz trials.

5.5 Fatigue crack growth test

Prior testing, the 5 mm long notch was machined to the specimen with bonded (CF UD, AISI 301), cold sprayed crack retarders (Ti-6Al-4V, AISI 316L) and without crack retarder (Bare). The 10.6 mm long notch was machined to all specimens with ultrasonically consolidated crack retarders because the precracking was unsuccessful after the 1.0×10^6 - 1.4×10^6 cycles. All specimens with bonded crack retarders, cold sprayed crack retarders, without crack retarder and the specimen with ultrasonically consolidated crack retarders (1-AIS301-UCCR specimen) were subjected to the crack propagation test with the following parameters: $\sigma_{max} = 60$ MPa, R =

0.1 and f = 15 Hz. Even with the larger machined notch (i.e. 10.6 mm in length), the precracing in the 2-AIS301-UCCR specimen was unsuccessful at the σ_{max} = 60 MPa and σ_{max} = 80 MPa. The crack did not start growing after the 1.0×10^6 - 1.4×10^6 cycles. For this reason, the test was conducted at σ_{max} = 100 MPa. At this stress level, the fatigue crack started to grow. In all cases, the crack length was periodically measured by the travelling microscope on the specimen's unreinforced side. The cyclic load was applied until the final failure of specimen.

5.6 Delamination monitoring

Delamination monitoring was done by measuring the specimen's thermal response using the Flir SC660 after the optical excitation through 2x 400 W halogen lamps (Fig. 5.4). Thermal response[3] was collected during heating and decay while the excitation took 5, 7 and 10 seconds. It appeared from the first processed thermal sequences that the highest contrast was acquired after 10 second excitation, so analysis was performed only for this excitation time. To minimize the negative effect of reflective heat, specimens were painted with white spray-paint ThermaSpray 500 with defined emissivity.

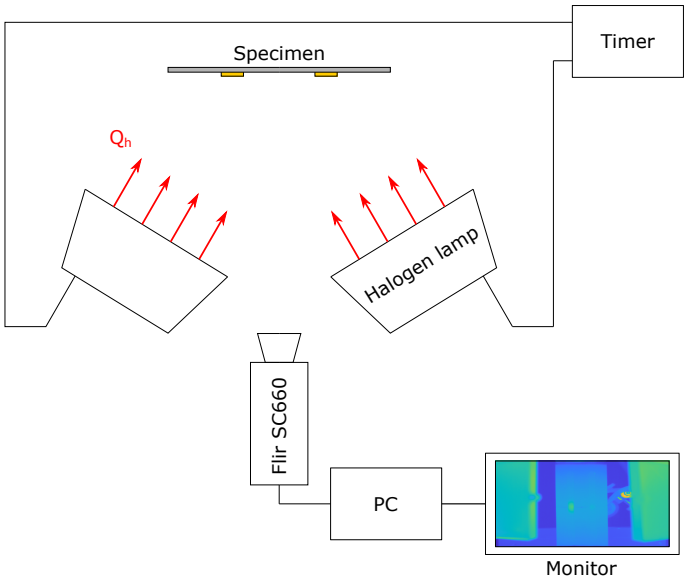

Figure 5.4: Pulsed thermography apparatus.

[3]Sequence of thermal images.

5.7 Digital image processing

Thermal sequence was first normalized to reduce the effect of non-uniform heating and optical properties variability across the measured surface. Then, normalized thermal sequence was fitted with 2nd–4th order polynomials (i.e. Thermographic Signal Reconstruction) to reduce high spatial frequency noise [189]. Solving the 1st derivative of each polynomial, the flaw to background contrast was increased [189].

The decay sequence was first extracted (Fig. 5.5a) from the thermal response and then normalized by dividing the decay thermal images by the image at the beginning of the decay

$$\mathbf{W} = \frac{\mathbf{T}}{T_{x,y,t_0}} \tag{5.1}$$

where $\mathbf{T} = (T_{x,y,t})$ represents the history of x, y dimensionless temperature field over the decay time t, T_{x,y,t_0} is the first x, y dimensionless temperature field at the beginning of the decay and $\mathbf{W} = (w_{x,y,t})$ is the normalized history of x, y dimensionless temperature field over the decay time t (Fig. 5.5b). The dimensionless temperature history of each pixel in the field was fitted by 2nd-4th degree logarithmic polynomial (Fig. 5.5c):

$$\log_{10}(w_{x,y,t}) = a_0 + a_1[\log_{10}(t)] + a_2[\log_{10}(t)]^2 + ... + a_4[\log_{10}(t)]^4 \tag{5.2}$$

where $w_{x,y,t}$ is the pixel's dimensionless temperature history over the time t and $a_0 - a_4$ are the polynomial coefficients. Then the 1st derivative of each polynomial was solved:

$$\mathbf{B} = \frac{\mathrm{d}}{\mathrm{d}\log_{10}(t)} \log_{10}(w_{x,y,t}) \tag{5.3}$$

From the first derivatives, the dimensionless temperature history of each pixel is reconstructed. To find the dimensionless temperature field with greatest contrast between sound and defective region, four pixels representing the defective region and four pixels representing sound region were picked directly from the field. Then, the x, y temperature field with maximal difference between defective and sound region $b_{x,y,t_{mc}}$ was found. If:

$$max\{w_{sound} - w_{def}\} \rightarrow t = t_{mc} \tag{5.4}$$

where w_{sound} is the average dimensionless temperature in the sound region and w_{def} is the average dimensionless temperature in the defective region. The $b_{x,y,t_{mc}}$ matrix was plotted (Fig. 5.5d), crack retarder region was selected and binary matrix representing this region was created:

$$\mathbf{C} = (c_{x,y}), \qquad c_{xy} \in \{0, 1\} \tag{5.5}$$

where "0" represents region outside the selection and "1" represent region inside the selection. Number of pixels representing each crack retarder p_{CR} was calculated summing the non-zero matrix entries:

$$p_{CR} = \sum_{x=1}^{n} \sum_{y=1}^{n} c_{x,y} \tag{5.6}$$

Then the dimensionless normalized temperature field was entry-wise multiplied by unit matrix to extract x, y temperature field of each bonded crack retarder:

$$\mathbf{R} = \mathbf{Q} \circ \mathbf{C} \tag{5.7}$$

Dimensionless normalized temperature field of crack retarder $\mathbf{R}$ was plotted and the lowest dimensionless temperature in the sound region (local minimum) $r_{sound,loc,min}$ was selected. Comparing the matrix entries with the local minimum, a new matrix with dimensionless temperature entries in defective region was created:

$$\mathbf{D} = (d_{xy}), \qquad d_{xy} < (r)_{sound,loc,min} \tag{5.8}$$

where d_{xy} are dimensionless temperatures in the defective region. Then the binary matrix $\mathbf{M}$ representing defective area in each crack retarder was created:

$$\mathbf{M} = (m_{xy}), \qquad m_{xy} \in \{0, 1\} \tag{5.9}$$

where "1" entries represents defective region and "0" represents sound region. Pixels representing the defect p_{def} were counted by summing the binary matrix entries:

$$p_{def} = \sum_{x=1}^{n} \sum_{y=1}^{n} m_{xy} \tag{5.10}$$

The percentage of delaminated area A_{del} was finally given by:

$$A_{del} = \frac{p_{def}}{p_{CR}} 100 \tag{5.11}$$

(a) Raw.

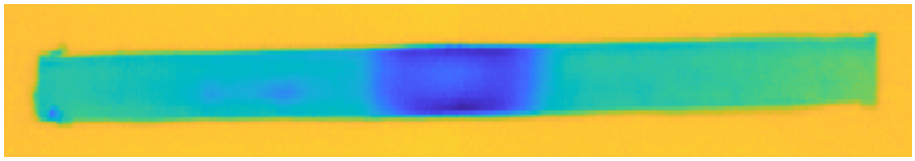

(b) Normalized.

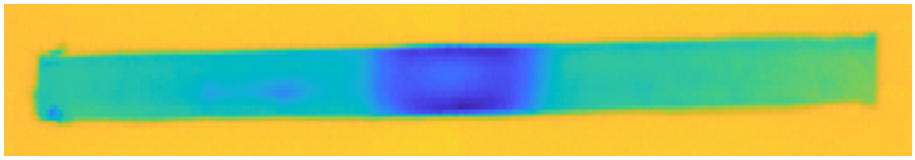

(c) TSR: 4th order polynomials.

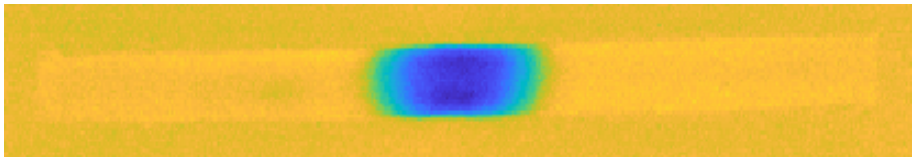

(d) TSR: first derivatives of polynomials.

Figure 5.5: Thermographic image processing steps: chronological order.

5.8 Results and discussion

During the crack propagation test, no crack initiation was observed in the BCRs. They broke[4] or disbond[5] shortly after the substrate failure. In cases of all cold sprayed crack retarders, the crack propagated directly from the substrate to the crack retarders (Fig. 5.6). In case of the ultrasonically consolidated crack retarders,

[4] 1-AISI301A-BCR, 1-CFUD-CR

[5] 2-AISI301A-BCR, 2-AISI301B-BCR, 2-CFUD-BCR

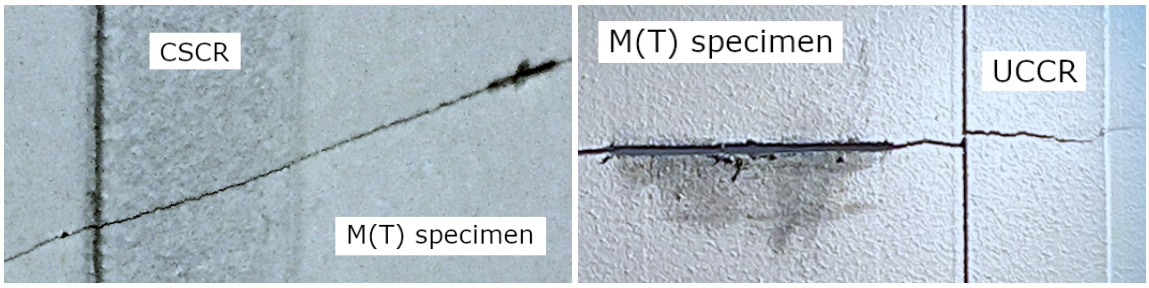

(a) 1-316L-CSCR specimen. (b) 1-AIS301-UCCR specimen.

Figure 5.6: Direct propagation of fatigue crack to crack retarder.

the failure was contradictory. The fatigue crack in the specimen with one steel layer (1-AISI301-UCCR) directly propagated to the crack retarder (Fig. 5.6a). However, the crack in the specimen with two steel layers (2-AISI301-UCCR) remained in the substrate and the crack retarders broke immediately after the substrate failure. Measured crack lengths were averaged for each specimen side and plotted against the number of cycles, thus the crack propagation curves were obtained (Fig. 5.7, 5.8).

With regard to specimens possessing crack growth life longer than specimen without crack retarder (Bare), no significant delay can be observed in the crack retarder area, (16–26) mm. The positive crack retarding effect manifests along the entire crack path. Similarly, any significant change in the crack growth rate can be observed in specimens possessing shorter fatigue life.

The fatigue life extension can be expressed by the life extension parameter:

$$LEF = \frac{N_i - N_{bare}}{N_{bare}} \tag{5.12}$$

where N_i is the number of cycles of specimen with crack retarders and N_{bare} is the number of cycles of specimen without crack retarders. All bonded crack retarders resulted in a significant fatigue life extension. The greatest increase, (1.9-2.0), was observed in case of specimen with two steel layers (Fig. 5.9). One can observe a relatively small difference between the fatigue crack growth curves of specimen with two and five CF UD layers. This was probably caused by the evolution of thermal residual stresses during the curing process, which raised the mean stress high enough, to speed-up the crack propagation in the specimen with thicker CF

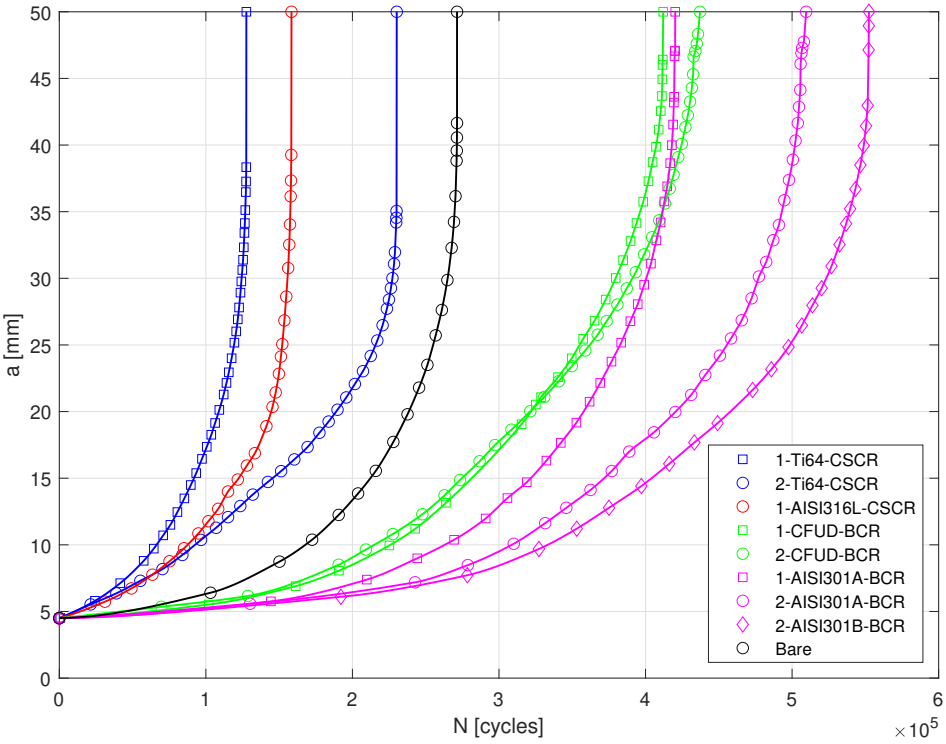

Figure 5.7: Crack growth curves: bonded and cold sprayed crack retarders; $\sigma_{max} = 60$ MPa, $R = 0.1$, $f = 15$ Hz.

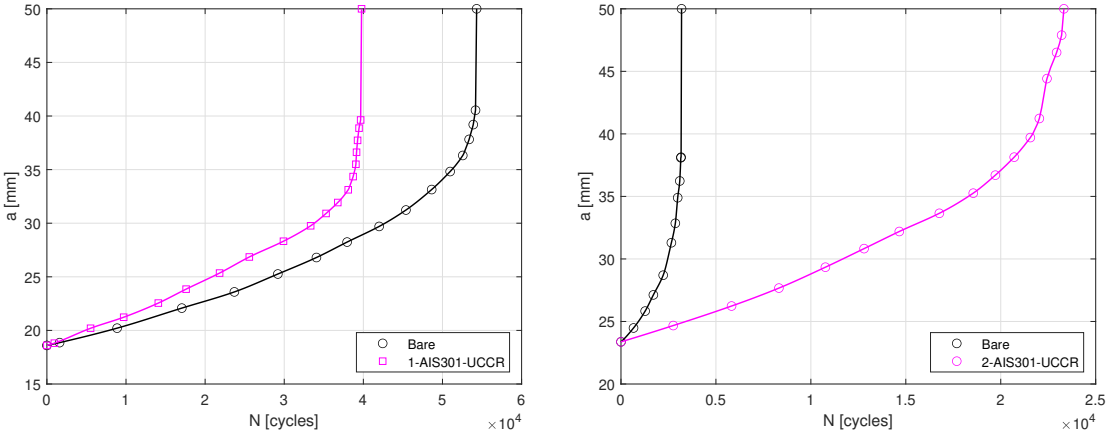

(a) 1-AISI301-UCCR specimen.

(b) 2-AISI301-UCCR specimen.

Figure 5.8: Crack growth curve: ultrasonically consolidated crack retarders; $R = 0.1$, $f = 15$ Hz.

UD crack retarders. Regarding this observation, using more than two CF UD layers appears to be redundant. All cold sprayed crack retarders dramatically decreased the fatigue life. The greatest decrease, 50%, was observed in the fatigue life of specimen with the Ti-6Al-4V crack retarders. The specimen with the thicker 316L crack retarder failed within the crack initiation period due to the presence of rapidly growing crack at one of the ends of the crack retarder.

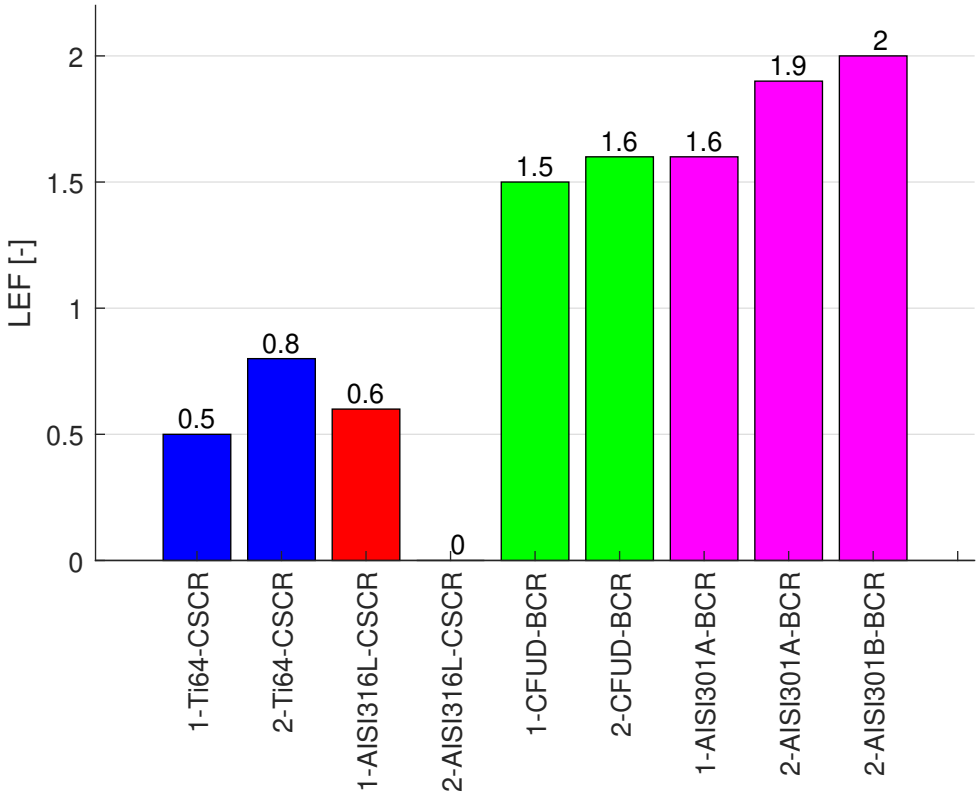

Figure 5.9: Life extension parameter: bonded and cold sprayed crack retarders.

Regarding the poor fatigue properties (i.e. decreased fatigue life and increased crack growth rate) of specimens with CSCRs, there are several explanations. The substrate temperature increased due to its plastic deformation during cold spraying and due to the heat transfer from the impinging jet. A combination of cooldown from such temperature and the crack retarder's CTE dissmilar from the substrate probably led to the evolution of tensile residual stresses in the substrate. The similar out-of-plane deformation (Fig. 4.17) was observed in all specimens with CSCRs. The temperature increase in the substrate certainly altered its mechanical properties.

A noticeable drop in the substrate hardness was measured in all specimens with CSCRs. Additionally, the crack retarder failed prematurely due to the poor fatigue properties of as-sprayed crack retarders. The poor fatigue properties of cold sprayed deposits were also observed by Čížek et al. [190]. In their study, the pure metalic specimens (Ti, Ni, Al, Cu) possessed greater fatigue crack growth rates than cold-rolled counterparts.

Specimen with one ultrasonically consolidated steel layer (1-AISI301-UCCR) failed earlier, thus his fatigue life was 30% lower compared to the specimen without crack retarder (Bare) (Fig. 5.10a). However, specimen with two steel layers (2-AISI301-UCCR) experienced the greatest increase by a factor of 7.3 (Fig. 5.10b). Note that in this specimen, the precrack length was five times greater and the σ_{max} was 1.66 times greater compared to the specimens with bonded and cold sprayed crack retarders.

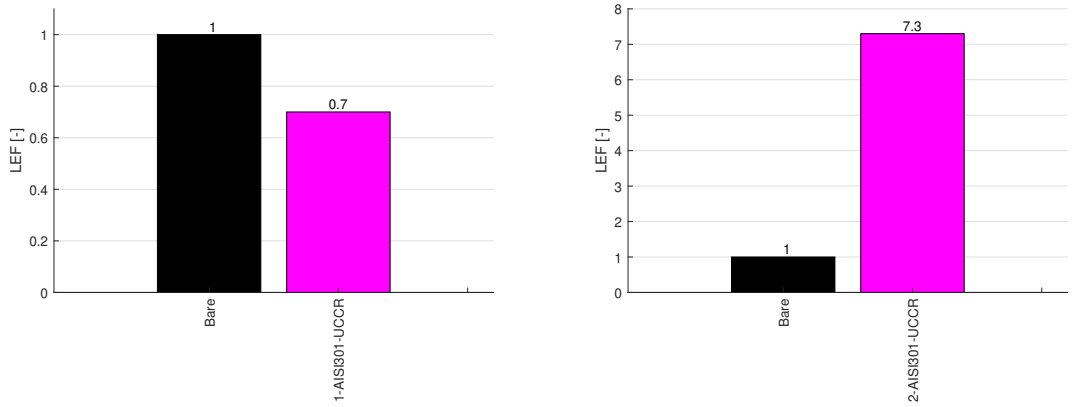

(a) 1-AISI301-UCCR specimen. (b) 2-AISI301-UCCR specimen.

Figure 5.10: Life extension parameter.

To obtain crack growth rates, the fatigue crack growth data were interpolated using the Modified Akima piecewise cubic Hermite interpolation spline (makima Matlab function). Since the beginning of the test, the specimens with CF UD and steel bonded crack retarders maintained the crack growth rate below the growth rate of bare specimen (Fig. 5.11). Unfortunately, the specimens with cold sprayed crack retarders possessed a higher rate in the whole crack length range, which resulted in already mentioned shorter fatigue life. Although the crack retardation in the 2-Ti64-CSCR specimen can be identified in the (11–28) mm crack length range, the

specimen failed earlier than the bare one because the crack grew significantly faster in other regions.

The fatigue crack growth rate in specimen with one steel layer (1-AISI301-UCCR) was higher in the whole crack length range (Fig. 5.12a), which resulted in already mentioned shorter fatigue life. On contrary, the specimen with two steel layers possessed fatigue crack growth rate significantly lower compared to the specimen without crack retarders (Fig. 5.12b).

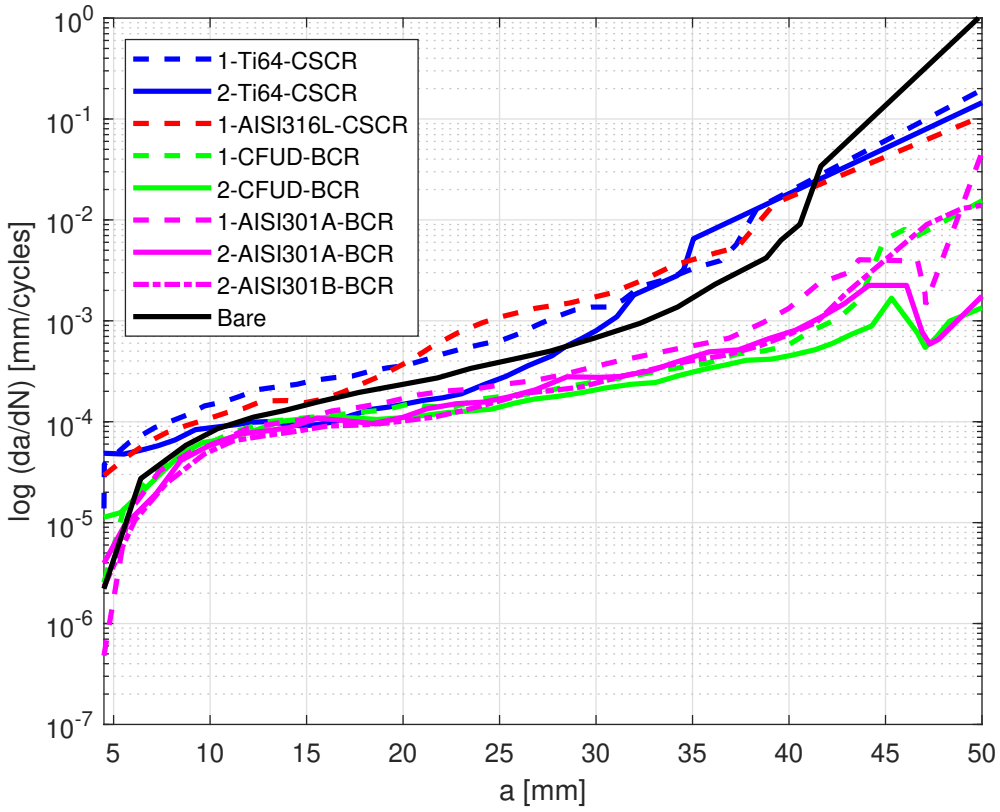

Figure 5.11: Fatigue crack growth rate: bonded and cold sprayed crack retarders.

The percentage of life improvement with respect to the bare specimen per gram weight of crack retarder can be expressed by a subsequent parameter [3]:

$$e = \frac{\frac{N_i - N_{bare}}{N_{bare}} 100}{m_{strap}} \tag{5.13}$$

where m_{strap} is the crack retarder weight. It is obvious that the BCR made of two CF UD layers can significantly extend fatigue life while maintaining relatively low

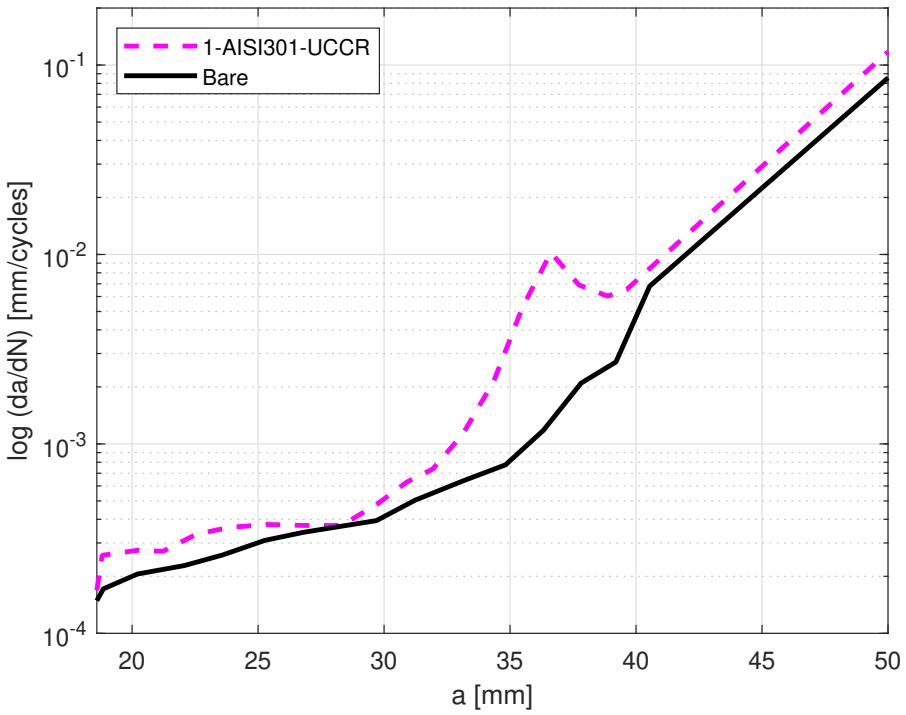

(a) 1-AISI301-UCCR specimen.

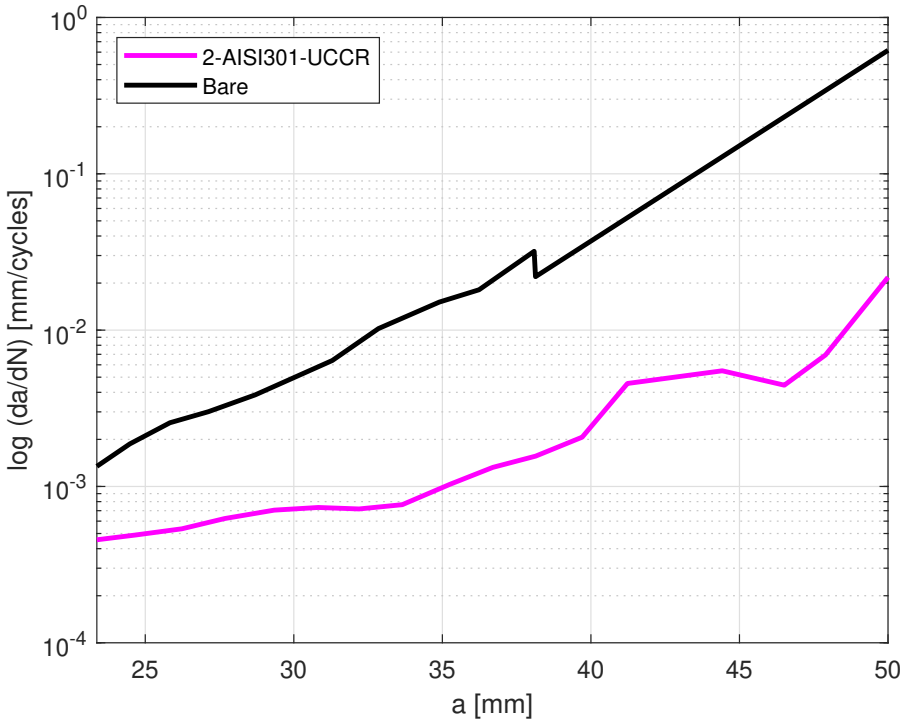

(b) 2-AISI301-UCCR specimen.

Figure 5.12: Fatigue crack growth rate: ultrasonically consolidated crack retarders

weight of a specimen (Fig. 5.13). One can also observe that the thinner BCR were much more effective than the thicker ones, however, this fact was already proved by Boscolo [3] and Molinari [21]. Specimens with steel BCRs did not perform in the same way. In comparison with carbon fibre crack retarders, their total thickness was lower. They probably did not experience the secondary bending to the extent that would have led to the lower performance. The greatest life increase with respect to the crack retarder unit weight, 82.2% g^{-1}, was observed in the ultrasonically consolidated crack retarder with two steel layers (2-AISI301-UCCR)[6].

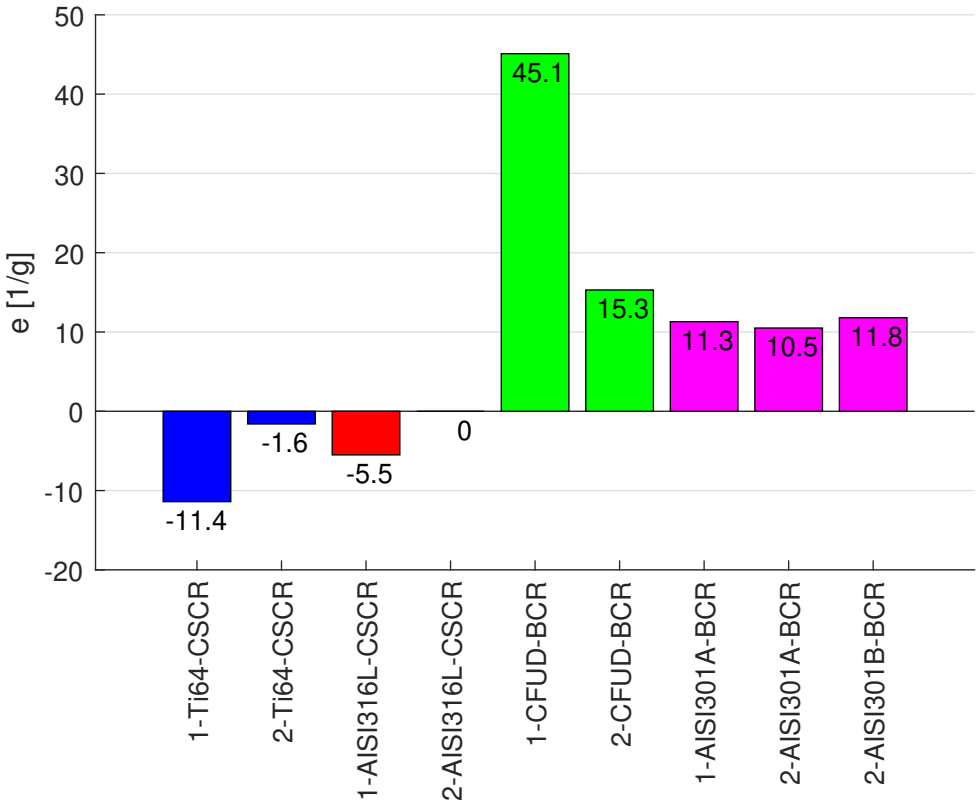

Figure 5.13: e factor: bonded and cold sprayed crack retarders.

All bonded crack retarders started delaminating in the end of specimen's fatigue life. The delamination in specimens with carbon fibre BCRs started later compared to the delamination in specimens with steel BCRs (Fig. 5.14). The steel crack retarders delaminated with continually increasing delamination rate. The earlier

[6]In this specimen, the precrack length was five times greater and the σ_{max} was 1.66 times greater compared to the specimens with bonded and cold sprayed crack retarders.

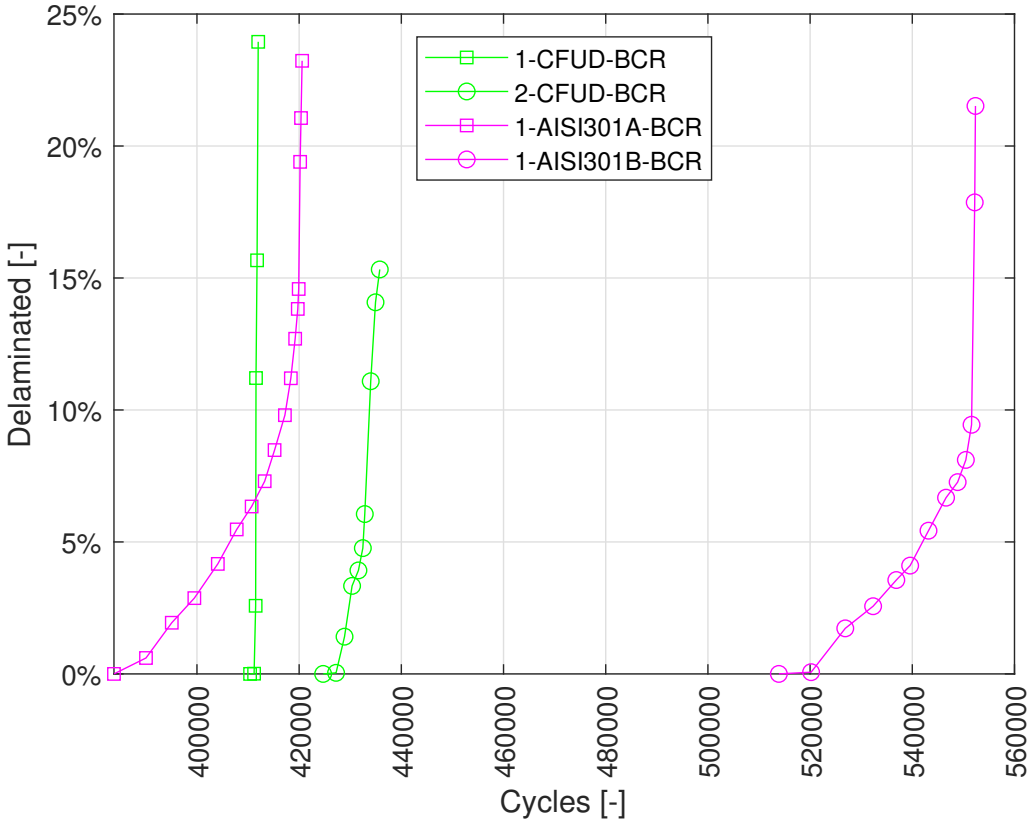

Figure 5.14: Delamination growth: bonded crack retarders.

onset of delamination in specimens with steel crack retarders can be attributed to the weaker joint strength. The fracture surface between CF UD crack retarder and substrate showed adhesive-cohesive failure. Conversely, fracture surface between steel crack retarder and substrate was purely adhesive failure. This suggests that if the joint strength (AISI 301/substrate) is increased, the fatigue retardation effect may be increased. The crack grew directly to the crack retarder without premature delamination in all specimens with cold-sprayed crack retarders. Samely, ultrasonically consolidated crack retarder with one steel layer (1-AISI301-UCCR) did not delaminate, the crack grew directly into him. However, the delamination in ultrasonically consolidated crack retarder with two steel layers (2-AISI301-UCCR) followed the same trend as the bonded crack retarders (Fig. 5.15); two steel layers start to delaminate in the end of specimen's fatigue life. Moreover, the delamination shape in consolidated crack retarder (Fig. A.5) is similar to the shape in bonded crack retarders (Fig. A.4).

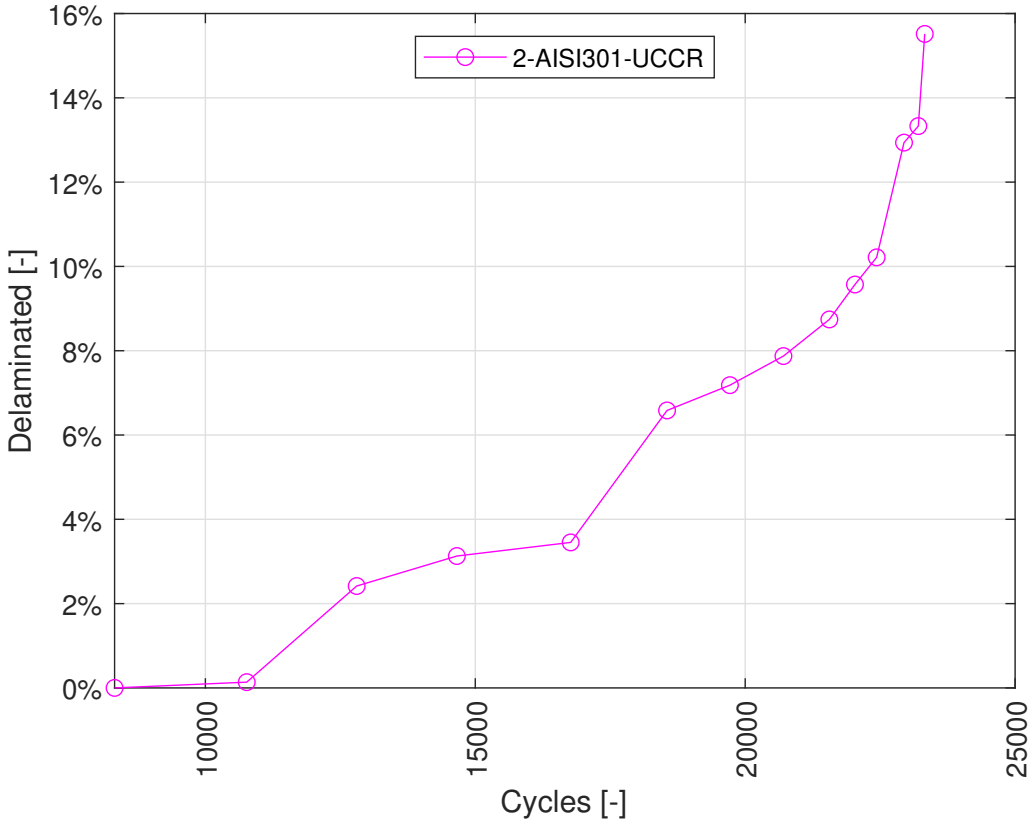

Figure 5.15: Delamination growth: 2-AISI301-UCCR specimen.

Chapter 6

Conclusion

From the results discussed in the previous chapter, the following conclusions can be drawn:

- Fatigue life of aluminum structure can be significantly improved using the bonded crack retarders made of AISI 301, CF UD/epoxy and ultrasonically consolidated crack retarders made of AISI 301/Al. The greatest increase by a factor 7.2 was recorded in specimen with ultrasonically consolidated AISI 301/Al crack retarder.

- Utilizing bonded CF UD/epoxy, AISI 301 crack retarders and ultrasonically consolidated AISI 301/Al crack retarder; the fatigue crack growth rate in the aluminum structure can be significantly decreased.

- The greatest percentage of life improvement with respect to the bare specimen per gram weight of crack retarder, 82.2% g^{-1}, was detected in the specimen with ultrasonically consolidated AISI 301/Al crack retarder.

- The delamination in AISI 301/Al laminate can be recorded using pulsed thermography. Thermographic signal reconstruction method proved to be a relevant approach to increase the contrast of delamination in ultrasonically consolidated AISI 301/Al laminate.

- The delamination growth between ultrasonically consolidated AISI 301/Al crack retarder and aluminum structure follows the same trend as delamination

between the bonded crack retarder and aluminum structure. The delamination patterns of bonded and ultrasonically consolidated crack retarders possess the similar shape.

6.1 Research implication and contribution

6.1.1 Practical

Through the application of crack retarder, the fatigue crack can experience stable growth for longer period of time. In other words, the critical crack length increases and thus the:

- aircraft maintenance interval will be longer [191]
- time to the first inspection (i. e. inspection threshold) will be longer [191]
- number of inspection might be reduced if maintenance tasks are fittingly associated
- crack detectability increases, since longer cracks are always easier to detect

A high-performance cars, boats and spacecrafts (Fig. 6.1) are other candidates that could benefit from the application of crack retarders. The crack retarder's influence to load capacity, fracture toughness, buckling resistance and residual strength was not examined in this thesis, however, the positive impact on all these structural properties is strikingly obvious because of the stiffening effect.

6.1.2 Scientific

This thesis:

- Compares the impact of novel material combinations and technologies on the fatigue crack growth rate and the delamination growth.
- Brings the experimental data for the calibration of predictive models that may involve the delamination growth.

- Marks the potential dead end; the cold spray deposit might increase the fatigue crack growth rate and thus decrease the fatigue life.

- Proves that the delamination in the ultrasonically consolidated metal laminates can be detected using the pulsed thermography.

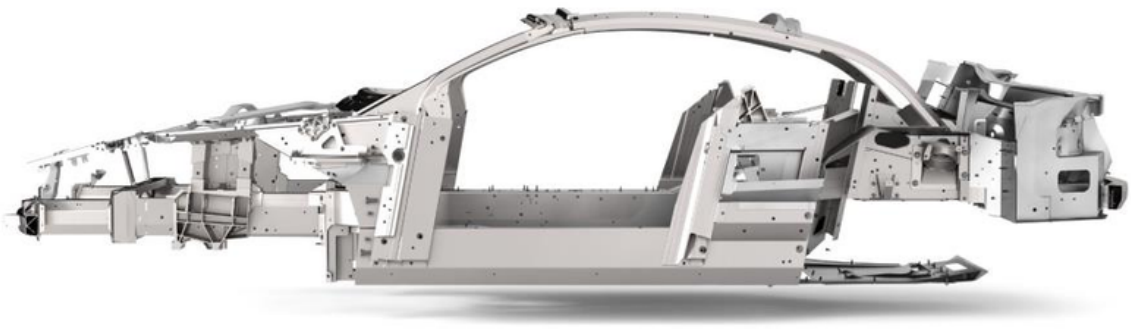

(a) Aston Martin Vanquish [192]

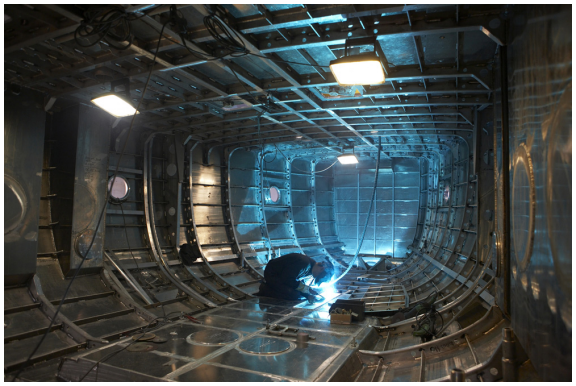

(b) Yacht made by KM Yachtbuilders [193]

(c) Sentinel 2 MSI Structure with external structural doubler [194]

Figure 6.1: Aluminum structures

6.2 Future research ideas

Manufacturing technologies may lead to the induction of thermal residual stresses. Because these stresses affects the performance of crack retarder, their levels must be investigated. Studies discussing the effect of ultrasonic consolidation and cold spraying on the thermal residual stress levels are scarce.

Studies focused on the delamination detactability and growth in cold sprayed and ultrasonically consolidated structures under cyclic loading are lacking. Finding the useful NDT method is necessary to design aircraft maintenance plan. Moreover, the delamination data would be useful for predictive models.

The crack retarders need to be rigorously tested before their application in real structure. It would involve testing of various designs at various stress levels, stress ratios and cyclic loadings (CA,VA). Moreover, these tests must be performed at the flight level atmospheric conditions, i.e. low temperature. The results from such extensive testing can be used to calibrate the fatigue crack growth prediction models incorporating delamination growth and thermal residual stresses. Such models for cold sprayed and ultrasonically consolidated structures are lacking.

Ultrasonically consolidated specimen that was damaged during the test machine failure demonstrated the outstanding formability. Since that accident, two research topics have arisen: (1) research on the formability of ultrasonically consolidated laminates made of dissimilar metals and (2) the impact of metal forming residual stresses on the fatigue crack growth in ultrasonically consolidated laminates.

Utilizing the ultrasonic consolidation, the amount of stress transfered from substrate to crack retarder was increased. In the crack retarder of 1-AISI301-UCCR specimen, such stress level allowed the crack to nucleate. Lowering the joint strength, the stress levels might decrease to the point that the fatigue crack do not nucleate. Finding the optimal consolidation process parameters is the another problem to be solved.

References

[1] G. I. Nestrenko, "Comparison of damage tolerance of integrally stiffened and riveted structures," in *22nd International Congress of Aeronautical Sciences*, 2000.

[2] S. Findlay and N. Harrison, "Why aircraft fail," *Materials Today*, vol. 5, no. 11, pp. 18–25, 2002, ISSN: 1369-7021. DOI: 10.1016/S1369-7021(02)01138-0.

[3] M. Boscolo, G. Allegri, and X. Zhang, "Design and modelling of selective reinforcements for integral aircraft structures," *AIAA journal*, vol. 46, no. 9, pp. 2323–2331, 2008.

[4] M. C. Dixon, *The Maintenance Costs of Aging Aircraft: Insights from Commercial Aviation*. Santa Monica, CA: RAND Corporation, 2006.

[5] J. Schijve, "Crack stoppers and ARALL laminates," *Engineering Fracture Mechanics*, vol. 37, no. 2, pp. 405–421, 1990.

[6] G. Farley, J. Newman, and M. James, "Selective reinforcement to improve fracture toughness and fatigue crack growth resistance in metallic structures," in *45th AIAA/ASME/ASCE/AHS/ASC Structures, Structural Dynamics & Materials Conference*, 2004, p. 1924.

[7] X. Zhang and Y. Li, "Damage tolerance and fail safety of welded aircraft wing panels," *AIAA journal*, vol. 43, no. 7, pp. 1613–1623, 2005.

[8] M. Colavita, A. Bowler, X. Zhang, and P. E. Irving, "Adhesively bonded cfrp straps as fatigue crack growth retarders on AA2024-T3," in *Proceedings of SAMPE Conference 2006*, 2006.

[9] X. Zhang, M. Boscolo, D. Figueroa-Gordon, G. Allegri, and P. E. Irving, "Fail-safe design of integral metallic aircraft structures reinforced by bonded crack retarders," *Engineering Fracture Mechanics*, vol. 76, no. 1, pp. 114–133, 2009.

[10] F. Tahmasebi, "Software tools for analysis of bonded joints," NASA/GSFC, Tech. Rep. 542, 2001.

[11] M. Boscolo, "A finite element analysis of bonded crack retarders for integral aircraft structures," PhD thesis, Cranfield University, Apr. 2009.

[12] C. Liljedahl, M. Fitzpatrick, and L. Edwards, "Distortion and residual stresses in structures reinforced with titanium straps for improved damage tolerance," *Materials Science and Engineering: A*, vol. 486, no. 1-2, pp. 104–111, 2008.

[13] C. Liljedahl, M. Fitzpatrick, O. Zanellato, and L. Edwards, "Evolution of residual stresses with fatigue crack growth in integral structures with crack retarders," *Materials Science and Engineering: A*, vol. 523, no. 1-2, pp. 152–159, 2009.

[14] P. M. Moreira and P. M. de Castro, "Fractographic analysis of fatigue crack growth in lightweight integral stiffened panels," *International Journal of Structural Integrity*, vol. 1, no. 3, pp. 233–258, 2010.

[15] P. E. Irving, X. Zhang, J. Doucet, D. Figueroa-Gordon, M. Boscolo, M. Heinimann, G. Shepherd, M. Fitzpatrick, and D. Liljedahl, "Life extension techniques for aircraft structures–extending durability and promoting damage tolerance through bonded crack retarders," in *ICAF 2011 structural integrity: influence of efficiency and green imperatives*, Springer, 2011, pp. 753–770.

[16] C. Liljedahl, M. Fitzpatrick, and L. Edwards, "Residual stresses in structures reinforced with adhesively bonded straps designed to retard fatigue crack growth," *Composite Structures*, vol. 86, no. 4, pp. 344–355, 2008.

[17] C. Liljedahl, M. Fitzpatrick, O. Zanellato, and L. Edwards, "Effect of temperature on the residual stresses in an integral structure with a crack-retarding patch," *Strain*, vol. 47, pp. 293–298, 2011.

[18] A. Brot, I. Kressel, S. Häusler, P. Baiz, S. Tavares, P. Horst, and J. Klement, "Analytical and experimental investigations of extending the crack growth life of integrally stiffened aluminum panels by the use of composite material strips," *Structural Durability & Health Monitoring*, vol. 7, no. 3, pp. 153–162, 2011.

[19] Y. E. Ma, B. Q. Liu, and Z. Q. Zhao, "The effects of bonded retarder on fatigue crack growth in 7085 aluminium alloy," in *Advanced Materials Research*, Trans Tech Publ, vol. 217, 2011, pp. 1135–1140.

[20] I. Meneghin, G. Ivetic, and E. Troiani, "Analysis of residual stress effect on fatigue crack propagation in bonded aeronautical stiffened panels," in *Materials Science Forum*, Trans Tech Publ, vol. 681, 2011, pp. 236–242.

[21] G. Molinari, I. Meneghin, M. Melega, and E. Troiani, "Parametric damage tolerance design of metallic aeronautical stiffened panels," *The Aeronautical Journal*, vol. 116, no. 1182, pp. 815–831, 2012.

[22] J. Doucet, X. Zhang, and P. Irving, "Fatigue modelling of aluminium plates reinforced with bonded fibre metal laminates," *International Journal of Structural Integrity*, vol. 4, no. 4, pp. 416–428, 2013.

[23] J. Doucet, "Fatigue life enhancement of aircraft structures through bonded crack retarders (BCR)," PhD thesis, Cranfield University, Sep. 2015.

[24] Y. E. Ma and P. F. Xu, "Effects of bonded crack retarders on fatigue parameters of FSWed integral panel," in *Advanced Materials Research*, Trans Tech Publ, vol. 891, 2014, pp. 627–632.

[25] A. K. Syed, M. E. Fitzpatrick, J. E. Moffatt, J. Doucet, and I. Durazo-Cardenas, "Effect of impact damage on fatigue performance of structures reinforced with GLARE bonded crack retarders," *International Journal of Fatigue*, vol. 80, pp. 231–237, 2015.

[26] A. K. Syed, "Durability of bonded crack retarders for aerospace," PhD thesis, The Open University, Jun. 2014.

[27] L. Llopart, B. Kurz, C. Wellhausen, M. Anglada, K. Drechsler, and K. Wolf, "Investigation of fatigue crack growth and crack turning on integral stiffened structures under mode I loading," *Engineering fracture mechanics*, vol. 73, no. 15, pp. 2139–2152, 2006.

[28] M.-V. Uz, M. Koçak, F. Lemaitre, J.-C. Ehrström, S. Kempa, and F. Bron, "Improvement of damage tolerance of laser beam welded stiffened panels for airframes via local engineering," *International Journal of Fatigue*, vol. 31, no. 5, pp. 916–926, 2009.

[29] R. Sepe, E. Armentani, G. Lamanna, and F. Caputo, "Fatigue behaviour of full scale flat stiffened aeronautic panels," in *Key Engineering Materials*, Trans Tech Publ, vol. 627, 2015, pp. 97–100.

[30] J. Lu, N. Kashaev, and N. Huber, "Crenellation patterns for fatigue crack retardation in fuselage panels optimized via genetic algorithm," *Procedia Engineering*, vol. 114, pp. 248–254, 2015.

[31] J. Liu, L. Wu, M. Song, Y. Hu, M. Lei, and F. Berto, "Crack resistance behaviour of aluminium alloy for aircraft skin with bionic coupling units processed by laser cladding," *Fatigue & Fracture of Engineering Materials & Structures*, vol. 43, no. 11, pp. 2756–2760, 2020. DOI: https://doi.org/10.1111/ffe.13315.

[32] R. Jones, N. Matthews, C. Rodopoulos, K. Cairns, and S. Pitt, "On the use of supersonic particle deposition to restore the structural integrity of damaged aircraft structures," *International Journal of Fatigue*, vol. 33, no. 9, pp. 1257–1267, 2011.

[33] R. Jones, L. Molent, S. Barter, N. Matthews, and D. Tamboli, "Supersonic particle deposition as a means for enhancing the structural integrity of aircraft structures," *International Journal of Fatigue*, vol. 68, pp. 260–268, 2014.

[34] M. Dorman, M. Toparli, N. Smyth, A. Cini, M. Fitzpatrick, and P. Irving, "Effect of laser shock peening on residual stress and fatigue life of clad 2024 aluminium sheet containing scribe defects," *Materials Science and Engineering: A*, vol. 548, pp. 142–151, 2012.

[35] X. Zhang, S. Hao, T. Grosdidier, J. Zou, B. Gao, B. Bolle, N. Allain-Bonasso, Y. Qin, X. Li, and C. Dong, "Surface modification of light alloys by low-energy high-current pulsed electron beam," *Journal of Metallurgy*, vol. 2012, 2012.

[36] Y. Ivanov, K. Alsaraeva, V. Gromov, S. Konovalov, and O. Semina, "Evolution of Al-19· 4Si alloy surface structure after electron beam treatment and high cycle fatigue," *Materials science and technology*, vol. 31, no. 13, pp. 1523–1529, 2015.

[37] J.-R. Hwang and C.-P. Fung, "Effect of electron beam surface hardening on fatigue crack growth rate in AISI 4340 steel," *Surface and Coatings Technology*, vol. 80, no. 3, pp. 271–278, 1996.

[38] V. Saxena, N. Moiuddin, and V. Radhakrishnan, "Electron beam irradiation effects on fatigue crack growth resistance in an austenitic steel," *International Journal of Fatigue*, vol. 16, no. 7, pp. 479–484, 1994.

[39] D. Schnubel, M. Horstmann, V. Ventzke, S. Riekehr, P. Staron, T. Fischer, and N. Huber, "Retardation of fatigue crack growth in aircraft aluminium alloys via laser heating–experimental proof of concept," *Materials Science and Engineering: A*, vol. 546, pp. 8–14, 2012.

[40] D. Schnubel and N. Huber, "Retardation of fatigue crack growth in aircraft aluminium alloys via laser heating–numerical prediction of fatigue crack growth," *Computational Materials Science*, vol. 65, pp. 461–469, 2012.

[41] A. Groth, N. Kashaev, and N. Huber, "Introducing residual stresses in thin aluminium structures by laser generated temperature fields," in *Proceedings of 29th Congress of the International Council of the Aeronautical Sciences, St. Petersburg*, 2014.

[42] M. C. da Cunha and M. S. F. de Lima, "The influence of laser surface treatment on the fatigue crack growth of AA 2024-T3 aluminum alloy alclad sheet," *Surface and Coatings Technology*, vol. 329, pp. 244–249, 2017.

[43] V. Irick and B. Gordon, "Metpreg: Metallic prepregs for the composites industry.," *SAMPE journal*, 2004.

[44] R. K. Bird, J. A. Alexa, P. L. Messick, M. S. Domack, and J. A. Wagner, "Investigation of methods for selectively reinforcing aluminum and aluminum-lithium materials," 2013.

[45] A. Hehr, J. Wenning, M. Norfolk, J. Sheridan, J. A. Newman, and M. Domack, "Selective reinforcement of aerospace structures using ultrasonic additive manufacturing," *Journal of Materials Engineering and Performance*, pp. 1–8,

[46] P. Cavaliere and A. Silvello, "Fatigue behaviour of cold sprayed metals and alloys: Critical review," *Surface Engineering*, vol. 32, no. 9, pp. 631–640, 2016. DOI: 10.1179/1743294415Y.0000000100.

[47] D. K. Christoulis, S. Guetta, V. Guipont, and M. Jeandin, "The influence of the substrate on the deposition of cold-sprayed titanium: An experimental and numerical study," *Journal of Thermal Spray Technology*, vol. 20, no. 3, pp. 523–533, 2011.

[48] N. Cinca, M. Barbosa, S. Dosta, and J. Guilemany, "Study of Ti deposition onto Al alloy by cold gas spraying," *Surface and Coatings Technology*, vol. 205, no. 4, pp. 1096–1102, 2010.

[49] M. Villa, S. Dosta, and J. Guilemany, "Optimization of 316L stainless steel coatings on light alloys using cold gas spray," *Surface and Coatings Technology*, vol. 235, pp. 220–225, 2013.

[50] B. Dikici, I. Ozdemir, and M. Topuz, "Cold spray deposition of SS316L powders on Al5052 substrates and their potential using for biomedical applications," *Int J Chem Mol Nucls Mater Metall Eng*, vol. 10, no. 4, pp. 483–487, 2016.

[51] A. Alhazaa and T. Khan, "Diffusion bonding of Al7075 to Ti-6Al-4V using cu coatings and Sn-3.6 Ag-1Cu interlayers," *Journal of Alloys and Compounds*, vol. 494, no. 1-2, pp. 351–358, 2010.

[52] M. Samavatian, A. Halvaee, A. A. Amadeh, and A. Khodabandeh, "An investigation on microstructure evolution and mechanical properties during liquid state diffusion bonding of Al2024 to Ti-6Al-4V," *Materials Characterization*, vol. 98, pp. 113–118, 2014.

[53] M. Samavatian, A. Khodabandeh, A. Halvaee, and A. A. AMADEH, "Transient liquid phase bonding of Al 2024 to Ti-6Al-4V alloy using Cu-Zn interlayer," *Transactions of Nonferrous Metals Society of China*, vol. 25, no. 3, pp. 770–775, 2015.

[54] A. Anbarzadeh, H. Sabet, and M. Abbasi, "Effects of successive-stage transient liquid phase (S-TLP) on microstructure and mechanical properties of Al2024 to Ti-6Al-4V joint," *Materials Letters*, vol. 178, pp. 280–283, 2016.

[55] N. Shamsaei, A. Yadollahi, L. Bian, and S. M. Thompson, "An overview of direct laser deposition for additive manufacturing; Part II: Mechanical behavior, process parameter optimization and control," *Additive Manufacturing*, vol. 8, pp. 12–35, 2015.

[56] W. MacDonald and T. Eagar, "Transient liquid phase bonding processes," *The Metal Science of Joining*, pp. 93–100, 1992.

[57] *Fabrisonic's 3D metal printing design guide and frequently asked questions*, Fabrisonic LLC, 2018.

[58] C. Zhang, J. Robson, and P. Prangnell, "Dissimilar ultrasonic spot welding of aerospace aluminum alloy AA2139 to titanium alloy TiAl6V4," *Journal of Materials Processing Technology*, vol. 231, pp. 382–388, 2016.

[59] P. J. Wolcott, N. Sridharan, S. S. Babu, A. Miriyev, N. Frage, and M. J. Dapino, "Characterisation of Al–Ti dissimilar material joints fabricated using ultrasonic additive manufacturing," *Science and Technology of Welding and Joining*, vol. 21, no. 2, pp. 114–123, 2016. DOI: 10.1179/1362171815Y.0000000072.

[60] T. L. Anderson, *Fracture mechanics: fundamentals and applications*. CRC press, 2017.

[61] G. R. Irwin, "Analysis of stresses and strains near the end of a crack traversing a plate," *Journal of Applied Mechanics*, vol. 24, pp. 361–364, 1957.

[62] D. Rooke, D. Cartwright, and G. B. M. of Defence. Procurement Executive, *Compendium of Stress Intensity Factors*, ser. Procurement executive, ministry of defence. H.M. Stationery Office, 1976, ISBN: 9780117713369.

[63] H. Tada, A. Press, P. Paris, and G. Irwin, *The Stress Analysis of Cracks Handbook*. ASME Press, 2000, ISBN: 9780791801536.

[64] Y. Murakami, *Stress intensity factors handbook*, sv. 1. Pergamon, 1987, ISBN: 9780080348094.

[65] J. Dixon and L. Pook, "Stress intensity factors calculated generally by the finite element technique," *Nature*, vol. 224, no. 5215, pp. 166–167, 1969, cited By 32. DOI: 10.1038/224166a0.

[66] T. A. Cruse, "Numerical evaluation of elastic stress intensity factors by the boundary-integral equation method," *Surface Crack, Physical Problems and Computational Solutions, ASME New York*, pp. 153–170, 1972.

[67] Y. Chen and M. Wilkins, "Stress analysis of crack problems with a three-dimensional, time-dependent computer program," *International Journal of Fracture*, vol. 12, no. 4, pp. 607–617, 1976. DOI: 10.1007/BF00034646.

[68] G. Green, *An Essay on the Application of Mathematical Analysis to the Theories of Electricity and Magnetism*, ser. (Göteborg: Wezäta-Melins 1958). author, 1828.

[69] D. J. Cartwright and D. Rooke, "Green's functions in fracture mechanics," in *Fracture Mechanics*, Elsevier, 1979, pp. 91–123.

[70] H. Westergaard, "Bearing pressures and cracks," 1939.

[71] G. B. S. Airy, "Iv. on the strains in the interior of beams," *Philosophical Transactions of the Royal Society of London*, pp. 49–79, 1863.

[72] B. HF, "Novel principle for the computation of stress intensity factors," *Z Angew Math Mech*, vol. 50, no. 9, pp. 529–546, 1970.

[73] J. Dally and R. Sanford, "Strain-gage methods for measuring the opening-mode stress-intensity factor, KI," *Experimental Mechanics*, vol. 27, no. 4, pp. 381–388, 1987.

[74] R. Marloff, M. Leven, T. Ringler, and R. Johnson, "Photoelastic determination of stress-intensity factors," *Experimental Mechanics*, vol. 11, no. 12, pp. 529–539, 1971.

[75] O. Kolednik and H. Stüwe, "The stereophotogrammetric determination of the critical crack tip opening displacement," *Engineering Fracture Mechanics*, vol. 21, no. 1, pp. 145–155, 1985.

[76] R. Narasimhan and A. J. Rosakis, "Three-Dimensional Effects Near a Crack Tip in a Ductile Three-Point Bend Specimen: Part I—A Numerical Investigation," *Journal of Applied Mechanics*, vol. 57, no. 3, pp. 607–617, 1990, ISSN: 0021-8936. DOI: 10.1115/1.2897066.

[77] J. Schijve, H. Van Lipzig, G. Van Gestel, and A. Hoeymakers, "Fatigue properties of adhesive-bonded laminated sheet material of aluminum alloys," *Engineering Fracture Mechanics*, vol. 12, no. 4, pp. 561–579, 1979.

[78] A. Griffith, "The phenomena of rupture and flow in solids," *Philosophical Transactions*, vol. 221, pp. 163–198, 1920.

[79] G. R. Irwin, "Onset of fast crack propagation in high strength steel and aluminum alloys," Naval Research Lab Washington DC, Tech. Rep., 1956.

[80] E. Rybicki and M. Kanninen, "A finite element calculation of stress intensity factors by a modified crack closure integral," *Engineering Fracture Mechanics*, vol. 9, no. 4, pp. 931–938, 1977, ISSN: 0013-7944. DOI: 10.1016/0013-7944(77)90013-3.

[81] V. Jetela, J. Klement, and P. Augustin, "The possibility for improving damage tolerance of integral airframe structure by high strength bonded straps," *Manufacturing Technology*, vol. 18, no. 4, pp. 572–577, 2018. DOI: 10.21062/ujep/152.2018/a/1213-2489/MT/18/4/572.

[82] J. Schijve, *Fatigue of Structures and Materials*. Springer Netherlands, 2009, ISBN: 9789048119066.

[83] P. Chowdhury and H. Sehitoglu, "Mechanisms of fatigue crack growth–a critical digest of theoretical developments," *Fatigue & Fracture of Engineering Materials & Structures*, vol. 39, no. 6, pp. 652–674, 2016.

[84] R. J. H. Wanhill, "Low stress intensity fatigue crack growth in 2024-T3 and T351," *Engineering Fracture Mechanics*, vol. 30, no. 2, pp. 233–260, 1988.

[85] *Standard test method for measurement of fatigue crack growth rates*, `https://www.astm.org/standards/e647`, Accessed: 2022-03-10.

[86] P. Paris and F. Erdogan, "A Critical Analysis of Crack Propagation Laws," *Journal of Basic Engineering*, vol. 85, no. 4, pp. 528–533, Dec. 1963, ISSN: 0021-9223. DOI: `10.1115/1.3656900`.

[87] R. Forman and S. Mettu, "Behavior of surface and corner cracks subjected to tensile and bending loads in Ti-6Al-4V alloy," Tech. Rep., Sep. 1990.

[88] J. C. Newman, "A crack opening stress equation for fatigue crack growth," Tech. Rep., 1984, R131–R135.

[89] C. Laird, "The influence of metallurgical structure on the mechanisms of fatigue crack propagation," in *Fatigue crack propagation*, ASTM International, 1967.

[90] C. Laird and G. Smith, "Crack propagation in high stress fatigue," *Philosophical Magazine*, vol. 7, no. 77, pp. 847–857, 1962.

[91] A. McEvily Jr and R. Boettner, "On fatigue crack propagation in FCC metals," *Acta Metallurgica*, vol. 11, no. 7, pp. 725–743, 1963.

[92] P. Neumann, "Coarse slip model of fatigue," *Acta metallurgica*, vol. 17, no. 9, pp. 1219–1225, 1969.

[93] P. Neumann, "The geometry of slip processes at a propagating fatigue crack—ii," *Acta Metallurgica*, vol. 22, no. 9, pp. 1167–1178, 1974.

[94] R. Pippan, C. Zelger, E. Gach, C. Bichler, and H. WeinhadlL, "On the mechanism of fatigue crack propagation in ductile metallic materials," *Fatigue & Fracture of Engineering Materials & Structures*, vol. 34, no. 1, pp. 1–16, 2011. DOI: `10.1111/j.1460-2695.2010.01484.x`.

[95] H. A. Richard and M. Sander, *Fatigue crack growth*. Springer, 2016.

[96] B. Mohamed, B. Bouchouicha, M. Zemri, and M. Mazari, "Crack propagation under constant amplitude loading based on an energetic parameters and fractographic analysis," *Materials Research*, vol. 15, pp. 544–548, Aug. 2012. DOI: `10.1590/S1516-14392012005000072`.

[97] Y. Xu, P. J. Gregson, and I. Sinclair, "Dispersoid and grain size effects on fatigue crack growth in AA2024-type alloys," in *Aluminium Alloys - Their Physical and Mechanical Properties*, ser. Materials Science Forum, vol. 331, Trans Tech Publications Ltd, May 2000, pp. 1525–1530. DOI: `10.4028/www.scientific.net/MSF.331-337.1525`.

[98] S. Kim, S. Han, and J. Zong, "Fatigue crack growth in 2024 aluminum alloy with inhomogeneous solidification microstructure," *Metals and materials international*, vol. 11, no. 6, p. 443, 2005.

[99] M. Benachour, M. Benguediab, A. Hadjoui, and N. Benachour, "Prediction of fatigue crack growth of aeronautical aluminum alloy," *International Journal of Aerospace and Mechanical Engineering*, vol. 4, no. 8, pp. 692–695, 2010, ISSN: eISSN: 1307-6892.

[100] A. Oldersma and R. Wanhill, "Variability of fatigue crack growth properties for 2024-t3 aluminium alloy.," National Aerospace Laboratory NLR, Tech. Rep., 1996.

[101] M. Benachour, M. Benguediab, A. Hadjoui, N. Benachour, and F. Hadjoui, "Fatigue crack growth of different aluminum alloy 2024," in *Multilevel Approach to Fracture of Materials, Components and Structures*, VUTIUM, Sep. 2008, pp. 1047–1052.

[102] C. Purry, A. Fien, and K. Shankar, "The effect of corrosion preventative compound on fatigue crack growth properties of 2024-T351 aluminium alloys," *International journal of fatigue*, vol. 25, no. 9-11, pp. 1175–1180, 2003.

[103] F. Menan and G. Henaff, "Influence of frequency and exposure to a saline solution on the corrosion fatigue crack growth behavior of the aluminum alloy 2024," *International journal of fatigue*, vol. 31, no. 11-12, pp. 1684–1695, 2009.

[104] F. Menan and G. Henaff, "Synergistic action of fatigue and corrosion during crack growth in the 2024 aluminium alloy," *Procedia Engineering*, vol. 2, no. 1, pp. 1441–1450, 2010.

[105] J. Petit, G. Henaff, and C. Sarrazin-Baudoux, "Environmentally assisted fatigue in the gaseous atmosphere," *Comprehensive structural integrity*, vol. 6, pp. 211–280, 2003.

[106] R. Piascik and R. Gangloff, "Environmental fatigue of an Al-Li-Cu alloy: Part I. Intrinsic crack propagation kinetics in hydrogenous environments," *Metallurgical Transactions A*, vol. 22, no. 10, pp. 2415–2428, 1991.

[107] ——, "Environmental fatigue of an Al-Li-Cu alloy: Part II. Microscopic hydrogen cracking processes," *Metallurgical and Materials Transactions A*, vol. 24, no. 12, pp. 2751–2762, 1993.

[108] F. Bradshaw and C. Wheeler, "The effect of gaseous environment and fatigue frequency on the growth of fatigue cracks in some aluminium alloys," *Int. J. Fracture Mech*, vol. 6, pp. 255–268, 1969.

[109] A. Noroozi, G. Glinka, and S. Lambert, "A study of the stress ratio effects on fatigue crack growth using the unified two-parameter fatigue crack growth driving force," *International journal of fatigue*, vol. 29, no. 9-11, pp. 1616–1633, 2007.

[110] R. R. Cervay, "An empirical model for load ration and test temperature effects on the fatigue crack growth rate of aluminum alloy 2024-T351," University of Dayton Research Institute, Tech. Rep. ADA116567, 1982.

[111] P. Abelkis, M. Harmon, E. Hayman, T. Mackay, and J. Orlando, "Low temperature and loading frequency effects on crack growth and fracture toughness of 2024 and 7475 aluminum," in *Fatigue at Low Temperatures*, ASTM International, 1985, pp. 257–273. DOI: 10.1520/STP32760S.

[112] D. Broek and J. Schijve, "The influence of sheet thickness on crack propagation," *Aircraft Engineering and Aerospace Technology*, 1966.

[113] J. J. Schubbe, "Thickness effects on a cracked aluminum plate with composite patch repair," PhD thesis, Air Force Institute of Technology Wright-Patterson AFB, Jun. 1997.

[114] A. Hartman and J. Schijve, "The effects of environment and load frequency on the crack propagation law for macro fatigue crack growth in aluminium alloys," *Engineering Fracture Mechanics*, vol. 1, no. 4, pp. 615–631, 1970.

[115] C. Liljedahl, J. Brouard, O. Zanellato, J. Lin, M. Tan, S. Ganguly, P. E. Irving, M. Fitzpatrick, X. Zhang, and L. Edwards, "Weld residual stress effects on fatigue crack growth behaviour of aluminium alloy 2024-t351," *International Journal of Fatigue*, vol. 31, no. 6, pp. 1081–1088, 2009.

[116] G. Bussu and P. Irving, "The role of residual stress and heat affected zone properties on fatigue crack propagation in friction stir welded 2024-T351 aluminium joints," *International Journal of Fatigue*, vol. 25, no. 1, pp. 77–88, 2003.

[117] A. Papyrin, V. Kosarev, S. Klinkov, A. Alkhimov, and V. M. Formin, *Cold Spray Technology*. Amsterdam, Netherlands: Elsevier, 2007, ISBN: 978-0-08-045155-8.

[118] X. Wang, F. Feng, M. A. Klecka, M. D. Mordasky, J. K. Garofano, T. El-Wardany, A. Nardi, and V. K. Champagne, "Characterization and modeling of the bonding process in cold spray additive manufacturing," *Additive Manufacturing*, vol. 8, pp. 149–162, 2015.

[119] W. Wong, E. Irissou, A. N. Ryabinin, J.-G. Legoux, and S. Yue, "Influence of helium and nitrogen gases on the properties of cold gas dynamic sprayed pure titanium coatings," *Journal of Thermal Spray Technology*, vol. 20, no. 1-2, pp. 213–226, 2011.

[120] W. Wong, P. Vo, E. Irissou, A. Ryabinin, J.-G. Legoux, and S. Yue, "Effect of particle morphology and size distribution on cold-sprayed pure titanium coatings," *Journal of thermal spray technology*, vol. 22, no. 7, pp. 1140–1153, 2013.

[121] H. Assadi, T. Schmidt, H. Richter, J.-O. Kliemann, K. Binder, F. Gärtner, T. Klassen, and H. Kreye, "On parameter selection in cold spraying," *Journal of thermal spray technology*, vol. 20, no. 6, pp. 1161–1176, 2011.

[122] H. Assadi, H. Kreye, F. Gärtner, and T. Klassen, "Cold spraying–a materials perspective," *Acta Materialia*, vol. 116, pp. 382–407, 2016.

[123] J. Villafuerte, *Modern cold spray: materials, process, and applications*. Springer, 2015.

[124] R. Huang, M. Sone, W. Ma, and H. Fukanuma, "The effects of heat treatment on the mechanical properties of cold-sprayed coatings," *Surface and Coatings Technology*, vol. 261, pp. 278–288, 2015.

[125] R. Huang, W. Ma, and H. Fukanuma, "Development of ultra-strong adhesive strength coatings using cold spray," *Surface and Coatings Technology*, vol. 258, pp. 832–841, 2014.

[126] A. Sova, S. Grigoriev, A. Okunkova, and I. Smurov, "Cold spray deposition of 316L stainless steel coatings on aluminium surface with following laser post-treatment," *Surface and Coatings Technology*, vol. 235, pp. 283–289, 2013.

[127] O. C. Ozdemir, Q. Chen, S. Muftu, and V. K. Champagne, "Modeling the continuous heat generation in the cold spray coating process," *Journal of Thermal Spray Technology*, vol. 28, no. 1, pp. 108–123, 2019.

[128] E. Lin, I. Nault, O. C. Ozdemir, V. K. Champagne Jr, A. Nardi, and S. Müftü, "Thermo-mechanical deformation history and the residual stress distribution in cold spray," *Journal of Thermal Spray Technology*, 2020.

[129] T. Suhonen, T. Varis, S. Dosta, M. Torrell, and J. Guilemany, "Residual stress development in cold sprayed Al, Cu and Ti coatings," *Acta materialia*, vol. 61, no. 17, pp. 6329–6337, 2013.

[130] P. P. A. Mazza, F. Martini, B. Sala, M. Magi, M. P. Colombini, G. Giachi, F. Landucci, C. Lemorini, F. Modugno, and E. Ribechini, "A new palaeolithic discovery: Tar-hafted stone tools in a european mid-pleistocene bone-bearing bed," *Journal of Archaeological Science*, vol. 33, no. 9, pp. 1310–1318, 2006.

[131] P. R. Kozowyk, M. Soressi, D. Pomstra, and G. H. Langejans, "Experimental methods for the palaeolithic dry distillation of birch bark: Implications for the origin and development of neandertal adhesive technology," *Scientific reports*, vol. 7, no. 1, pp. 1–9, 2017.

[132] J. A. Gannon, "History and development of epoxy resins," in *High Performance Polymers: Their Origin and Development*, R. B. Seymour and G. S. Kirshenbaum, Eds., Dordrecht: Springer Netherlands, 1986, pp. 299–307, ISBN: 978-94-011-7073-4.

[133] P. Cognard, *5.1 The Wright Brothers*, 2005.

[134] S. Ebensajjad, *Handbook of adhesives and surface preparation*. Elsevier, 2011.

[135] J. J. Licari and D. W. Swanson, *Adhesives technology for electronic applications: materials, processing, reliability*. William Andrew, 2011.

[136] C. May, *Epoxy resins: chemistry and technology*. Routledge, 2018.

[137] B. Ellis *et al.*, *Chemistry and technology of epoxy resins*. Springer, 1993.

[138] F. H. Chung, "Unified theory and guidelines on adhesion," *Journal of applied polymer science*, vol. 42, no. 5, pp. 1319–1331, 1991.

[139] P. Cognard, *Handbook of adhesives and sealants: general knowledge, application of adhesives, new curing techniques*. Elsevier, 2006.

[140] M. A. Butt, A. Chughtai, J. Ahmad, R. Ahmad, U. Majeed, and I. Khan, "Theory of adhesion and its practical implications," *Journal of Faculty of Engineering & Technology*, vol. 2007, pp. 21–45, 2008.

[141] J. Marsh, L. Minel, M. Barthes-Labrousse, and D. Gorse, "Interaction of epoxy model molecules with aluminium, anodised titanium and copper surfaces: An XPS study," *Applied Surface Science*, vol. 133, no. 4, pp. 270–286, 1998.

[142] B. Derjaguin and V. Smilga, "Electronic theory of adhesion," *Journal of applied Physics*, vol. 38, no. 12, pp. 4609–4616, 1967.

[143] J. Venables, D. McNamara, J. Chen, T. Sun, and R. Hopping, "Oxide morphologies on aluminum prepared for adhesive bonding," *Applications of surface science*, vol. 3, no. 1, pp. 88–98, 1979.

[144] J. Venables, "Adhesion and durability of metal-polymer bonds," *Journal of Materials Science*, vol. 19, no. 8, pp. 2431–2453, 1984.

[145] G. W. Critchlow, "Review of methods for the surface treatments of aluminium," in *Review of Methods for Substrate Surface Treatments*, pp. 1-1–1-23.

[146] E. Kieronski, K. Knock, W. Fallon, and G. Walker, "Mechanism of adhesive in secondary bonding of fiberglass composites with peel ply surface preparation," in *Joining and Repair of Composite Structures*, ASTM International, pp. 78–91. DOI: 10.1520/STP12585S.

[147] M. Pizzorni, E. Lertora, C. Gambaro, C. Mandolfino, M. Salerno, and M. Prato, "Low-pressure plasma treatment of CFRP substrates for epoxy-adhesive bonding: An investigation of the effect of various process gases," *The International Journal of Advanced Manufacturing Technology*, vol. 102, no. 9-12, pp. 3021–3035, 2019.

[148] L.-F. Li and J.-P. Celis, "Pickling of austenitic stainless steels (a review)," *Canadian metallurgical quarterly*, vol. 42, no. 3, pp. 365–376, 2003.

[149] D. Lindell and R. Pettersson, "Pickling of process-oxidised austenitic stainless steels in HNO3-HF mixed acid," *Steel research international*, vol. 81, no. 7, pp. 542–551, 2010.

[150] *JSLA annealing & pickling process*, https://www.slideshare.net/tushar3081/annealing-pickling-process, 2015.

[151] R. I. M. Asri, W. Harun, and Y. Asmara, "Effect of acid pickling on microstructure and surface roughness of 316l stainless steel," in *National Conference for Postgraduate Research*, 2016, pp. 142–146.

[152] J. Peterka, *Lepení konstrukčních matriálů ve strojírenství*. SNTL, 1980.

[153] *Cold atmospheric plasma (CAP) treatment of metals for adhesive bonding*, https://www.twi-global.com/media-and-events/insights/cold-atmospheric-plasma-cap-treatment-of-metals-for-adhesive-bonding, 2020.

[154] F. Bouquet, J. Cuntz, and C. Coddet, "Influence of surface treatment on the durability of stainless steel sheets bonded with epoxy," *Journal of adhesion science and technology*, vol. 6, no. 2, pp. 233–242, 1992.

[155] J. J. Bikerman, "Causes of poor adhesion: Weak boundary layers," *Industrial & Engineering Chemistry*, vol. 59, no. 9, pp. 40–44, 1967.

[156] V. Jetela, *Hybride adhesive bonded joints of metals and composite materials*, 2016.

[157] J. D. Minford, "Durability evaluation of adhesive bonded structures," in *Adhesive bonding*, Springer, 1991, pp. 239–290.

[158] D. White, "Ultrasonic object consolidation," 6 519 500, Feb. 2003.

[159] A. Hehr and M. Norfolk, "A comprehensive review of ultrasonic additive manufacturing," *Rapid Prototyping Journal*, 2019.

[160] J. Gibert, "Dynamics of ultrasonic consolidation," PhD thesis, Clemson University, Dec. 2009.

[161] D. Li and R. Soar, "Influence of sonotrode texture on the performance of an ultrasonic consolidation machine and the interfacial bond strength," *Journal of Materials Processing Technology*, vol. 209, no. 4, pp. 1627–1634, 2009.

[162] C. Robinson, C. Zhang, G. Janaki Ram, E. J. Siggard, B. Stucker, and L. Li, "Maximum height to width ratio of freestanding structures built using ultrasonic consolidation," in *2006 International Solid Freeform Fabrication Symposium*, 2006.

[163] *Discussion with Fabrisonic LLC*, 2020.

[164] B. Langenecker, "Work-softening of metal crystals by alternating the rate of glide strain," *Acta metallurgica*, vol. 9, no. 10, pp. 937–940, 1961.

[165] H. T. Fujii, S. Shimizu, Y. S. Sato, and H. Kokawa, "High-strain-rate deformation in ultrasonic additive manufacturing," *Scripta Materialia*, vol. 135, pp. 125–129, 2017.

[166] D. R. White, "Ultrasonic consolidation of aluminum tooling," *Advanced materials & processes*, vol. 161, no. 1, pp. 64–65, 2003.

[167] M. Sriraman, M. Gonser, H. T. Fujii, S. Babu, and M. Bloss, "Thermal transients during processing of materials by very high power ultrasonic additive manufacturing," *Journal of Materials Processing Technology*, vol. 211, no. 10, pp. 1650–1657, 2011.

[168] X. Zhong, J. Feng, and S. Yao, "Temperature field modeling and experimental study on ultrasonic consolidation for Al-Ti foil," *Journal of Mechanical Science and Technology*, vol. 33, no. 6, pp. 2833–2840, 2019.

[169] D. Bourell, B. Stucker, J. Obielodan, A. Ceylan, L. Murr, and B. Stucker, "Multi-material bonding in ultrasonic consolidation," *Rapid prototyping journal*, 2010.

[170] H. Zhang, Y. Chao, and Z. Luo, "Effect of interlayer on microstructure and mechanical properties of Al–Ti ultrasonic welds," *Science and Technology of Welding and Joining*, vol. 22, no. 1, pp. 79–86, 2017.

[171] P. R. Pati, M. P. Satpathy, B. K. Nanda, B. C. Routara, and A. Pattanaik, "Dissimilar joining of Al/SS sheets with interlayers by ultrasonic spot welding: Microstructure and mechanical properties," *Materials Today: Proceedings*, 2020.

[172] J. Obielodan, B. Stucker, E. Martinez, J. Martinez, D. Hernandez, D. Ramirez, and L. Murr, "Optimization of the shear strengths of ultrasonically consolidated Ti/Al 3003 dual-material structures," *Journal of Materials Processing Technology*, vol. 211, no. 6, pp. 988–995, 2011.

[173] R. Ritchie, "Mechanisms of fatigue crack propagation in metals, ceramics and composites: Role of crack tip shielding," *Materials Science and Engineering: A*, vol. 103, no. 1, pp. 15–28, 1988.

[174] R. Ritchie, W. Yu, and R. Bucci, "Fatigue crack propagation in ARALL® laminates: Measurement of the effect of crack-tip shielding from crack bridging," *Engineering Fracture Mechanics*, vol. 32, no. 3, pp. 361–377, 1989.

[175] J. M. Arenas, J. J. Narbón, and C. Alıa, "Optimum adhesive thickness in structural adhesives joints using statistical techniques based on weibull distribution," *International Journal of Adhesion and Adhesives*, vol. 30, no. 3, pp. 160–165, 2010.

[176] S. Marzi, A. Biel, and U. Stigh, "On experimental methods to investigate the effect of layer thickness on the fracture behavior of adhesively bonded joints," *International Journal of Adhesion and Adhesives*, vol. 31, no. 8, pp. 840–850, 2011.

[177] R. Clark and D. Romilly, "Linear coupled bending and extension of an unbalanced bonded repair," *International journal of solids and structures*, vol. 44, no. 10, pp. 3156–3176, 2007.

[178] J. Schijve, G. Campoli, and A. Monaco, "Fatigue of structures and secondary bending in structural elements," *International Journal of Fatigue*, vol. 31, no. 7, pp. 1111–1123, 2009.

[179] W. Wallace, D. W. Hoeppner, and P. Kandachar, *AGARD Corrosion Handbook. Volume 1. Aircraft Corrosion: Causes and Case Histories*. Advisory Group for Aerospace Research and Development, Neuilly-Sur-Seine (France), 1985, ISBN: 92-835-1505-6.

[180] *ASM Handbook, Volume 2: Properties and selection: Nonferrous alloys and special-purpose materials*. Materials Park, Ohio: ASM International, 1990, ISBN: 978-0-87170-378-1.

[181] P. Dymáček and J. Klement, "Properties and manufacturing of steel-C/epoxy fiber-metal laminates," in *Proceedings of the Fourth Seminar on Recent Research and Design Progress in Aeronautical Engineering and its Influence on Education: Part II*, Institute of Aeronautics and Applied Mechanics, 2011, pp. 47–52.

[182] *ASM Handbook, Volume 1: Properties and Selection: Irons, Steels, and High-Performance Alloys*. Materials Park, Ohio: ASM International, 1990, ISBN: 978-0-87170-377-4.

[183] *HexPly® M10R*, Hexcel, 2015.

[184] *Araldite® 2011 (AW106 + HW953U): Two component epoxy paste adhesive*, Huntsman Advanced Materials, 2004.

[185] Sandvik. (2019). Austenitic stainless steel metal powder, [Online]. Available: `https://www.materials.sandvik/cz/produkty/metal-powder/list-of-materials/austenitic-stainless-steels/`.

[186] AP&C. (2019). Ti-6Al-4V (15-45 µm), [Online]. Available: `http://advancedpowders.com/nos-poudres-atomisees-au-plasma/produits/ti-6al-4v-poudre-dalliage-de-titane/#15-45_m`.

[187] *Standard specification for aluminum and aluminum-alloy sheet and plate*, `https://www.astm.org/Standards/B209.htm`, Accessed: 2021-03-15.

[188] *ASM Specialty Handbook: Aluminum and Aluminum Alloys*. Materials Park, Ohio: ASM International, 1993, ISBN: 978-0-87170-496-2.

[189] S. M. Shepard and M. F. Beemer, "Advances in thermographic signal reconstruction," in *Thermosense: thermal infrared applications XXXVII*, International Society for Optics and Photonics, vol. 9485, 2015, 94850R.

[190] J. Cizek, O. Kovarik, J. Cupera, J. Kondas, T. Bajer, F. Siska, M. Janovska, and H. Seiner, "Measurement of mechanical and fatigue properties using unified, simple-geometry specimens: Cold spray additively manufactured pure metals," *Surface and Coatings Technology*, vol. 412, p. 126 929, 2021, ISSN: 0257-8972. DOI: `https://doi.org/10.1016/j.surfcoat.2021.126929`. [Online]. Available: `https://www.sciencedirect.com/science/article/pii/S025789722100102X`.

[191] D. Vlcek, *Damage tolerance evaluation of L410 NG aircraft lower wing integrally stiffened panel*, Section: Detectability and inspection program, 2013.

[192] M. Hirz and P. Rossbacher, "Enhanced knowledge-based 3D-CAD methods supporting automotive body-in-white production engineering," in *MOTSP 2016 International Conference Management of Technology – Step to Sustainable Production*, 2016.

[193] KM Yachtbuilders. (2021). Aluminium, [Online]. Available: `https://www.kmy.nl/the-shipyard/aluminium/`.

[194] APCO Technologies. (2021). Sandwich panels qualification brochure, [Online]. Available: `https://www.apco-technologies.eu/catalogue-datasheets/`.

Abbreviations

Al Aluminum

AlF Aluminum Oxide Fibre

ARALL Aramid Fiber Reinforced Aluminum Laminate

ASI Adiabatic Shear Instability

BCR Bonded Crack Retarder

BCRs Bonded Crack Retarders

BF Boron Fibre

C-scan A two dimensional graphical presentation, in which the discontinuity echoes are displayed in a top view on the test surface

CA Constant Amplitude

CARE Carbon Fibre Reinforced Aluminum

CF Carbon Fibre

CNC Computer Numerical Control

cp commercialy pure

CSCR Cold Sprayed Crack Retarder

CSCRs Cold Sprayed Crack Retarders

CT Compact Tension

CTE Coefficient of Thermal Expansion

DLD Direct Laser Deposition

EBSP Electron Beam Suface Processing

ESET Eccentrically-Loaded Single Edge Crack Tension

FE Finite Element

FEA Finite Element Analysis

FPL Forest Products Laboratory

GF Glass Fibre

GLARE Glass Reinforced Aluminum Laminate

GM Geometry Modification

HE Hydrogen Embrittlement

LEAF Linear Elastic Analysis of Fracture

LEF Life Extension Factor

LICRA Life Increment Crack Retarders Analysis

M(T) Middle Tension

makima Modified Akima piecewise cubic Hermite interpolation Matlab Function

MMC Metal Matrix Composite

NASGRO suite of computer programs used to analyze fracture and fatigue crack growth

ReSLIC Reinforced Structures Life Improvement Calculation

RS Residual Stresses

RT Room Temperature

SCC Stress Corrosion Cracking

SENT Single-Edge Notched Tension

SIF Stress Intensity Factor

SLM Selective Laser Melting

Ti Titanium

TLP Transient Liquid Phase

UAM Ultrasonic Additive Manufacturing

UCCR Ultrasonically Consolidated Crack Retarder

UD Unidirectional

VA Variable Amplitude

VCCT Virtual Crack Closure Technique

VHPCR Vacuum Hot Pressed Crack Retarder

Appendix A

Delamination data

A.1 1-CFUD-BCR

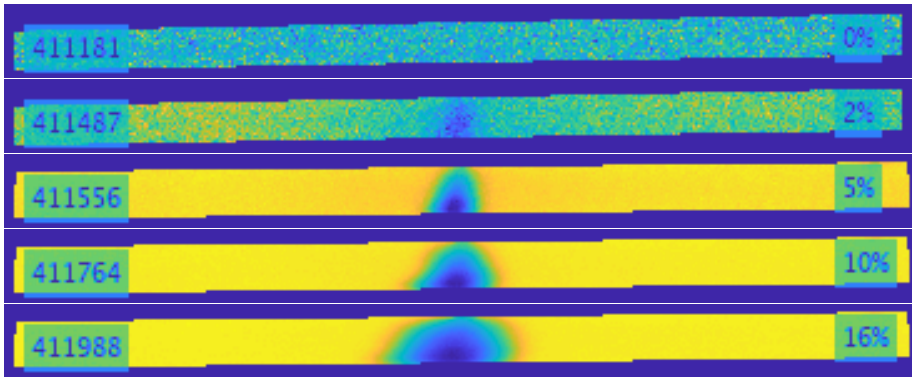

(a) Left BCR

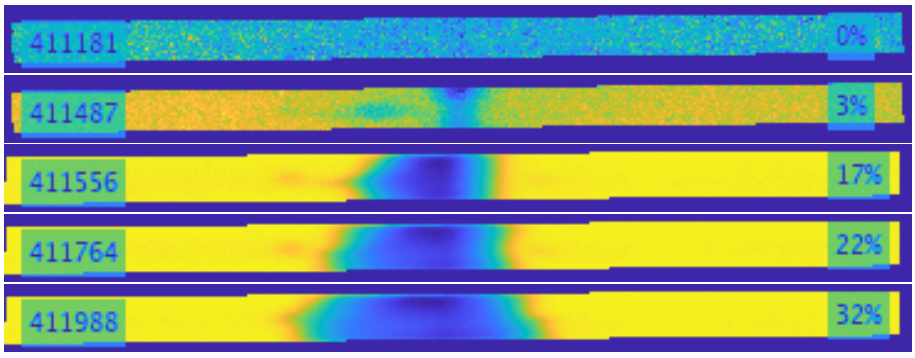

(b) Right BCR

Figure A.1: 1-CFUD-BCR specimen: Delamination patterns.

A.2 2-CFUD-BCR

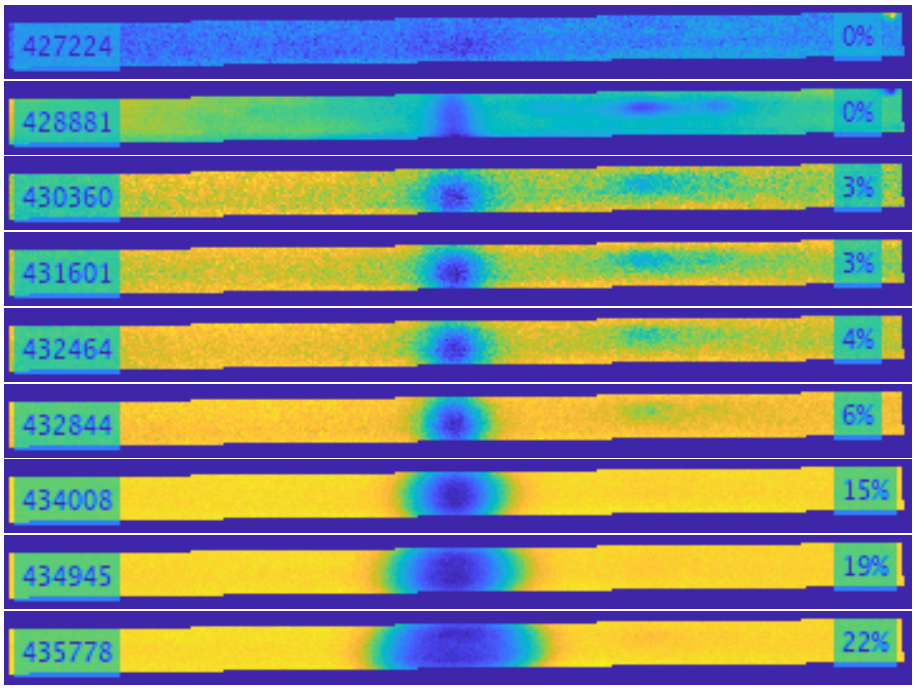

(a) Left BCR

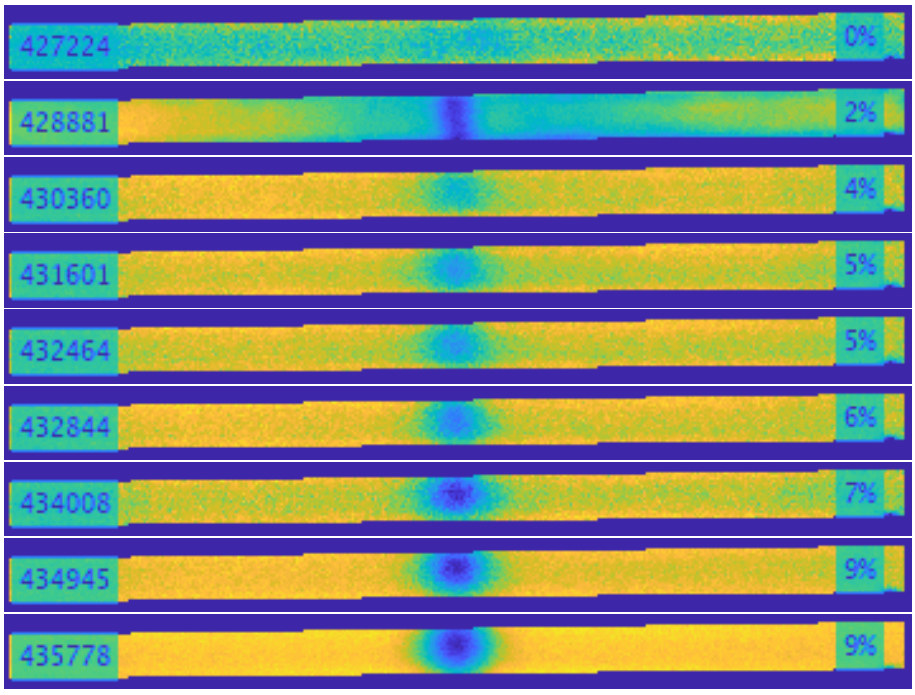

(b) Right BCR

Figure A.2: 2-CFUD-BCR specimen: Delamination patterns.

A.3 1-AISI301A-BCR

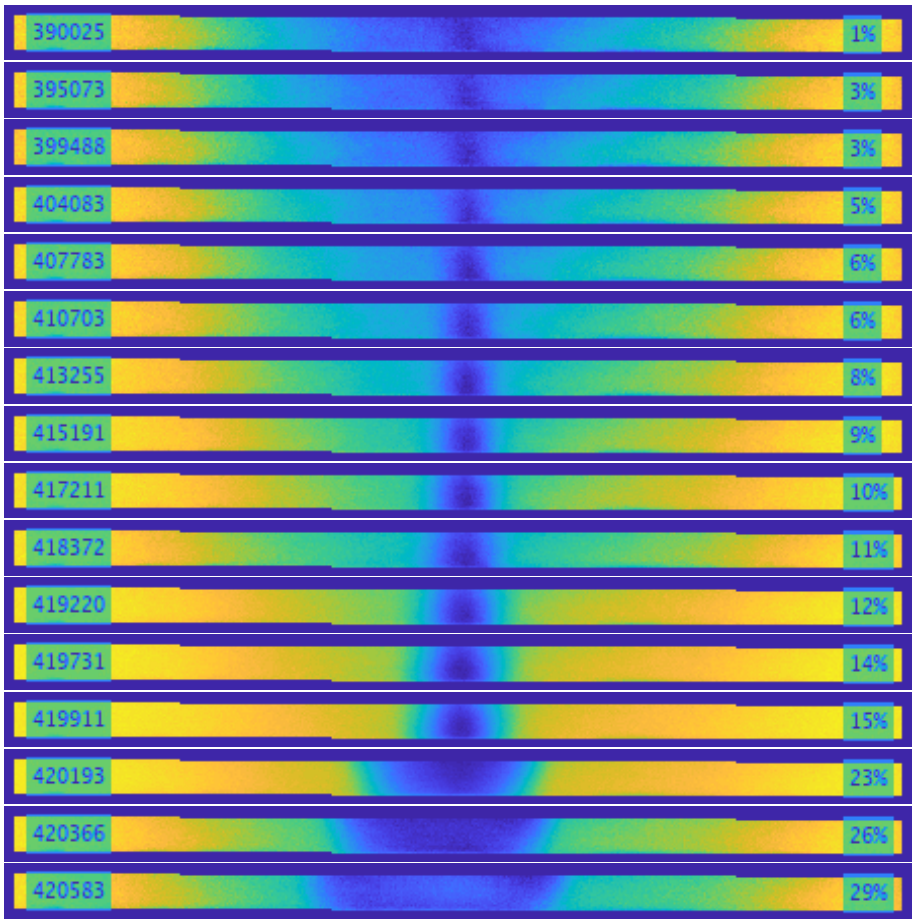

(a) Left BCR

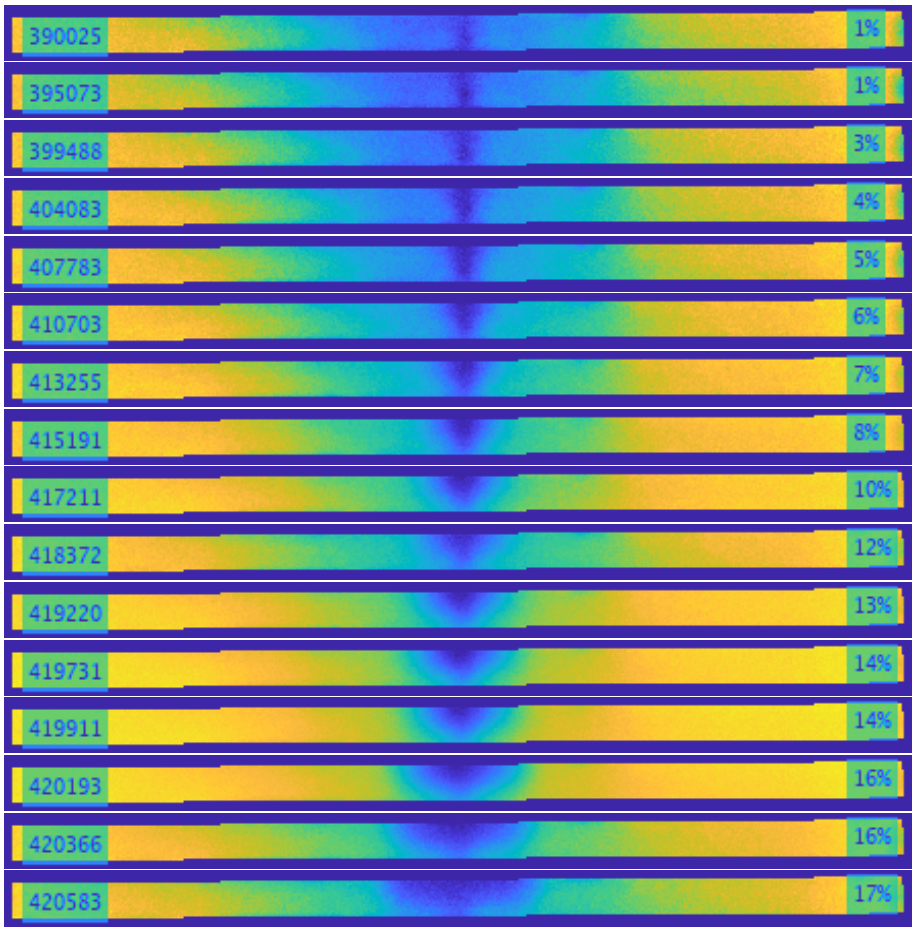

(b) Right BCR

Figure A.3: 1-AISI301A-BCR specimen: Delamination patterns.

A.4 2-AISI301B-BCR

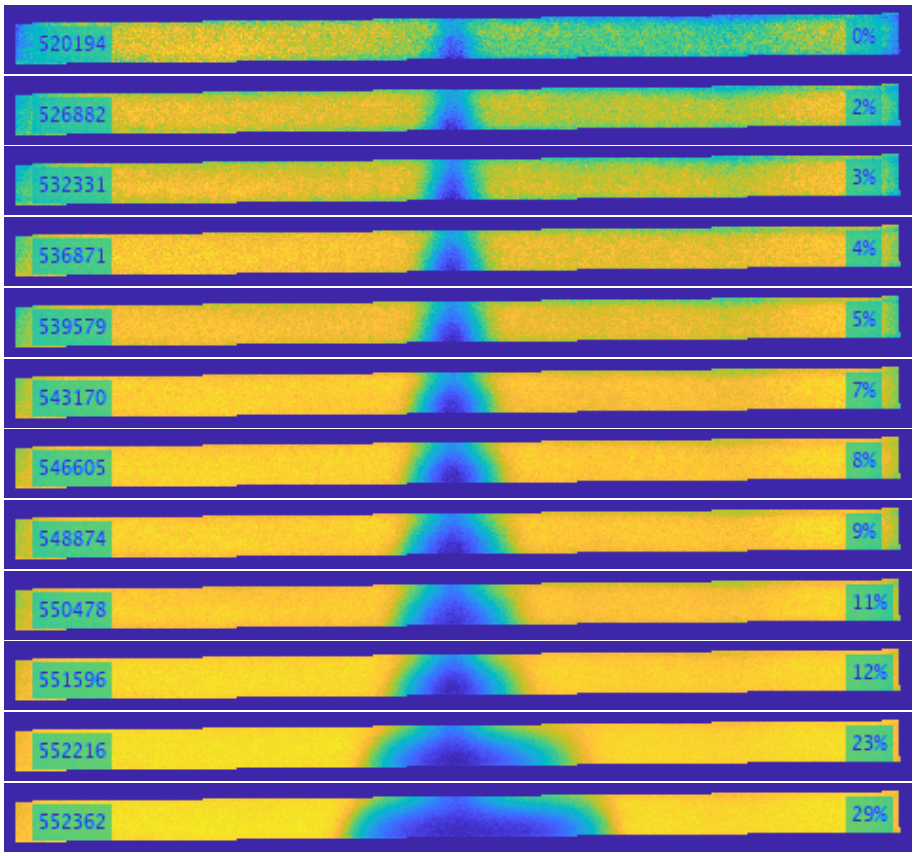

(a) Left BCR

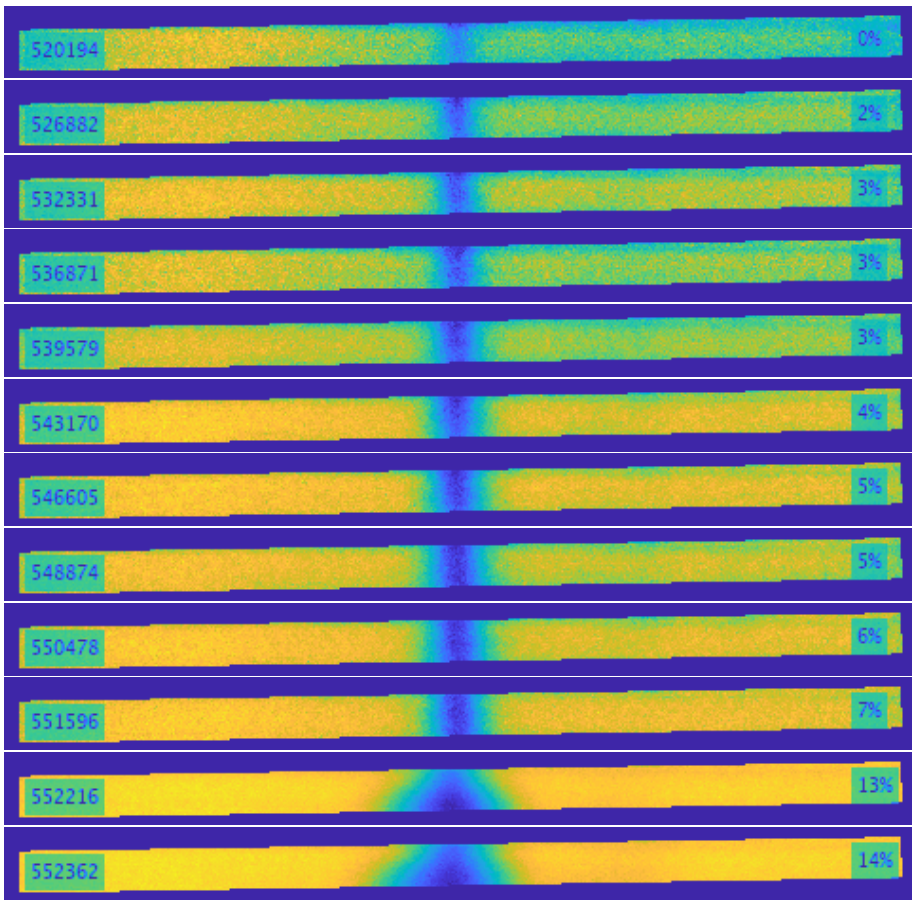

(b) Right BCR

Figure A.4: 2-AISI301A-BCR specimen: Delamination patterns.

A.5 2-AISI301-UCCR

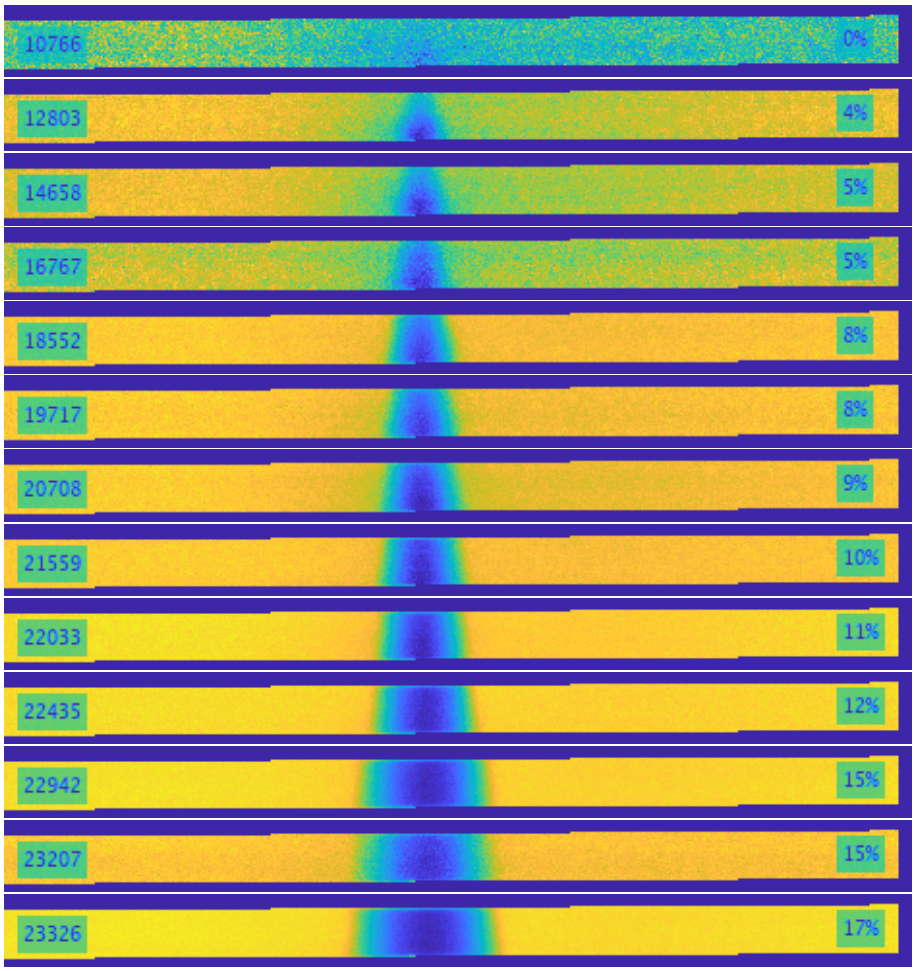

(a) Left BCR

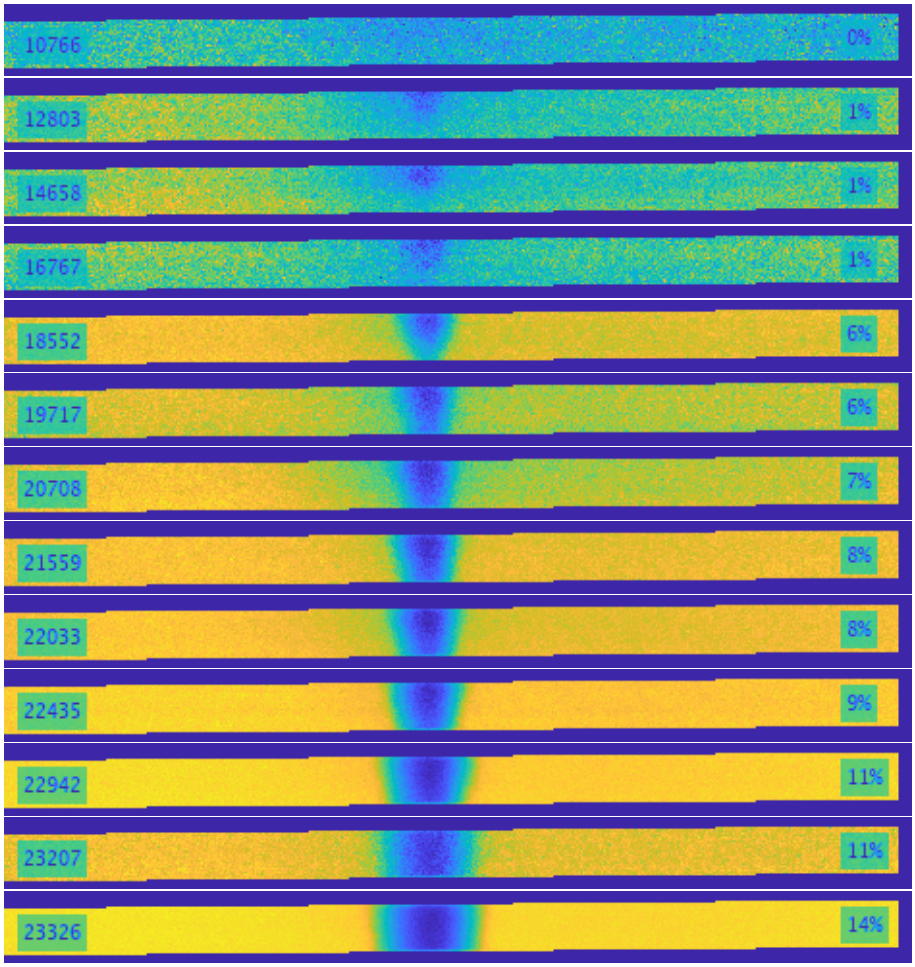

(b) Right BCR

Figure A.5: 2-AISI301-UCCR specimen: Delamination patterns.